Optical Manipulation of Micro- and Nano-particles Using Evanescent Fields

Marios Sergides

A thesis submitted to the University College London

in partial fulfilment of the requirements for the

degree of Doctor of Philosophy.

Department of Physics and Astronomy

University College London

England

October 2013

Declaration

I, Marios Sergides confirm that the work presented in this thesis is my own. Where information has been derived from other sources, I confirm that this has been indicated in the thesis.

Signed ..... Date .....

Abstract

Optical manipulation of micro- and nano- scale particles using evanescent fields has been of high importance not only in terms of fundamental optical physics, but also in terms of a variety of optical trapping applications involving the sorting and trafficking of such particles. We present a study of the manipulation of micro-particles and the formation of optically bound structures of particles in evanescent wave traps. Two trapping geometries are considered: the first is a surface trap where the evanescent field above a glass prism is formed by the interference of a number of laser beams incident on the prism-water interface; the second uses the evanescent field surrounding a bi-conical tapered optical fibre that has been stretched to produce a waist of sub-micron diameter.

In the surface trap using the Kretschmann geometry we have observed the formation of optically bound one- and two-dimensional structures of particles. The binding spring constant and measured by tracking particle motion and the extent of the particles Brownian fluctuations. Additionally, we have measured the inter-particle separations in the one-dimensional chain structures and characterised the geometry of the two-dimensional arrays.

In the tapered optical fibre trap we demonstrated both particle transport for long distances along the fibre, and the formation of stable arrays of particles. Firstly, we present experimental results on the fabrication of tapered optical fibres using the 'heat-and-pull' technique, and evanescent wave optical binding of micro-particles to the taper. We have calculated the distribution of the evanescent field surrounding a tapered fibre for a number of modes as the fibre diameter approaches the cut-off. We show that an appropriate combination of modes can give additional control over the spatial distribution of evanescent

field maxima around the fibre, and hence the locations of the optical trapping (binding) sites, and suggest applications for controlled micro-particle trafficking and delivery. The formation of stable optically bound chain structures has been observed, and the propulsion velocities of single particles pushed along the fibre been measured by a particle tracking method. Next, we show how the plasmon resonance of metallic nano-particles can be exploited to enhance the optical trapping force, and suggest how a two-colour or bi-chromatic nano-fibre trap for plasmonic particles may be implemented.

In both experiments we implement video microscopy to track the particle locations and make quantitative measures of the particle dynamics. The experimental studies of particle structures are complemented by light scattering calculations based on Mie theory to infer how the geometries of the observed particle structures are controlled by the underlying incident and scattered optical fields.

Publications

1. M. Sergides, S. E. Skelton, E. Karczewska, K. Thorneycroft, O. M. Maragò, P. H. Jones. *"Optically bound particle structures in evanescent wave traps"*, Proc. SPIE 8458, Optical Trapping and Optical Micromanipulation IX, 84583C (2012).

2. S. E. Skelton, M. Sergides, R. Patel, E. Karczewska, O. M. Maragò, P. H. Jones. *"Evanescent wave optical trapping and transport of micro- and nanoparticles on tapered optical fibers"*, Journal of Quantitative Spectroscopy and Radiative Transfer 113 2512-2520 (2012).

Acknowledgements

I will begin by thanking my PhD supervisor, Dr Philip Jones, for his guidance, encouragement and support throughout the past four years. He has not only been a brilliant teacher, but also an inspiring collaborator. Moreover I am grateful for his help, patience and time spent on preparing this thesis.

In addition, I've learned a lot through collaborations and discussions with members of other institutes. First, I would like to thank Onofrio Maragò (CNR-IPCF, Messina, Italy) for sharing his enthusiasm and knowledge and also for making me feel comfortable during my visit there. I would also like to thank, all members of the Quantum Optics Group at University College Cork, Republic of Ireland, (now at Okinawa Institute of Science and Technology, Japan) and especially Dr Síle Nic Chormaic, Dr Jonathan Ward, and Mary Frawley for their useful input on the designing of the fibre 'heat-and-pull' rig.

Moreover, I am grateful to the other members of the UCL Optical Tweezers Group, for their help and friendship over the years, particularly Susan Skelton for providing me with assistance whenever required and spending many hours working in the lab and travelling to conferences with me. Special thanks go to Radhika Patel and Ewa Karczewska, for their contributions to the tapered optical fibre project.

On a more personal note, I would like to thank my colleagues in the UCL Atomic, Molecular, Optical and Positron Physics group, Alexandros Gerakis who has been my friend since my master studies, Dr Connor Maher-McWilliams, Pete Edmunds, Dr Arne Wickenbrock, Ilhan Candan, Constantinos Lazarou, Chris Perry and the lovely Naïri Usher for the useful discussions and entertainment they offered me during my stay at UCL.

My research has been funded by the Engineering and Physical Sciences Research Council (UK). Thanks to Nanoscience Europe for funding the tapered optical fibre project, the Royal Society for funding my visit to Messina, Sicily, and the Okinawa Institute of Science and Technology for supporting my trip to Okinawa, Japan.

A great amount of love, support and patience throughout the years has come from my family, particularly my parents, and I would like to thank them all for believing in me always. I would never have made it to this point without them. I also owe a massive debt of gratitude to my close friends from Cyprus who have been supportive all these years, and especially Andreas Papaefstathiou and Giannis Constantinou for proofreading the thesis and helping me in times of need with physics matters since they both are excellent physicists. Any remaining errors are of course my sole responsibility.

Contents

1 Introduction **1**

1.1 Motivation 1

1.2 History of Optical Trapping and Binding 2

1.2.1 Optical Tweezers 3

1.2.2 Optical Binding 5

1.2.2.1 Lateral Optical Binding 5

1.2.2.2 Longitudinal Optical Binding 6

1.2.2.3 Surface (Evanescent Field) Optical Binding . . 8

1.3 Thesis outline 11

2 Generalised Lorentz-Mie Theory (GLMT) **14**

2.1 Introduction 14

2.2 Scattering Theory 15

2.2.1 Maxwell's Equations 16

2.2.2 Solution of the Electromagnetic Equation 16

2.2.3 Scattering Problem Solution 19

2.3 Single Particle Scattering Simulations 24

2.3.1 Plane Wave 25

2.3.2 Counter Propagating Plane Waves 27

2.3.2.1 Parallel Polarisations 27

2.3.2.2 Perpendicular Polarisations 29

2.3.3 Gaussian Beam Profile 29

2.3.4 Evanescent Waves 31

2.4 Force on a Scatterer 33

2.4.1 Force on a Dielectric Sphere 33
2.4.2 Force on a Dielectric Sphere in Counter Propagating Beams 35
2.5 Outlook 36

3 Evanescent Field Surface Trap: Method 39
3.1 Introduction 39
3.2 Experimental Set-up 40
3.2.1 One-dimensional Surface Trap 40
3.2.2 Two-dimensional Surface Trap 45
3.3 Particle Tracking 48
3.4 Outlook 50

4 Evanescent field surface trap: Results 52
4.1 Introduction 52
4.2 Optical Binding Beam Configuration 53
4.3 1D Binding 54
4.3.1 Particle Separation 55
4.3.1.1 Parallel Polarisations 56
4.3.1.2 Orthogonal Polarisations 62
4.3.2 Spring Constant 65
4.3.2.1 Parallel Polarisations 68
4.3.2.2 Orthogonal Polarisations 68
4.4 2D binding 71
4.4.1 Lattice Geometry 71
4.4.1.1 Square Lattice 73
4.4.1.2 Hexagonal Lattice 79
4.4.2 Spring Constant 82
4.5 Optical Binding of Carbon Nano-tubes (CNT) 84
4.6 Outlook 88

5 Fields and Forces Around a Nano-Fibre 90

5.1 Introduction . . . 90

5.2 Evanescent Field Distribution Around the Tapered Region of a Nano-Fibre . . . 91

5.3 Mode Calculations Guided in Tapered Fibres . . . 97

5.3.1 Linearly Polarised Light . . . 98

5.3.2 Circularly Polarised Light . . . 100

5.4 Optical Forces Around Tapered Optical Fibres . . . 101

5.4.1 Interaction with Metallic Nano-particles . . . 106

5.5 Optical Manipulation of Metallic Nano-particles on Tapered Optical Fibres . . . 110

5.5.1 Silver Nano-particles . . . 110

5.5.1.1 Lin $\parallel$ Lin Configuration . . . 111

5.5.1.2 Lin $\perp$ Lin Configuration . . . 113

5.5.1.3 $\sigma - \sigma$ Configuration . . . 114

5.5.2 Gold Nano-particles . . . 115

5.5.2.1 Linear Polarisation . . . 117

5.5.2.2 Circular Polarisation . . . 118

5.5.3 Particle Sorting . . . 119

5.6 Outlook . . . 121

6 Tapered Optical Fibre Trap: Method 122

6.1 Introduction . . . 122

6.2 Fibre-pulling rig . . . 123

6.3 Tapered Optical Fibre Trap . . . 126

6.4 Fused Tapered Fibre Couplers . . . 127

6.5 Outlook . . . 129

7 Tapered Optical Fibre Trap: Results 130

7.1 Introduction . . . 130

7.2 Optical Manipulation of Micro-Particles . . . 131

7.2.1 Circular Polarisation 132
7.2.2 Two Beam Tapered-Fibre Trap 134
7.3 Outlook 137

8 Conclusion **138**
8.1 Discussion 138
8.2 Future Directions 140

List of Figures

1.1 Dielectric particle trapped in the x-y direction by the light of a single-beam gradient force trap. 3

1.2 Dielectric particle axially trapped by the light of a single-beam gradient force trap. 3

1.3 Experimental setup of lateral optical binding experiment from Burns *et al.*, 1989 6

1.4 Longitudinal optical binding by two counter-propagating beams 7

1.5 Kretschmann configuration 9

1.6 Array of 460 nm diameter spheres with s-polarised light 10

1.7 Force acting on a single particle placed halfway between a bright and dark fringe 10

2.1 Transformation of Cartesian system to spherical coordinates. . . 21

2.2 Mie scattering simulation: 1 μm diameter sphere with $n_{sph} = 1.45$ immersed in water, $n_{water} = 1.33$ and illuminated by a plane wave, $\lambda = 1064$ nm. 25

2.3 Intensity maximum in the forward scatter direction for a single beam case. 26

2.4 Intensity profile in the z-direction 27

2.5 Mie scattering simulation: 1 μm diameter sphere with $n_{sph} = 1.45$ immersed in water, $n_{water} = 1.33$ and illuminated by two counter propagating plane waves, $\lambda = 1064$ nm, with parallel polarisations. 28

2.6 Modulation of the linear fringe patter due to forward scattering in the ±z-directions. 28
2.7 Mie scattering simulation: 1 μm diameter sphere with n_{sph} = 1.45 immersed in water, n_{water} = 1.33 and illuminated by two counter propagating plane waves, λ = 1064 nm, with orthogonal polarisations. 29
2.8 The amplitudes of the real and imaginary parts of g_ℓ for a Gaussian beam. 30
2.9 Mie scattering simulation: 1 μm diameter sphere with n_{sph} = 1.45 immersed in water, n_{water} = 1.33 and illuminated by a Gaussian beam, λ = 1064 nm. 31
2.10 Refraction of a plane wave at a dielectric interface. 32
2.11 Force on a dielectric sphere. 35
2.12 Force on a dielectric sphere in counter-propagating beams. . . . 36
2.13 Intensity profile in the z-direction for all configurations. 37

3.1 Evanescent wave surface trap: 3D illustration of the experimental set-up 40
3.2 Evanescent wave surface trap: Experimental set-up. 41
3.3 Elevation angle determination for 1D binding set-Up. 42
3.4 Scattered evanescent waves by a group of micro-particles at prism - water interface. 43
3.5 Beam profile of the weakly focused beam at the prim-water interface 44
3.6 Gaussian beam analysis for the Dove prism 45
3.7 Evanescent Wave Surface Trap: Experimental set-up in two-dimensions. 46
3.8 Elevation angle determination For 2D binding set-up. 47
3.9 Gaussian beam analysis for the approximately hemispherical lens 47
3.10 Particle Tracking 49
3.11 Flowchart of the particle tracking process. 49

3.12 Particle trajectory reconstructed for 1 μm silica particles in one-dimensional bound chain. Particles were tracked over 1770 frames at 100 frames per second. 50

4.1 Interference pattern for one and two pairs for counter-propagating beams. 54
4.2 One-dimensional chain of optically bound dielectric spheres. . . 55
4.3 Position of spheres in one-dimensional bound chain. 56
4.4 Force on silica sphere place between a bright and dark fringe as a function of $k\alpha$. 57
4.5 GLMT Calculation: Intensity measured along the propagation direction for silica spheres for all sizes used in experiment in counter propagating beams with parallel polarisations. 58
4.6 One-dimensional bound chain of 0.8 μm silica spheres. 59
4.7 Inter-particle separation of 0.8 μm silica spheres in counter-propagating beams with parallel polarisations as a function of laser power. 59
4.8 One-dimensional bound chain of 1.0 μm silica spheres. 60
4.9 Inter-particle separation of 1.0 μm silica spheres in counter-propagating beams with parallel polarisations as a function of laser power. 61
4.10 One-dimensional bound chain of 1.5 μm silica spheres. 61
4.11 Inter-particle separation of 1.5 μm silica spheres in counter-propagating beams with parallel polarisations as a function of power. 62
4.12 Inter-particle separation for 0.8 μm, 1.0 μm, 1.5 μm silica spheres in counter-propagating beams with orthogonal polarisations as a function of power. 63
4.13 0.8 μm bound particle trajectories in a chain structure at low and high laser powers. 64

4.14 GMLT Calculation: Intensity in the propagation direction for silica spheres with sizes used in experiment in counter propagating beams with orthogonal polarisations. 65
4.15 Histograms of bound particles in one-dimensional chain. 65
4.16 Oscillating optically bound chain of 1.0 μm for laser power P = 0.954 W. The oscillation in the direction orthogonal to propagation (y-) is apparent. 66
4.17 Selection of data for which the 1D bound structure is more stable. 66
4.18 Position fluctuations of a dielectric particle in the direction parallel to the optically bound chain. 68
4.19 Spring constant vs Laser Power for 0.8 μm, 1.0 μm and 1.5 μm silica particles in one-dimensional bound chains formed in parallel polarised laser beams. 69
4.20 Spring constant vs Laser Power for 0.8 μm, 1.0 μm and 1.5 μm silica particles in one-dimensional bound chains formed in orthogonally polarised laser beams. 69
4.21 Difference between the force magnitudes for the parallel and orthogonal polarisation cases as a function of laser power. 70
4.22 Square and Hexagonal Lattice Representation. 72
4.23 Square lattice formed by 1 μm silica spheres at the crossing point of two orthogonal counter-propagating beam pairs. 73
4.24 Particle trace and particle distance distribution in square lattice. 74
4.25 Positions of 1 μm silica spheres and the interference landscape created by two orthogonal pair of beams with parallel polarisations. 75
4.26 Positions of 20 dielectric cylinders and field distributions from Grzegorczyk *et al*, 2006. 77
4.27 Voronoi diagram for the square lattice of 1.0 μm silica particles. 78
4.28 Bond orientational order parameter as a function of time for a square lattice. 79

4.29 Hexagonal lattice formed by 1 μm silica spheres at the crossing point of two orthogonal counter-propagating beam pairs of orthogonal polarisations. 79
4.30 Particle trace and particle distance distribution in hexagonal lattice. 80
4.31 Particle positions of 1 μm silica particles and optical landscape created by two cross polarised orthogonal beam pairs. (b) Image of actual particles considered in part (a). 80
4.32 Voronoi diagram for the hexagonal lattice of 1.0 μm silica particles. 81
4.33 Bond orientational order parameter as a function of time for a hexagonal lattice. 82
4.34 Hexagonal lattice formed by 0.8 μm silica spheres at the crossing point of two orthogonal counter-propagating beam pairs of orthogonal polarisations. 83
4.35 Spring constant vs Laser Power for 0.8 μm and 1.0 μm silica particles in a hexagonal two-dimensional array. 83
4.36 Optical Binding of Carbon Nano-tubes. 86
4.37 Carbon Nano-tubes trace with video microscopy. 87
4.38 Carbon Nano-tubes position fluctuations histogram in one-dimensional bound structure for laser power, P = 0.954W and number of counts, N = 51. 87

5.1 Fibre cross-section and Propagation of light ray in an optical fibre 92
5.2 Normalised propagation constant β/k_0 vs Fibre diameter. 98
5.3 Directed fields for the linearly polarised (x-) fundamental HE_{11} mode in silica nano-fibre. 99
5.4 $|E_x|^2$ in the fundamental mode HE_{11} with quasi-linear polarisation for various fibre radii. 100
5.5 Directed fields for the circularly polarised fundamental HE_{11} mode in silica nano-fibre. 101

5.6 $|E_x|^2 + |E_y|^2$ and $|E_z|^2$ in the fundamental mode HE_{11} with circular polarisation for various fibre radii. 102

5.7 Components of the spin density in circularly polarised HE_{11} mode. 104

5.8 Non-zero components of the Poynting vector for the quasi-linearly (x-) and circularly polarised fundamental HE_{11} mode. 105

5.9 Optical Properties of Silver Nano-particle. 108

5.10 Components of the spin curl force acting on a sliver nano-particle in circularly polarised HE_{11} mode. 109

5.11 Silver Extinction Efficiency. 111

5.12 Dipole Interaction Energies for red- and blue- detuned beams from silver plasmon resonance with parallel linear polarisations. 112

5.13 Dipole interaction energy for different wavelengths around silver resonance. 113

5.14 Dipole Interaction Energies for red- and blue- detuned beams from silver plasmon resonance with orthogonal linear polarisations. 114

5.15 Dipole Interaction Energies for red- and blue- detuned beams from silver plasmon resonance with circular polarisations. 115

5.16 Optical Properties of Gold Nano-particle. 116

5.17 Dipole Interaction Energies for red- and blue- detuned beams from gold plasmon resonance with linear polarisations. 117

5.18 (a) Dipole interaction energy for different wavelengths around gold resonance; (b) Evanescent field penetration depth Λ vs wavelength. 118

5.19 Dipole Interaction Energies for red- and blue- detuned beams from gold plasmon resonance with circular polarisations. 119

5.20 Calculations on particle sorting - Interaction energies. 120

5.21 Calculations on particle sorting - Propelling velocities. 120

6.1 Custom made Fibre-pulling rig. 124

6.2 Transmission monitoring during tapered fibre fabrication. 125

6.3 Mounted tapered fibre on custom-made slide. 126
6.4 Tapered optical fibre trap apparatus 127
6.5 Fused twisted tapered fibres. 128
6.6 Fused tapered fibre coupler intensity variation with polarising angle. 128

7.1 Directed fields for the linearly polarised (x-) fundamental HE_{11} mode in silica nano-fibre. 131
7.2 Propulsion of 2 μm polystyrene spheres along a tapered fibre. . 132
7.3 Reconstructed trajectory of micro-particles along a tapered fibre. 132
7.4 Reconstruction of particle 'shooting'. 133
7.5 Directed fields and Poynting vector magnitudes for the circularly polarised fundamental HE_{11} mode in silica nano-fibre. . . . 134
7.6 Helical trajectory of micro-particles along and around a tapered fibre 135
7.7 Reconstruction of helical trajectory of micro-particles along and around a tapered fibre 135
7.8 Sequence of frames from a film of optical binding and micro-particle chain formation in the evanescent field of a tapered optical fibre. 136

Chapter 1

Introduction

1.1 Motivation

This thesis investigates phenomena occurring when a number of colloidal particles are confined in an evanescent wave trap, resulting in light-induced coupling between the trapped particles (optical binding) and the formation of optically bound structures. These light-mediated interactions are of high importance not only in terms of fundamental optical physics, but also in terms of a variety of optical trapping applications involving the sorting and trafficking of microparticles. The confinement of multiple particles in the same trap intending to create micro-structures can be achieved by using either:

- single or multiple strongly focused laser beams (optical tweezers) where the interactions between particles are an undesirable effect [1, 2]; or
- intense laser fields (which need not to be strongly focused) where the interactions between the particles may result in periodic patterns [3, 4].

The aim of this thesis is to provide a better understanding of the physics involved in evanescent wave optical binding through the experimental analysis of systems where the interactions between the trapped particles are of higher significance compared to the optical forces created by the incident trapping fields. We believe that the work of this thesis can potentially lead to new applications such as sorting and trafficking of dielectric and metallic micro- and nano-particles.

1.2 History of Optical Trapping and Binding

In 1986, Arthur Ashkin demonstrated the first 'optical tweezers' where a single laser beam can be used to trap colloidal particles at the beam waist. The tightly focused laser beam creates a force which depends on the refractive index mismatch between the particle and the surrounding medium, and due to this force dielectric particles are held stably at the beam waist, or can be moved around in three dimensions [1]. Later on, Burns and co-workers were able to use intense multiple beams to create an interference pattern at their crossing point on a surface, and trap multiple colloidal particles, forming arrays [4, 5]. These arrays were formed due to the multiple scattering of the laser light and this phenomenon was given the name of 'optical binding'.

The idea of driving micro-particles using evanescent waves was first proposed by Kawata and Sugiura in 1992 [6]. In 2005, Garcés-Chávez *et al.*, using two counter propagating beams demonstrated that the net radiation pressure can be cancelled and micro-particles with diameters smaller than the fringe spacing were trapped in the maxima of the interference pattern [7]. Optical manipulation of colloidal particles experiments using evanescent waves will be described in Chapter 3.

In 2004, the use of tapered optical fibres or nano-fibres was suggested for trapping and manipulating cold atoms by using the strong evanescent field that surrounds the surface of the tapered region. This was successfully demonstrated by Sagué *et al.* in 2007 [8]. In addition Brambilla *et al.* presented

results showing manipulation of micro-spheres around tapered fibres [9]. Nano-fibres are produced by pulling an optical fibre while it is heated and can have submicron diameters [10]. When light is guided through these sub-micron optical fibres a strong evanescent field surrounds the surface of the tapered region. This will be discussed in more detail in Chapter 4.

1.2.1 Optical Tweezers

Optical tweezers were demonstrated in 1986 [1] and since then they are considered as a useful tool for manipulating micro-particles and sub-micron structures. This single-beam gradient force radiation-pressure particle trap uses a high numerical aperture microscope objective lens which focuses a laser beam leading to the creation of a trapping force which is of the order of pico-newtons. When the diameter of the particle is larger than the wavelength of the light in use, optical tweezers can be explained using the following figures:

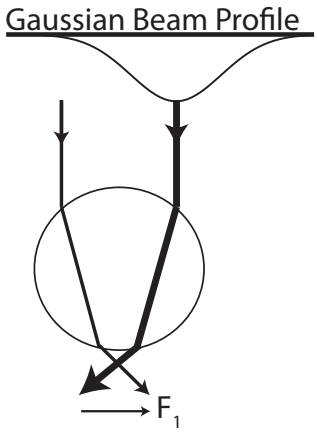

Figure 1.1: Dielectric particle trapped in the x-y direction by the light of a single-beam gradient force trap.

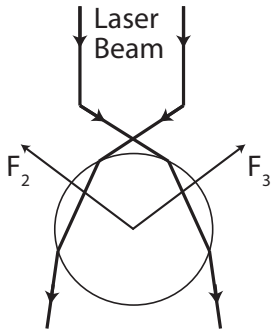

Figure 1.2: Dielectric particle axially trapped by the light of a single-beam gradient force trap.

Light rays passing through the dielectric particle get refracted resulting to a change in their direction. Since light has momentum, this change in direction indicates a change in momentum. By Newtons third law there is an equal and opposite momentum change on the particle. Since more intense rays cause larger momentum change towards the centre for a Gaussian TEM_{00} beam the net gradient force returns the particle to the centre of the beam (see Fig. 1.1).

If the beam is aligned to pass through the centre of the particle, refraction occurs symmetrically. The gradient force is in the axial direction and this cancellation causes the particle to be trapped in the axial direction of the trap (Fig. 1.2). This gradient force is given by:

$$F_{gradient} = \frac{n_p P Q_g}{c}, \tag{1.1}$$

where P is the power of light in use, n_p is the refractive index of the particle, c is the speed of light and Q_g is the fraction of optical momentum transferred to the particle [11].

Additionally, there exist a force generated by reflection or scattering from the interface of the particle. This is due to the small refractive index mismatch between the particle and the suspension fluid resulting to Fresnel reflections and corresponding recoil forces. Energy is lost from the incident beam upon reflection and then re-radiated. Therefore the momentum transfer on the particle (along the beam propagation and opposite to the direction of the emitted photon) is equal to the momentum lost from the incident beam. The force acting on the particle is in the direction of the incident light since there is no preferred direction for photon emission [12]. This force is called the scattering force and it is expressed as:

$$F_{scat} = n_p \frac{\sigma \langle S \rangle}{c} \tag{1.2}$$

where σ is the particle's cross section and $\langle S \rangle$ is the time averaged Poynting vector.

Provided that the beam is focused strongly (high NA lens) the gradient force is greater than the forces generated by reflection or scattering from the interface of the particle. Both gradient and scattering forces scale linearly with laser intensity therefore increasing the intensity is not sufficient to form a trap. The intensity gradient has to be maximised for the gradient force to exceed the scattering force. This is achieved by focusing the laser beam using

a high numerical aperture microscope objective lens. From this description it is evident that the reflection and refraction of light, or, more precisely, the scattering of light results in a force that is of significant magnitude for micron-sized particles.

In most of the optical tweezing configurations, optical binding is an unwanted side effect which increases with the number of the trapped particles (especially for large particle sizes and high refractive indices).

1.2.2 Optical Binding

When laser light shines on a group of particles, it is apparent that these particles are not only influenced by the incident light but also by the scattered light from nearby particles. This induces forces between the particles, which causes them to self-organise in ordered states.

1.2.2.1 Lateral Optical Binding

Optical binding was first reported by Burns *et al.* in 1989 where a number of particles were optically trapped at a surface perpendicular to the direction of propagation of the trapping laser field (Figure 1.3) [4, 5]. This configuration consisted of up to five laser beams creating an interference field illuminating dilute suspensions of polystyrene spheres in water. The dielectric spheres were confined in the maxima of the interference pattern and were pushed against the top surface of the sample cell due to radiation pressure. This configuration produced optically bound crystals with lattice properties determined by the optical lattice. They also illuminated the centre of the colloidal sample by a single Gaussian beam with diameter 15 - 20 times greater than the diameter of an individual sphere. This lead to an 'unexpected' observation that spheres were attracted to the crystal centre from the beam periphery creating a close-packed crystal. The conclusion drawn from this was that the colloidal spheres were not only affected by the incident field but also by the scattered light from nearby particles.

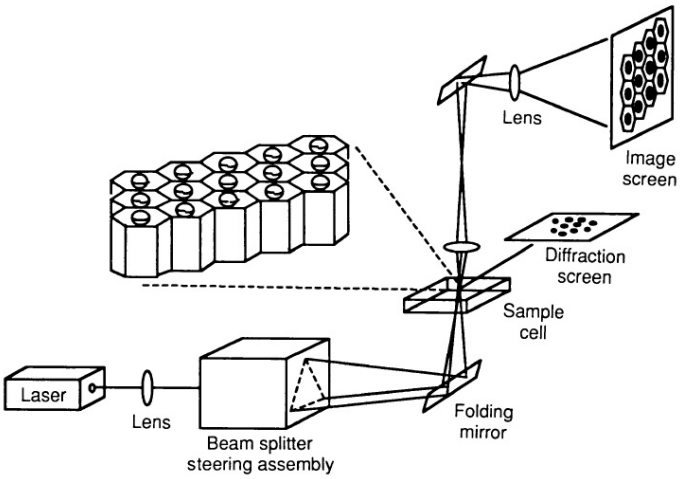

Figure 1.3: Experimental setup of lateral optical binding experiment. From Burns *et al.*, 1990 [5].

The mechanism they used to model the confinement of dielectric matter in standing waves derives from fundamental ideas of electromagnetism (Lorentz force). The simplest application of these ideas is the system of two oscillators that are allowed to interact even though the particles used in experiments were too large to be described as induced dipoles. The two oscillators are separated by a distance R and the interaction energy W (when the polarisation of the incident light is perpendicular to the direction connecting the two oscillators) is of the form:

$$W = -\frac{1}{2}\alpha^2 k^2 \frac{\cos(kR)}{R}|E|^2 \tag{1.3}$$

where α is the polarisability of the oscillator, k is wavenumber in the surrounding medium and E is the amplitude of the applied electric field [5].

In 2005 Ng *et al.* theoretically studied this trapping configuration and used Mie scattering theory to model the multiple light scattering. Their analysis predicted geometric configurations with stable or quasi-stable particles positions. A theoretical model for a three dimensional expansion of this transverse trapping geometry was also described by the same group [13].

1.2.2.2 Longitudinal Optical Binding

The first evidence of longitudinal optical binding was presented by Tatarkova *et al.* in 2002 [14]. By using two weakly focused counter-propagating Gaussian

beams they were able to trap silica micro-spheres with diameters 2.3 μm and 3 μm along the direction of propagation of the incident field. The two beams were aligned so that the radiation pressure from each one was cancelled by the other. The particles were confined in equilibrium positions with spacings several times the particle diameters. These spacings become smaller as more spheres were added to the bound structure since the particles have to fill the harmonic potential created by the two counter-propagating beams (Figure 1.4).

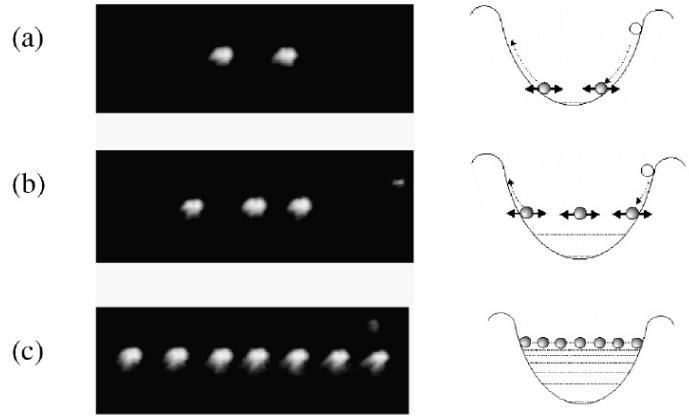

Figure 1.4: Longitudinal optical binding by two counter-propagating beams. Experimental data for the arrays of (a) two, (b) three, and (c) seven spheres (each 3 μm in size). The diagrams on the right elucidate how the particles fill up the approximately harmonic potential well created by the two counter-propagating beams. From Tatarkova *et al.*, 2002 [14].

Independently, Singer *et al.* studied this phenomenon in 2003 using the same experimental configuration. They assumed a simple model treating the polystyrene spheres used in their experiment as point scatterers even though the range of diameters they considered was in the Mie scattering regime ($0.5\lambda < D < 2\lambda$). This predicted that the bead spacings depend only on the particle diameter and not on the optical power of the incident fields or refractive index [15]. That was in agreement with their experimental data and the sphere separations reported by Tatarkova *et al.* [14].

A different approach to model longitudinal optical binding was later proposed by McGloin *et al.* in 2004 and Metzger *et al.* in 2006 [16, 17]. Based on paraxial optics they considered small dielectric spheres as micro-lenses with focal length $f = \alpha/[2(n_p - n_m)]$ in the small angle approximation and by omit-

ting high-order aberrations, where α is the radius of the sphere and n_p and n_m are the refractive indices of the sphere and the submersion medium [18]. The incident light on a sphere is focused at a distance equal to f from the sphere leading to the creation of a trap for a nearby particle which in turn creates a similar trap for the next one.

In 2008, Gordon *et al.* used a generalized multipole technique (GMT) to model the light scattering from polystyrene micro-spheres [19]. The scattered field outside the spheres was calculated by using a series of Hankel function spherical vector waves and a series of Bessel function vectorial waves for the inside of the spheres. The magnetic field was then derived from the electric field using Maxwell's equations. The forces acting on the micro-spheres could be then calculated using Maxwell's stress tensor (MST) [20]. This approach explains the self-organisation of particles and is more general for calculating the optical forces on dielectric spheres and can be applied for all sphere diameters as well as for higher refractive index contrast between the particle and the immersion medium. While MST is convenient, it is a complicated technique and time consuming in a computational point of view.

1.2.2.3 Surface (Evanescent Field) Optical Binding

Even though all previous work mentioned used free space beams, an alternative geometry is to use evanescent optical fields[1] to optically manipulate particles near a surface. The configuration used to generate evanescent fields is called the 'Kretschmann geometry' and is illustrated in Figure 1.5. The use the Kretschmann geometry allowed the development of various methods of evanescent wave trapping.

Driving of micro-particles across a surface using evanescent waves was first demonstrated by Kawata and Sugiura in 1992 [6]. Micro-particles near the surface of a high refractive index prism were driven along the surface by the radiation pressure of an evanescent wave created by a single infra-red laser beam. In this case the evanescent wave is converted to a travelling wave in the

[1]Evanescent optical fields will be discussed in more detail in Section 2.3.4

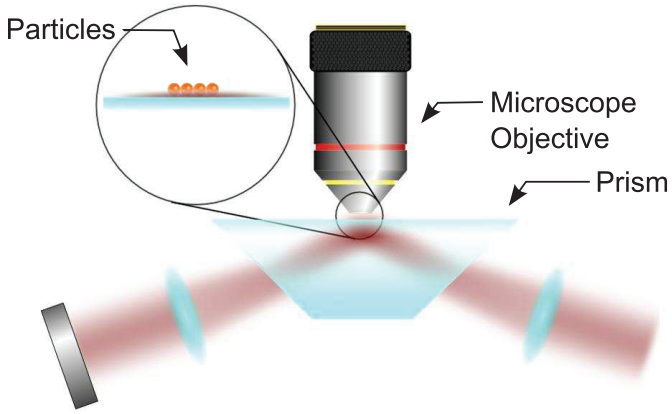

Figure 1.5: Kretschmann configuration. The beam is incident on the glass-water interface at the critical angle forming an evanescent wave which penetrates the glass substrate. Particles placed on the substrate interact with the evanescent field.

particle and a fraction of the momentum component parallel to the surface is transferred to it. In 2005, Garcés-Chávez *et al.* extended this setup to use two counter-propagating beams at an incident angle for Total Internal Reflection (TIR), causing the radiation pressure acting on the particles to be balanced in both directions [7]. The 5 μm spheres (five times greater than the optical wavelength) were localised in a lateral manner, confined to linear potential wells defined by the light interference fridges.

Mellor *et al.* in 2006, observed the formation of 2D arrays (Figure 1.6) as more particles were added to the overlap region of two wider laser beams which contradicted the results presented by Garcés-Chávez *et al.*[21, 22]. Further investigation showed that particles with sizes equal or larger than 700 nm align themselves along the fringes but for smaller particle sizes (500 nm and less) the arrays evolve to a chessboard pattern.

The conclusion drawn from these experiments was that optical binding i.e. multiple scattering effects dominate over optical trapping and the geometry of the arrays formed depends on both particle size and light polarisation. This was theoretically verified by Taylor *et al.* by using a Generalized Lorentz-Mie Theory (GLMT) [23]. They calculated the force as a function of the particle size parameter ka, where k is the wavenumber ($k = \frac{2\pi}{\lambda/n_{water}}$) and a the particle

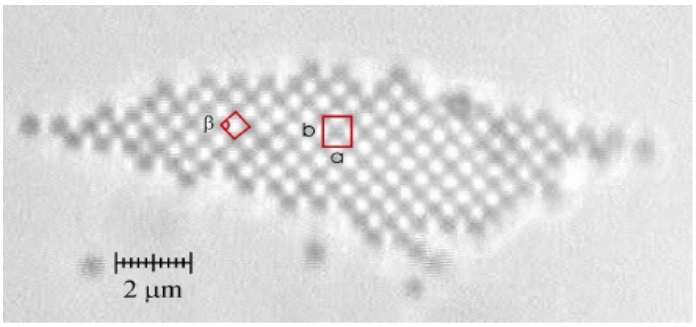

Figure 1.6: Array of 460 nm diameter spheres with s-polarised light. A centred rectangular unit cell is shown, with lattice parameters α and β perpendicular and parallel to the fringes respectively. From Mellor *et al.*, 2006 [22].

radius, for s- and p-polarised light states (Figure 1.7). The sign of the force denotes whether the particle is attracted to a bright or a dark fringe.

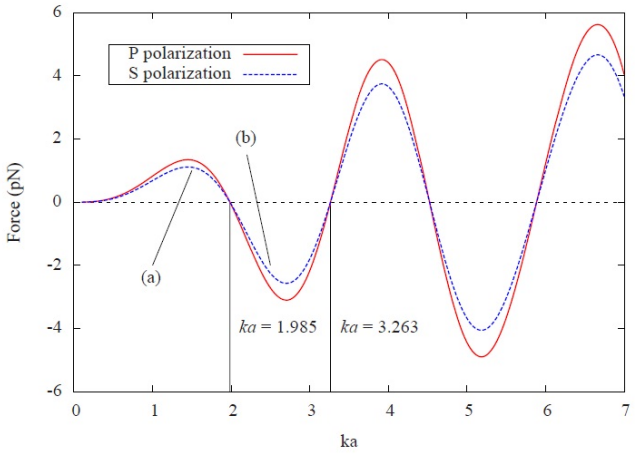

Figure 1.7: Force acting on a single particle placed halfway between a bright and dark fringe, as a function of size parameter ka. A positive force indicates that the particle is attracted to the bright fridge. Two lines are shown for different polarization states. From Taylor *et al.*, 2008 [23].

Enhancement of evanescent fields can be achieved by exploiting the motion of free electrons in metals. By making use of the surface plasmon polaritons (SPP) Garcés-Chávez *et al.*, in 2006, were able to observe the formation of hexagonal close-packed crystals at the centre of the excitation region. Linear chains were also observed when minimizing thermal effects (through the use of thin chambers of 10 μm) for powers three times less than those for a standard evanescent field with the same beam parameters [24].

Evanescent field effects can be observed in other optical structures e.g.

in standard optical fibres even though they are not normally significant. In cases where the size of the structure is comparable to the optical wavelength such as an optical 'nanofibre' then the evanescent waves generated play a dominant role and an enhanced optical interaction with nearby structures can be observed [25]. The energy inside the core of a nano-fibre can be significantly less than the energy guided outside the core if the diameter is small compared to the wavelength of light transmitted through it [26, 27]. The manipulation of matter with the aid of tapered fibres has been analysed and experimentally demonstrated by various groups [28, 8, 9]. Experimental work and results using the evanescent field near a tapered fibre for particle manipulation will be presented in Chapter 7.

1.3 Thesis outline

The aim of this thesis is to provide a scientific insight into the physical phenomena occurring during evanescent field optical binding. Such phenomena cannot be simply understood by applying the concepts used to study isolated trapped particles. The common theme of this thesis is the interactions between multiple trapped particles in evanescent waves and their behaviour in configurations where the optical trapping and binding forces are balanced.

Chapter 2, describes the Mie scattering theory and the light scattering calculations based on this theory to infer how the geometries of the observed particle structures are controlled by the underlying incident and scattered optical fields. Simulations to support our experimental work will be presented here.

Chapter 3, provides a detailed description of the experimental set-up and any calculations made prior the experiments. These experiments made use of the evanescent field of two or more counter-propagating beams ($\lambda = 1064$ nm) at a water-prism interface leading to bound states of micro-particles of different sizes. In order to facilitate these experiments a non-expensive video microscopy method was developed and used in the presentation of this work.

This development allowed the reconstruction of particle trajectories and study individual particle's dynamics.

In turn, Chapter 4, discusses the results obtained from the experimental work done on optical trapping and binding. Namely one- and two-dimensional bound arrays have been observed. The most significant novel content here is the observation of optical binding of carbon nano tubes (CNT) bundles. This is the first time that optical binding of non-spherical particles has been observed experimentally. Additionally, the characterisation of the two-dimensional bound structures is presented using methods such as Voronoi diagrams and bond orientational parameters. Finally, we present results that confirm the theoretical work done by Grzegorczyk *et al*. in 2006 on the modification of the background interference pattern by the scattered fields of the bound particles [29].

Chapter 5 presents numerical calculations of the field distribution around a tapered optical fibre. The optical trapping and scattering forces originating from the evanescent field in the tapered region are also calculated using a simple dipole model. These calculations provide an insight to the behaviour of micro- and nano- particles around a nano-fibre. Additionally, plasmonic optical forces on metallic (silver and gold) nano-particles are calculated and we show how the plasmon resonance of metallic nano-particles can be exploited to enhance the optical trapping force. A two-colour or bi-chromatic nano-fibre trap for plasmonic particles is modelled and a description of its implementation is provided. Moreover we suggest a novel method of sorting metallic nano-particles by using their plasmonic properties.

Chapter 6, considers a trapping geometry which uses the evanescent field surrounding a bi-conical tapered optical fibre that has been stretched to produce a waist of sub-micron diameter. The design and fabrication of the tapered fibres using a custom made pulling rig are described in this chapter. As in the experiments of the previous chapter we make use of video microscopy to analyse the experimental data.

Chapter 7 presents and discusses the results obtained from these experi-

ments. The motion of micro-particles in the vicinity of a the tapered region of an optical fibre is studied for the cases of the quasi-linear and circular polarised HE_{11} mode. For the second case the helical trajectory of micro-particles along and around the tapered fibre has been experimentally observed which is a novel result. This demonstrates the conversion of spin angular momentum to orbital angular momentum previously studied in high numerical aperture systems. Moreover the formation of one-dimensional bound structures has been observed for the case where the radiation pressure is balanced when coupling light from both ends of the taper.

Finally, Chapter 8 summarises the conclusions drawn from the results presented in the previous chapters and suggests topics that still need further investigation.

Chapter 2

Generalised Lorentz-Mie Theory (GLMT)

2.1 Introduction

This chapter introduces theoretical methods which give insight into the formation of optically bound structures[1]. The solution to the scattering problem of a sphere illuminated by a coherent laser field can be found in several texts [30, 31]. In this chapter we present computer simulations, using Mie scattering calculations, to represent the internal and external fields of a scatterer for different beam profiles (Section 2.3). The force on a scatterer has been also calculated for different beam configurations (Section 2.4).

The Generalised Lorentz-Mie Theory (GLMT) involves the scattering of electromagnetic waves by a single homogeneous sphere. It finds applications to the scattering processes of planetary atmospheres which contain particles of various sizes but it is also a useful tool for analysing optical manipulation

[1]Such optically bound structures in surface (evanescent) traps are presented experimentally in Chapter 4

processes. It can be applied to particles whose size is larger or smaller than the incident wavelength, ranging from the ray optics limit down to the Rayleigh limit, although it is mainly used for particles sizes which are comparable to the light wavelength (Mie Regime) where the limiting approximations of light rays or dipolar particles are not applicable.

The theory is named after Gustav Mie who was the first to develop it in the early 1900s [32]. A significant contribution to the scattering problem was also made by Debye by introducing the Debye potential used to solve Maxwell's equations [33]. A more general treatment of the subject was presented by Stratton [34]. By following his work van de Hulst simplified the presentation of the theory and in addition he derived the extinction parameter and the phase function [31]. Born and Wolf gave a more coherent approach by using the Debye potential to derive the electric and magnetic fields [35] and in turn Kerker presented a brief analysis of the theory by utilising their approach [36].

2.2 Scattering Theory

In this section we will follow van de Hulst formalism [31] to solve the scattering problem of a homogeneous sphere illuminated by an electromagnetic wave. The treatment of Maxwell's equations with the appropriate boundary conditions is required to obtain a full solution to this problem.

We will start with Maxwell's equations which are used to derive the vector wave equations for an electromagnetic field. The solutions to the vector wave equation (scalar potentials) are then found in spherical coordinates in terms of spherical Bessel functions and Legendre polynomials. The scattering coefficients for the internal and scattered fields are then determined for the appropriate boundary conditions. Finally, the scalar potentials can be used to obtain the fields inside and outside the sphere.

2.2.1 Maxwell's Equations

The four Maxwell equations are:

$$\nabla \times \bar{H} = \frac{1}{c}\frac{\partial \bar{D}}{\partial t} + \frac{4\pi \bar{I}}{c} \tag{2.1}$$

$$\nabla \times \bar{E} = -\frac{1}{c}\frac{\partial \bar{B}}{\partial t} \tag{2.2}$$

$$\nabla \cdot \bar{D} = 4\pi\rho \tag{2.3}$$

$$\nabla \cdot \bar{B} = 0 \tag{2.4}$$

where $\bar{H}$ is the magnetic field strength, $\bar{D}$ the electric displacement given by $\bar{D} = \epsilon\bar{E}$, $\bar{I}$ the current density given by $\bar{I} = \sigma\bar{E}$, $\bar{E}$ the electric field strength, ϵ the dielectric constant, σ the conductivity, ρ the charge density and $\bar{B}$ the magnetic induction given by $\bar{B} = \mu\bar{H}$.[2]

By taking the divergence of both sides of Eq. 2.1 and since $\nabla \cdot \nabla \times \bar{H} = 0$, we have:

$$4\pi\ \nabla \cdot \bar{I} + \frac{\partial}{\partial t}\nabla \cdot \bar{D} = 0 \tag{2.5}$$

and by combining Eq. (2.3),

$$\nabla \cdot \bar{I} + \frac{\partial \rho}{\partial t} = 0 \tag{2.6}$$

This is the equation of continuity of the electromagnetic field.

2.2.2 Solution of the Electromagnetic Equation

We first consider a plane electromagnetic wave with angular frequency ω so we can express $\bar{H}$ and $\bar{E}$ as follows:

$$\bar{H} \rightarrow \bar{H}\mathrm{e}^{i\omega t} \tag{2.7a}$$

$$\bar{E} \rightarrow \bar{E}\mathrm{e}^{i\omega t} \tag{2.7b}$$

[2]Magnetic permeability μ is made to be equal to 1 for the purposes of the calculations shown in this section.

This allows us to assume the simpler forms:

$$\nabla \times \bar{H} = ikm^2\bar{E} \tag{2.8a}$$

$$\nabla \times \bar{E} = -ik\bar{H}, \tag{2.8b}$$

where $k = \omega/c$ is the wavenumber and m is the complex refractive index of the medium at the frequency ω and the permeability $\mu \approx 1$ for air.
By taking the curl of Equations 2.8a and 2.8b and using the identity $\nabla \times \nabla \times \bar{A} = \nabla(\nabla \cdot \bar{A}) - \nabla^2\bar{A}$ we obtain:

$$\nabla^2\bar{H} = -k^2m^2\nabla \cdot \bar{H} \tag{2.9a}$$

$$\nabla^2\bar{E} = -k^2m^2\nabla \cdot \bar{E} \tag{2.9b}$$

The above equations indicate that the components of the magnetic induction $\bar{H}$ and electric vector $\bar{E}$, in a homogeneous medium, must satisfy the scalar wave equation:

$$\nabla^2\psi + k^2m^2\psi = 0 \tag{2.10}$$

with the simplest solution being a plane wave.
The scalar wave equation Eq. 2.10 can be separated in spherical coordinates (ρ, θ, ϕ) and can have solutions of the type:

$$\Phi(\phi) = a_\ell \cos \ell\phi + b_\ell \sin \ell\phi \tag{2.11a}$$

$$\Theta(\theta) = P_\ell^n(\cos\theta) \tag{2.11b}$$

$$R(\rho) = \sqrt{\frac{\pi}{2\rho}} Z_{\ell+1/2}(\rho) \tag{2.11c}$$

where a_ℓ and b_ℓ are arbitrary constants, $\rho = mkr$, $P_\ell^n(\cos\theta)$ the associated Legendre polynomials (spherical harmonics of the first kind) and $Z_{\ell+1/2}(\rho)$ general cylindrical functions of order $\ell + \frac{1}{2}$.

The wave function at all points at the surface of a sphere is then given by:

$$\psi(r,\theta,\phi) = (a_\ell \cos \ell\phi + b_\ell \sin \ell\phi) P_\ell^n(\cos\theta) \sqrt{\frac{\pi}{2\rho}} Z_{\ell+1/2}(\rho) \tag{2.12}$$

The cylindrical functions that appear in Eq. 2.11c can be expressed as the combination of Bessel and Neumann functions, $J_{\ell+1/2}(\rho)$ and $N_{\ell+1/2}(\rho)$ respectively. Even though Bessel functions are regular on the ρ-plane including the origin, Neumann functions become infinite at the origin. Therefore we will be using only Bessel functions to represent the waves incident and inside the sphere.

If ψ is a solution of the scalar wave function then the vector wave function must be satisfied by:

$$\begin{aligned} \bar{M}_\psi &= \nabla \times (\bar{r}\psi) \\ &= \frac{1}{r\sin\theta}\frac{\partial(r\psi)}{\partial\phi} - \frac{1}{r}\frac{\partial(r\psi)}{\partial\theta} \end{aligned} \tag{2.13a}$$

$$\begin{aligned} mk\bar{N}_\psi &= \nabla \times (\bar{M}_\psi) \\ &= \left[\frac{\partial^2(r\psi)}{\partial r^2} + m^2k^2 r\psi\right] + \frac{1}{r}\frac{\partial^2(r\psi)}{\partial r\partial\theta} \\ &+ \frac{1}{r\sin\theta}\frac{\partial^2(r\psi)}{\partial r\partial\phi} \end{aligned} \tag{2.13b}$$

If u and v are two orthogonal solutions to the scalar wave equation then the electric and magnetic vectors $\bar{E}$ and $\bar{H}$ can be expressed as:

$$\bar{E} = \bar{M}_v + i\bar{N}_u \tag{2.14a}$$

$$\bar{H} = m(-\bar{M}_u + i\bar{N}_v) \tag{2.14b}$$

which satisfy Equations 2.8a and 2.8b. By combining Equations 2.13 and 2.14

we can write $\bar{E}$ and $\bar{H}$ as:

$$\begin{aligned}\bar{E} =& \frac{i}{mk}\left[\frac{\partial^2(ru)}{\partial r^2} + m^2k^2ru\right]\hat{r} \\ &+ \left[\frac{1}{r\sin\theta}\frac{\partial(ru)}{\partial\phi} + \frac{i}{mkr}\frac{\partial^2(ru)}{\partial r\partial\theta}\right]\hat{\theta} \\ &+ \left[-\frac{1}{r}\frac{\partial(ru)}{\partial\theta} + \frac{i}{mkr\sin\theta}\frac{\partial^2(ru)}{\partial r\partial\phi}\right]\hat{\phi}\end{aligned} \tag{2.15}$$

$$\begin{aligned}\bar{H} =& \frac{i}{k}\left[\frac{\partial^2(rv)}{\partial r^2} + m^2k^2rv\right]\hat{r} \\ &+ \left[-\frac{m}{r\sin\theta}\frac{\partial(rv)}{\partial\phi} + \frac{i}{kr}\frac{\partial^2(rv)}{\partial r\partial\theta}\right]\hat{\theta} \\ &+ \left[-\frac{m}{r}\frac{\partial(rv)}{\partial\theta} + \frac{i}{kr\sin\theta}\frac{\partial^2(rv)}{\partial r\partial\phi}\right]\hat{\phi}\end{aligned} \tag{2.16}$$

2.2.3 Scattering Problem Solution

We then consider the simple case where the refractive index of the surrounding medium is $m_{med} = 1$ (vacuum) and the sphere has an arbitrary index of refraction m. The sphere is illuminated by a plane wave which is linearly polarised and propagates along the positive z-axis. The amplitude of the incident wave is normalised to unity and therefore the electric and magnetic field vectors are:

$$\bar{E} = \bar{a}_x \mathrm{e}^{-i(kz-\omega t)} \tag{2.17a}$$

$$\bar{H} = \bar{a}_y \mathrm{e}^{-i(kz-\omega t)} \tag{2.17b}$$

where a_x and a_y are unit vectors along the x- and y- axis respectively.

One can transform from rectangular coordinates to spherical polar coordinates r, θ and ϕ as Figure 2.1 indicates and thus the electric and magnetic fields

become:

$$E_r = \mathrm{e}^{-i(kr\cos\theta-\omega t)}\sin\theta\cos\phi \tag{2.18a}$$

$$E_\theta = \mathrm{e}^{-i(kr\cos\theta-\omega t)}\cos\theta\cos\phi \tag{2.18b}$$

$$E_\phi = \mathrm{e}^{-i(kr\cos\theta-\omega t)}\sin\phi \tag{2.18c}$$

$$H_r = \mathrm{e}^{-i(kr\cos\theta-\omega t)}\sin\theta\sin\phi \tag{2.18d}$$

$$H_\theta = \mathrm{e}^{-i(kr\cos\theta-\omega t)}\cos\theta\sin\phi \tag{2.18e}$$

$$H_\phi = \mathrm{e}^{-i(kr\cos\theta-\omega t)}\cos\phi \tag{2.18f}$$

The non time-dependant part of the first term of the above equations can be rewritten in terms of the Legendre polynomials:

$$\mathrm{e}^{-ikr\cos\theta} = \sum_{\ell=0}^{\infty}(-i)^\ell(2\ell+1)j_\ell(kr)P_\ell(\cos\theta) \tag{2.19}$$

where j_ℓ is the spherical Bessel function.

We also have the identities:

$$\mathrm{e}^{-ikr\cos\theta}\sin\theta = \frac{1}{ikr}\frac{\partial}{\partial\theta}(\mathrm{e}^{-ikr\cos\theta}), \tag{2.20}$$

$$\frac{\partial}{\partial\theta}P_\ell(\cos\theta) = -P_\ell^1(\cos\theta), \qquad P_0^1(\cos\theta) = 0 \tag{2.21}$$

Equation 2.21 relates the Legendre polynomial P_ℓ to the associated Legendre polynomial P_ℓ^1. Using the above identities with Equation 2.19, we have:

$$\mathrm{e}^{-ikr\cos\theta}\sin\theta = \sum_{\ell=1}^{\infty}(-i)^\ell(2\ell+1)j_\ell(kr)P_\ell^1(\cos\theta) \tag{2.22}$$

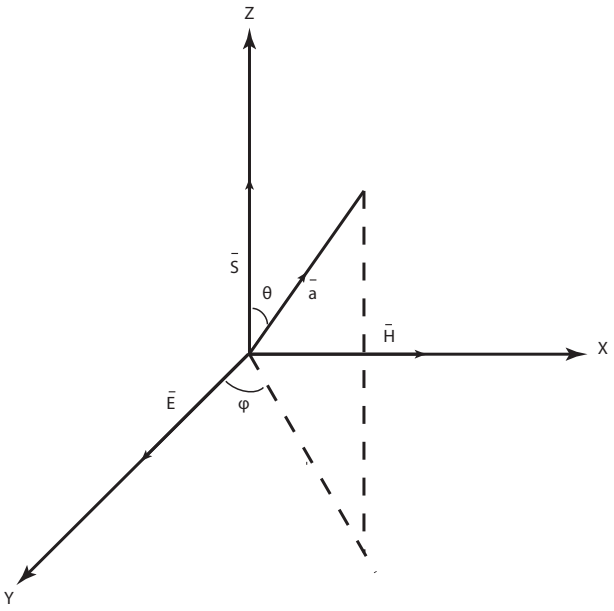

Figure 2.1: Transformation of Cartesian system to spherical coordinates. $\bar{S}$ is the Poynting vector, and $\bar{a}$ is an arbitrary unit vector.

The scalar potential u and v can be determined by only one of the components of Equations 2.15 and 2.16:

$$\begin{aligned} E_r &= \mathrm{e}^{-i(kr\cos\theta)}\sin\theta\cos\phi \\ &= \sum_{\ell=1}^{\infty}(-i)^{\ell}(2\ell+1)j_{\ell}(kr)P_{\ell}^{1}(\cos\theta)\cos\phi \\ &= \frac{i}{mk}\left[\frac{\partial^2(ru)}{\partial r^2}+m^2k^2ru\right] \end{aligned} \tag{2.23}$$

A trial solution for Equation 2.23 for $m_{med}=1$ is:

$$u=\sum_{\ell=1}^{\infty}a_{\ell}j_{\ell}(kr)P_{\ell}^{1}(\cos\theta)\cos\phi \tag{2.24}$$

with $a_{\ell}=(-i)^{\ell}\frac{2\ell+1}{\ell(\ell+1)}$.

Similarly v is derived from Equation 2.16 and we obtain the scalar potentials for the incident field:

$$u_{inc}=\mathrm{e}^{i\omega t}\sum_{\ell=1}^{\infty}(-i)^{\ell}\frac{2\ell+1}{\ell(\ell+1)}j_{\ell}(kr)P_{\ell}^{1}(\cos\theta)\cos\phi \tag{2.25a}$$

$$v_{inc}=\mathrm{e}^{i\omega t}\sum_{\ell=1}^{\infty}(-i)^{\ell}\frac{2\ell+1}{\ell(\ell+1)}j_{\ell}(kr)P_{\ell}^{1}(\cos\theta)\sin\phi \tag{2.25b}$$

The form for the inside and scattered waves have to be similar to the incident wave but with coefficients which satisfy the boundary conditions. As mentioned before we only use Bessel functions for the internal wave since Neumann functions have singularities at the origin. We obtain the following expression for the scalar potential of the internal field of a sphere with refractive index m:

$$u_{int} = \mathrm{e}^{i\omega t} \sum_{\ell=1}^{\infty} m c_\ell (-i)^\ell \frac{2\ell+1}{\ell(\ell+1)} j_\ell(mkr) P_\ell^1(\cos\theta)\cos\phi \tag{2.26a}$$

$$v_{int} = \mathrm{e}^{i\omega t} \sum_{\ell=1}^{\infty} m d_\ell (-i)^\ell \frac{2\ell+1}{\ell(\ell+1)} j_\ell(mkr) P_\ell^1(\cos\theta)\sin\phi \tag{2.26b}$$

Finally, the scattered field solution must vanish at infinity. For this reason we use the second kind Hankel functions because of their asymptotic behaviour to represent the fields expressed by the sphere:

$$u_{scat} = \mathrm{e}^{i\omega t} \sum_{\ell=1}^{\infty} -a_\ell (-i)^\ell \frac{2\ell+1}{\ell(\ell+1)} h_\ell^{(2)}(kr) P_\ell^1(\cos\theta)\cos\phi \tag{2.27a}$$

$$v_{scat} = \mathrm{e}^{i\omega t} \sum_{\ell=1}^{\infty} -b_\ell (-i)^\ell \frac{2\ell+1}{\ell(\ell+1)} h_\ell^{(2)}(kr) P_\ell^1(\cos\theta)\sin\phi \tag{2.27b}$$

where $h_\ell^{(2)}$ is the spherical Hankel function derived from the second kind Hankel functions which are the linear combination of Bessel and Neumann functions:

$$H_{\ell+1/2}^{(2)}(\rho) = J_{\ell+1/2}(\rho) - iN_{\ell+1/2}(\rho) \tag{2.28}$$

For the purpose of determining the coefficients $a_\ell, b_\ell, c_\ell, d_\ell$ we introduce the Riccati-Bessel functions which are the spherical Bessel functions multiplied by a factor z:

$$\psi_\ell(z) = z j_\ell(z) = \sqrt{\frac{\pi z}{2}} J_{\ell+1/2}(z) = S_\ell(z) \tag{2.29a}$$

$$\chi_\ell(z) = -z n_\ell(z) = -\sqrt{\frac{\pi z}{2}} N_{\ell+1/2}(z) = C_\ell(z) \tag{2.29b}$$

$$\zeta_\ell(z) = -z h_\ell^{(2)}(z) = -\sqrt{\frac{\pi z}{2}} H_{\ell+1/2}^{(2)}(z) = S_\ell(z) + iC_\ell(z) \tag{2.29c}$$

The tangential components of $\bar{E}$ and $\bar{H}$ must be continuous at the surface, $r = \alpha$, with α being the radius of the sphere.

$$u_{inc} + u_{scat} = m u_{int} \tag{2.30a}$$
$$\frac{\partial}{\partial r}\left[r(u_{inc} + u_{scat})\right] = \frac{1}{m}\frac{\partial}{\partial r}(r u_{int}) \tag{2.30b}$$
$$v_{inc} + v_{scat} = v_{int} \tag{2.30c}$$
$$\frac{\partial}{\partial r}\left[r(v_{inc} + v_{scat})\right] = \frac{\partial}{\partial r}(r v_{int}) \tag{2.30d}$$

We set the following parameters:

$$x = k\alpha = \frac{2\pi\alpha}{\lambda}, \qquad y = mk\alpha$$

Hence the boundary conditions can be written as:

$$\psi_\ell(x) - a_\ell \zeta_\ell(x) = m c_\ell \psi_\ell(y) \tag{2.31a}$$
$$\psi'_\ell(x) - a_\ell \zeta'_\ell(x) = m c_\ell \psi'_\ell(y) \tag{2.31b}$$
$$\psi_\ell(x) - b_\ell \zeta_\ell(x) = m d_\ell \psi_\ell(y) \tag{2.31c}$$
$$\psi\prime_\ell(x) - b_\ell \zeta'_\ell(x) = m d_\ell \psi'_\ell(y) \tag{2.31d}$$

Combining the above equations we obtain the expressions for the coefficients:

$$a_\ell = \frac{\psi'_\ell(y)\psi_\ell(x) - m\psi_\ell(y)\psi'_\ell(x)}{\psi'_\ell(y)\zeta_\ell(x) - m\psi_\ell(y)\zeta'_\ell(x)} \tag{2.32}$$
$$b_\ell = \frac{m\psi'_\ell(y)\psi_\ell(x) - \psi_\ell(y)\psi'_\ell(x)}{m\psi'_\ell(y)\zeta_\ell(x) - \psi_\ell(y)\zeta'_\ell(x)} \tag{2.33}$$
$$c_\ell = \frac{m\left[\psi'_\ell(x)\zeta_\ell(x) - \psi_\ell(x)\zeta'_\ell(x)\right]}{\psi'_\ell(y)\zeta_\ell(x) - m\psi_\ell(y)\zeta'_\ell(x)} \tag{2.34}$$
$$d_\ell = \frac{m\left[\psi'_\ell(x)\zeta_\ell(x) - \psi_\ell(x)\zeta'_\ell(x)\right]}{m\psi'_\ell(y)\zeta_\ell(x) - \psi_\ell(y)\zeta'_\ell(x)} \tag{2.35}$$

This completes the solution of the scattering problem of a homogeneous sphere with radius α and refractive index m. The fields inside and outside the sphere are expressed in known functions.

2.3 Single Particle Scattering Simulations

In this section we present computational calculations for GLMT based on the expressions derived in the previous chapter. The results include illustrations of the fields inside and outside dielectric spheres for different beam configurations and profiles. We will discuss the generation of the beam shape coefficients in Section 2.3.3. The illustrations shown in this section are for the case of a 1 μm diameter sphere with refractive index $n_{sph} = 1.45$ immersed in water $n_{water} = 1.33$.[3]

In order to illustrate the fields involved in the scattering problem, we used the scalar potentials given in Equations 2.25, 2.26 and 2.27 for the incident, internal and scattered fields respectively.
These expressions were calculated for a number of terms n_{terms} which depends on particle size as suggested by W. J. Wiscombe [39].

$$\ell_{terms} = \begin{cases} kx + 4(kx)^{1/3} + 1, & 0.02 \leq kx \leq 8 \\ kx + 4.05(kx)^{1/3} + 2, & 8 < kx < 4200 \\ kx + 4(kx)^{1/3} + 2, & 4200 \leq kx \leq 20000 \end{cases} \tag{2.36}$$

where k is the wave vector and x is the distance over which the fields are calculated. Spherical Bessel functions of order $\ell > \ell_{terms}$ are almost equal to zero for $r \leq \alpha$, where α is the radius of the sphere. Therefore they do not have a significant effect on the fields on the surface of the sphere. Also the scattering coefficients (Equations 2.32, 2.33, 2.34, 2.35) become negligible for $r > \alpha$ for $\ell > \ell_{terms}$.

The corresponding electric fields could then be determined by using Equation 2.14a. Finally the intensity of the electric fields was found by $I = \bar{E} \cdot \bar{E}^*$ and plotted for the xy, xz and yz planes.

[3]The parameters used for these simulations i.e. laser wavelength and the refractive indices for the sphere and immersion medium [37, 38] are chosen to match the ones used during experiments as presented in Chapter 4.

2.3.1 Plane Wave

First, we start with the simplest configuration which is the one where the incident field is a unit amplitude plane wave. The sphere is immersed in water, $n_{water} = 1.33$, and is located at the origin $x = 0$, $y = 0$ and $z = 0$. It is illuminated by a plane wave propagating in the z-direction and polarised in the x-direction with wavelength λ=1064 nm. The results of the calculations using these parameters are presented in Figure 2.2.

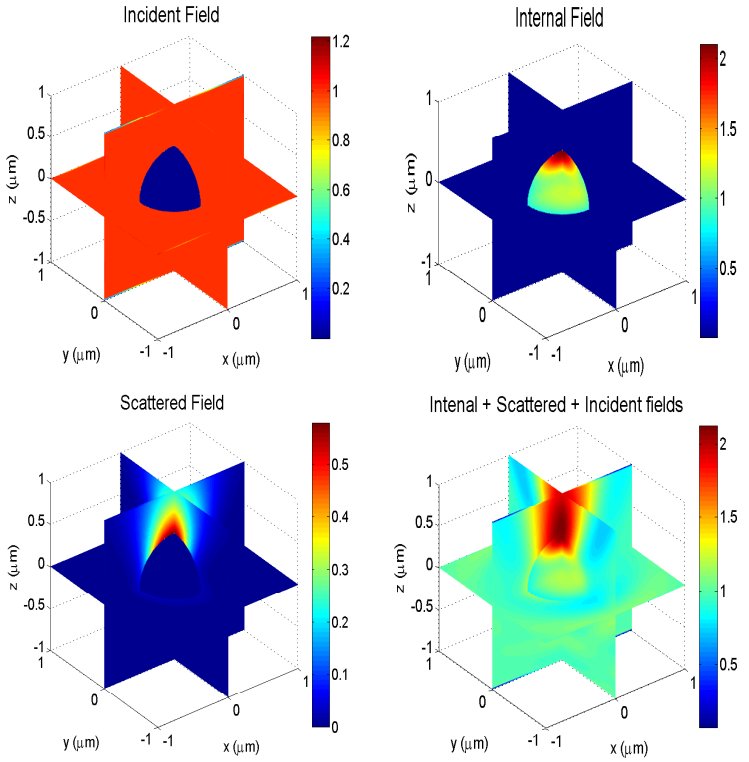

Figure 2.2: 1 μm diameter sphere with $n_{sph} = 1.45$ immersed in water, $n_{water} = 1.33$ and illuminated by a plane wave, λ=1064 nm, propagating in the z-direction and polarised in the x-direction. Top left: incident plane wave, top right: field inside the sphere, bottom left: scattered field from the surface of the sphere, bottom right: all fields combined.

An intensity maximum in the forward scattering direction can be observed and clearly shown in Figure 2.3. Similar to the intensity maximum of the focused beam used in optical tweezers, this intensity 'hot spot' may be expected to act as an optical trap for a nearby particle, resulting in an optically mediated attractive force between the two particles.

We have checked if the position of the intensity maximum coincides with the

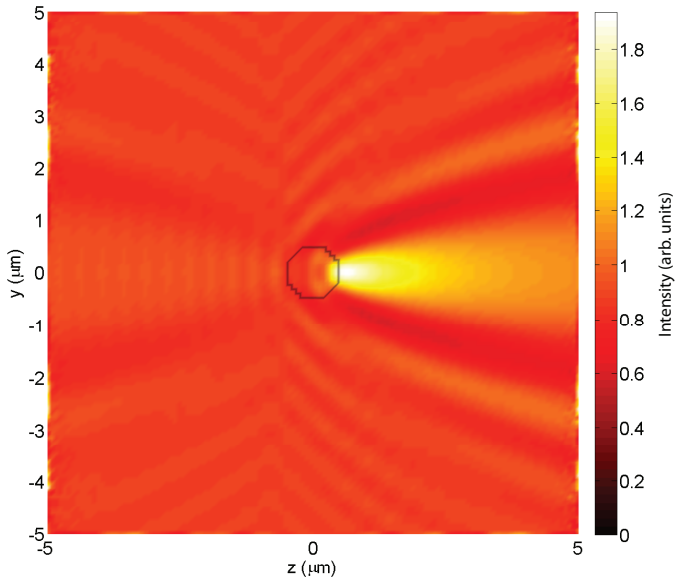

Figure 2.3: Intensity maximum in the forward scatter direction for the case of 1 μ m sphere and incident wavelength $\lambda = 1064$ nm.

focal length predicted by McGloin's *et al.* in 2004 and Metzger's *et al.* [16, 17] approach as mentioned in Section 1.2.2.2. Using the expression for the focal length of a ball lens,

$$f = \frac{\alpha}{2\Delta n} \tag{2.37}$$

and inserting the parameters used for the simulations we obtain $f = 2.0$ μm. This does not agree with the simulation value as Figure 2.4 shows. The intensity maximum as obtained from the above plot is located at 0.6 μm from the centre of the sphere. This is due to the fact that treating the sphere as a ball lens, using ray optics, is not an accurate approach when the sphere size becomes really small. This is also in contrast with experimental results that will be presented in Chapter 4.

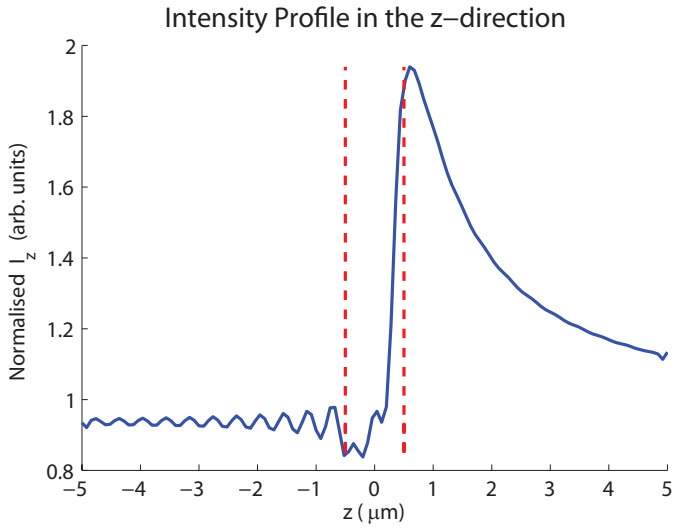

Figure 2.4: Intensity profile in the z-direction. The dashed lines represent the edges of the sphere. Small backscattering leading to the modulation of intensity for negative z is observed, but strong forward scattering, so it may be expected that another nearby particle will be attracted to the intensity maximum in the forward-scattered direction.

2.3.2 Counter Propagating Plane Waves

2.3.2.1 Parallel Polarisations

Next we calculate the internal and external fields for two counter propagating plane waves being incident on the sphere and are presented in Figure 2.5. The plane waves propagate in the ±z-directions and are polarised in the x-direction. When the wave propagating along the +z direction, it scatters through the angles θ and ϕ. Therefore the wave travelling in the opposite direction has to scatter through $\pi - \theta$ and $-\phi$. In this case we observe the formation of two intensity hot spots in both z-directions.

In counter-propagating beams of parallel linear polarisations, an interference pattern is formed which is additionally modified by the forward scatter from the particle in the direction of propagation of the two beams as shown in Figure 2.6. In this case we can understand optical binding and the observed 1D chain formation parallel to the direction of propagation (see also later experiments in Chapter 4) as the forward scatter in each direction from each particle attracts and binds adjacent particles into the chain.

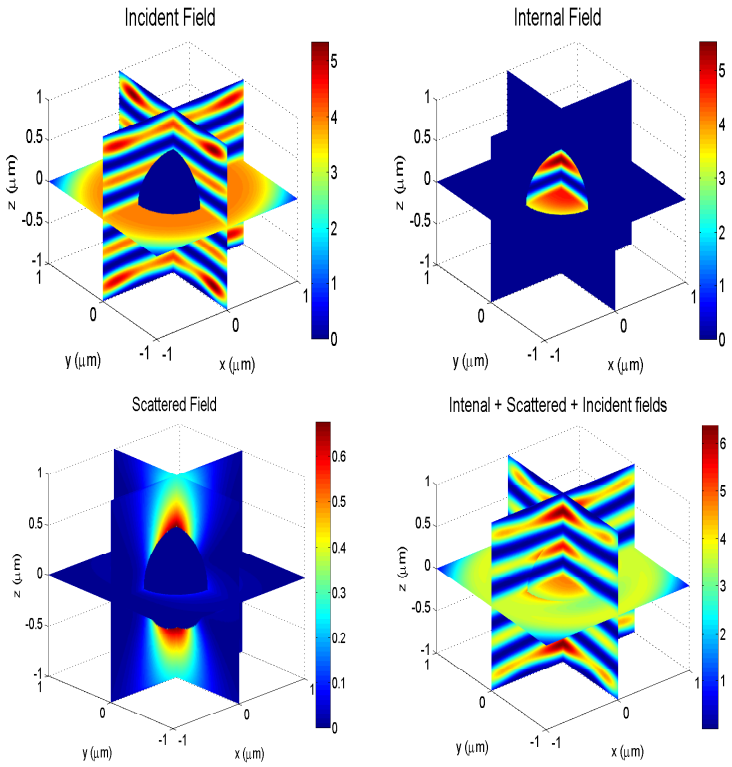

Figure 2.5: 1 μm diameter sphere with $n_{sph} = 1.45$ immersed in water, $n_{water} = 1.33$ and illuminated by two counter propagating plane waves, $\lambda = 1064$ nm, with parallel polarisations.

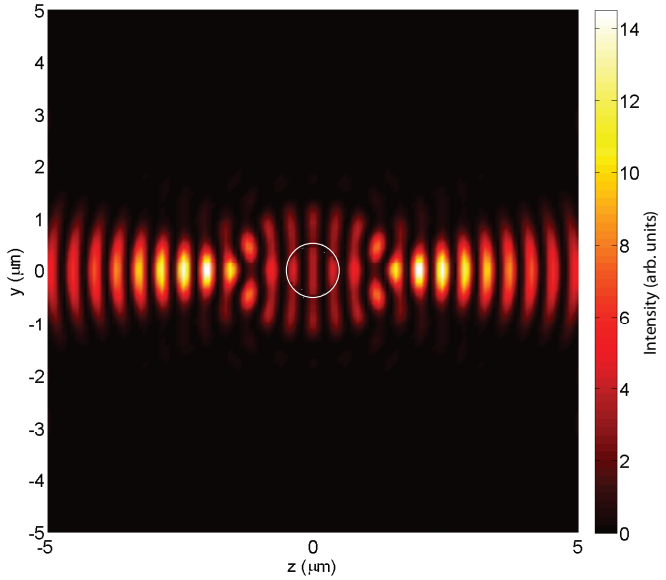

Figure 2.6: Counter-propagating plane waves polarised in the x-direction and propagating in the ±z-directions, showing the modulation of the linear fringe patter due to forward scattering in the ±z-directions.

2.3.2.2 Perpendicular Polarisations

The Mie theory calculations were also made for the configuration where the two beams are cross-polarised as shown in Figure 2.7. In this case there is no interference pattern formed. Hence the intensity maxima in both directions are not enhanced as in the previous case. The attractive force between nearby particles is expected to be weaker using this configuration although we may still expect optical binding to occur.

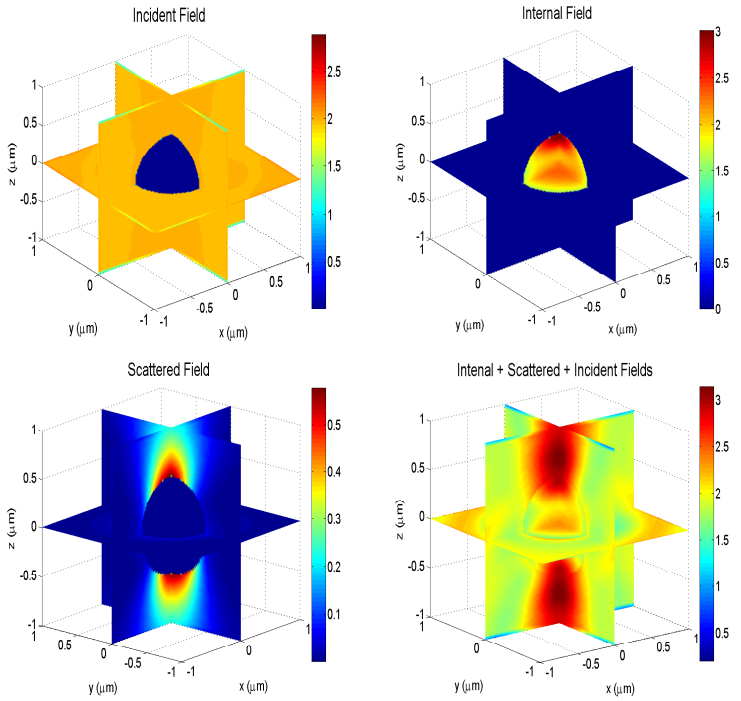

Figure 2.7: 1 μm diameter sphere with $n_{sph} = 1.45$ immersed in water, $n_{water} = 1.33$ and illuminated by two counter propagating plane waves, $\lambda = 1064$ nm, with orthogonal polarisations in the x- and y- directions.

2.3.3 Gaussian Beam Profile

In order to match the conditions used in experiments, we needed to shape the beam to a Gaussian profile in the simulations. This can be done be making use of the orthogonality relations successively for the Legendre Polynomial and

Bessel function terms [40, 41] :

$$\int_0^{\pi} P_n^m(\cos\theta) P_\ell^m(\cos\theta)\sin\theta d\theta = \frac{2}{2n+1}\frac{(n+m)!}{(n-m)!}\delta_{nl} \tag{2.38a}$$

$$\int_0^{\infty} \psi_n^1(kr)\psi_1^m(kr)d(kr) = \frac{\pi}{2(2n+1)}\delta_{nm} \tag{2.38b}$$

The amplitudes g_n are determined at the lowest order L^- of approximation which holds for small values of $1/kw$ and for small displacements of the scattering sphere from the beam axis [42]:

$$g_\ell = \frac{2\ell+1}{\pi\ell(\ell+1)}\frac{1}{(-1)^\ell i^\ell}\int_0^{\pi}\int_0^{\infty} ikr\sin^2\theta\ f\ \exp(-\mathrm{ikr}\cos\theta) \\ \psi_\ell^1(kr)P_\ell^1(\cos\theta)d\theta d(kr) \tag{2.39}$$

For a Gaussian beam polarised in the x-direction and propagating in the z-direction, f is defined as:

$$f = \mathrm{e}^{-ikz}\ \mathrm{e}^{-(x/w)^2} \tag{2.40}$$

where w is the beam parameter at the waist. We finally multiply Equations 2.25, 2.26 and 2.27 with the amplitudes g_ℓ which are shown in Figure 2.8.

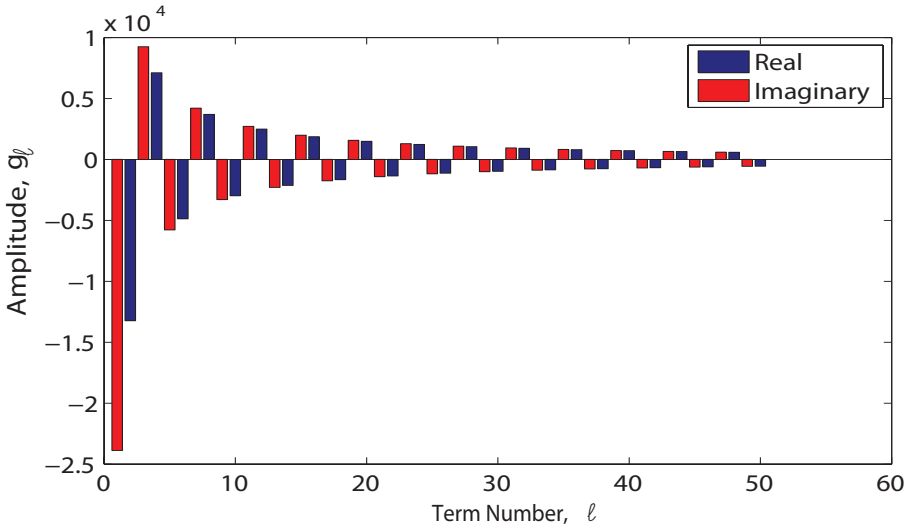

Figure 2.8: The amplitudes of the real and imaginary parts of g_ℓ, of the terms in the expansion for the scalar potential in the Mie scattering calculations for $P = 1$ W and beam width $w = 50$ μm.

The results obtained are shown in Figure 2.9. It can be clearly seen that the results are similar to the ones obtained for a plane wave of uniform intensity

as in Figure 2.2. We can safely assume that calculations made for plane waves are a good approximation to Gaussian beams.

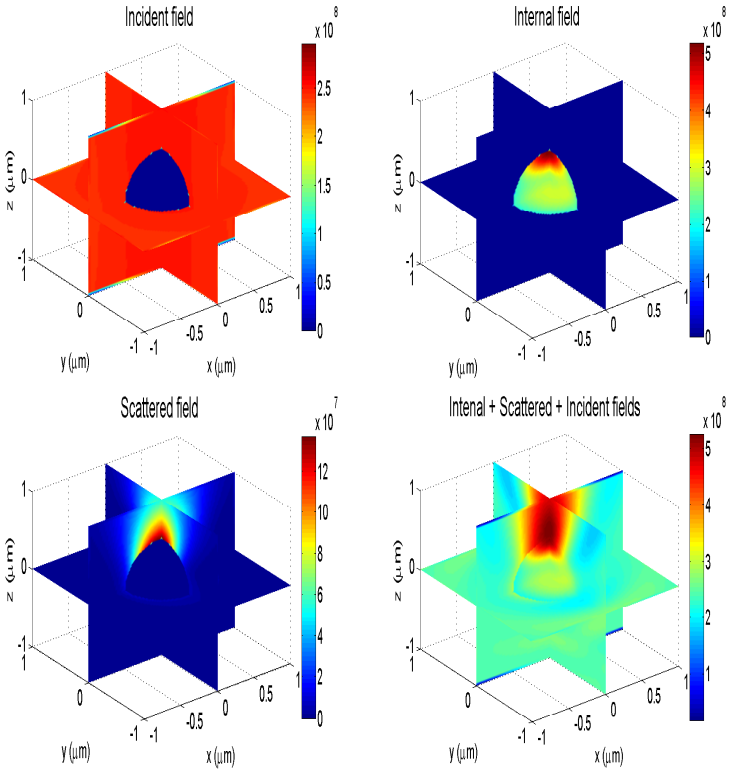

Figure 2.9: 1 μm diameter sphere with $n_{sph} = 1.45$ immersed in water, $n_{water} = 1.33$ and illuminated by a Gaussian beam, propagating in the z-direction and polarised in the x-direction.

2.3.4 Evanescent Waves

Total internal reflection (TIR) occurs when a light beam is incident on the interface of an optically less-dense medium at an angle greater than the critical angle. The critical angle can be derived from Snell's law when the angle of refraction is set to be equal to 90°as shown in the following equation:

$$n_1 \sin\theta_i = n_2 \sin\theta_r, \tag{2.41}$$

where n_1 and n_2 are the refractive indices of the two media and θ_i and θ_r are the angles of incidence and refraction respectively. Therefore the critical angle for $n_1 > n_2$ is given by:

$$\theta_{crit} = \arcsin\frac{n_2}{n_1}, \tag{2.42}$$

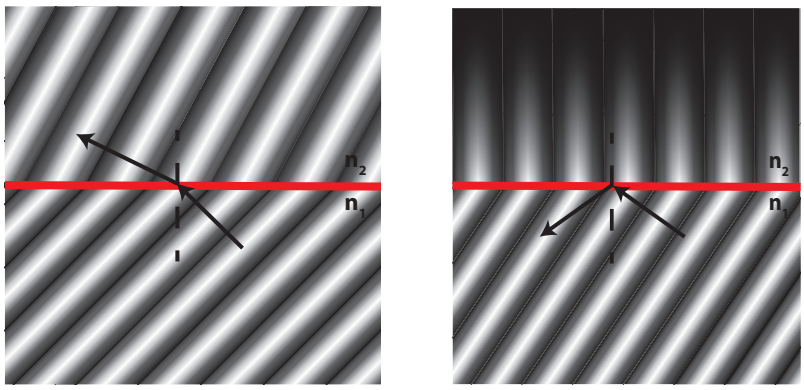

(a) **(b)**

Figure 2.10: Refraction of a plane wave at a dielectric interface: (a)wave is incident at an angle smaller than $\theta_{crit.}$ and is refracted (b) wave is incident at an angle greater than $\theta_{crit.}$ and an evanescent field is formed in the upper medium.

Even though there is no propagating light beam through the optically less-dense medium, there exists an electric field which penetrates a short distance from the surface and only transmits power parallel to the interface. It decays exponentially away from the interface and for that reason is called evanescent wave. The amplitude of this field is given by:

$$E_{zt} = E_0 \exp[-k_t(\frac{\sin^2\theta_i}{(n_2/n_1)^2} - 1)^{1/2} z], \tag{2.43}$$

where k_t is the wave number of the travelling wave in the transmitted medium. The penetration depth of the field is of the order of the optical wavelength and can be expressed as:

$$\Lambda = \frac{\lambda_0}{2\pi n_2[\frac{\sin^2\theta_i}{(n_2/n_1)^2} - 1]^{1/2}} \tag{2.44}$$

The wavefronts are plane, and provided that we are near critical angle incidence the variation in intensity across the particle is small, so the above free-space calculation is a reasonable model to gain insight into the scattering process that leads to optical binding. A full description would require a self-consistent model accounting for not only multiple scattering between two (or more) spheres, that is, the field incident on each sphere includes the field scattered by all other spheres, but also the field reflected from the adjacent planar surface.

2.4 Force on a Scatterer

In this section we will discuss the forces on a spherical particle that arise from their interaction with electromagnetic waves upon scattering. We will consider uniform plane waves that are being scattered by spherical particles whose size varies. This provides an insight to experiments that will be presented in Chapter 4.

The force on a scatterer due to scattering is given by [43]:

$$F = 2Ne\sigma \tag{2.45}$$

where N is the number of photons per unit volume in the incident beam, e the energy per photon and σ the effective scatterer area. If the scatterer is illuminated by coherent counter propagating beams then the force on it becomes:

$$F = 2NeA \sin 2kb \tag{2.46}$$

where A is the effective area, k the wavenumber and b the distance from the centre of the scatterer to an intensity maximum. With these expressions in mind we have calculated the forces for different configurations.

2.4.1 Force on a Dielectric Sphere

First, we examine the case of a dielectric sphere that is being illuminated by a single plane wave. We make use of the transverse components of the scattered wave as in Equation 2.15. We can rewrite these components as:

$$E_\theta = \frac{1}{ikr} \mathrm{e}^{-i(kz-\omega t)} \cos\phi \, S_2(\theta) \tag{2.47a}$$

$$E_\phi = -\frac{1}{ikr} \mathrm{e}^{-i(kz-\omega t)} \sin\phi \, S_1(\theta) \tag{2.47b}$$

with S_1 and S_2:

$$S_1 = \sum_{\ell=1}^{\infty} \frac{2\ell+1}{\ell(\ell+1)}[a_\ell \pi_\ell + b_\ell \tau_\ell] \tag{2.48a}$$

$$S_2 = \sum_{\ell=1}^{\infty} \frac{2\ell+1}{\ell(\ell+1)}[a_\ell \tau_\ell + b_\ell \pi_\ell] \tag{2.48b}$$

a_ℓ and b_ℓ are the scattering coefficients given by Equations 2.32 and 2.33. The functions π_ℓ and τ_ℓ can be expressed as:

$$\pi_\ell = \frac{l+1}{1-\cos^2\theta}(P_\ell \cos\theta - P_{\ell+1}) \tag{2.49a}$$

$$\tau_\ell = \ell(\ell+1)P_\ell - \pi_\ell \, cos\theta \tag{2.49b}$$

The total scattering cross section is then:

$$\sigma_s = \frac{\pi}{k^2}\int_{-1}^{1}(|S_1|^2 + |S_2|^2)d(\cos\theta) \tag{2.50}$$

The extinction cross-section σ_e is the sum of the absorbing and scattering cross-sections σ_a and σ_s. For the case of a non-absorbing scatterer the cross-section for the radiation pressure is [31]:

$$\sigma_p = [1 - \langle\cos\theta\rangle]\sigma_s \tag{2.51}$$

The force on a dielectric sphere due to a single beam as its radius increases is shown in Figure 2.11 for a beam power of 0.5 W. This force is in the direction of propagation of beam and increases with the size parameter ka.

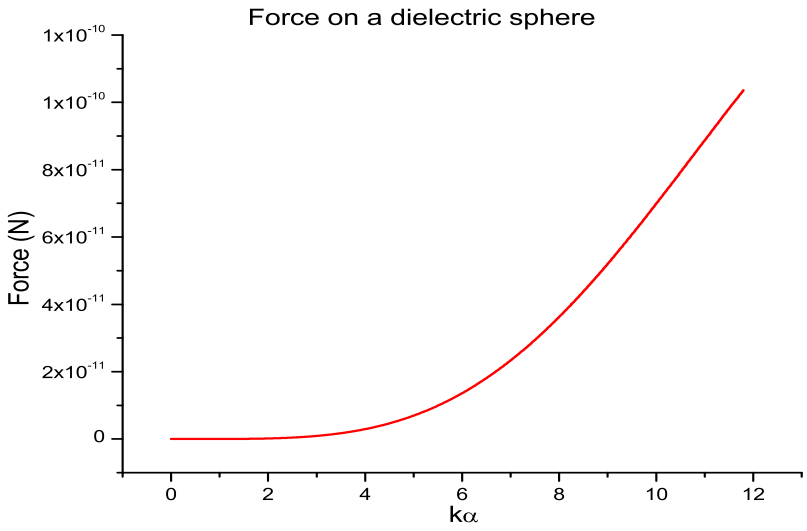

Figure 2.11: Force on a dielectric sphere illuminated by a single plane wave ($\lambda = 1064$ nm) and beam power of 0.5 W. The force is in the direction of propagation of the beam.

2.4.2 Force on a Dielectric Sphere in Counter Propagating Beams

Next, we consider the case where a dielectric particle is in a counter propagating beam configuration, propagating in the positive and negative z-directions. We can replace Equations 2.48a and 2.48a with:

$$T_1 = \sum_{\ell=1}^{\infty} \frac{2\ell+1}{\ell(\ell+1)} [a_\ell m_\ell \pi_\ell + b_\ell p_\ell \tau_\ell] \tag{2.52a}$$

$$T_2 = \sum_{\ell=1}^{\infty} \frac{2\ell+1}{\ell(\ell+1)} [a_\ell m_\ell \tau_\ell + b_\ell p_\ell \pi_\ell] \tag{2.52b}$$

The factors m_ℓ and p_ℓ that have been introduced here is to account for the phase factors $\mathrm{e}^{-i\beta}$ and $\mathrm{e}^{i\beta}$ with $\beta = kb$ relative to the origin. Namely:

$$m_\ell = \mathrm{e}^{-i\beta} + (-1)^{l+1} \mathrm{e}^{i\beta} \tag{2.53a}$$

$$p_\ell = \mathrm{e}^{-i\beta} + (-1)^{\ell} \mathrm{e}^{i\beta} \tag{2.53b}$$

The momentum transfer effective cross-section is then:

$$\tilde{\sigma}_p = \frac{-2\pi}{k^2} \int_{-1}^{1} \cos\theta(|T_1|^2 + |T_2|^2) d(\cos\theta) \tag{2.54}$$

The force acting on a dielectric sphere in such configuration as function of the parameter $k\alpha$ is shown in Figure 2.12. For this calculation the sphere is centred on a fringe maximum. When the force is positive the sphere is attracted to a bright fringe (e.g $k\alpha = 2.5$). In turn a negative force indicates an attraction to a dark fringe (e.g $k\alpha = 3.6$). For some size parameters the force acting on the sphere is zero (e.g $k\alpha = 2.9$).

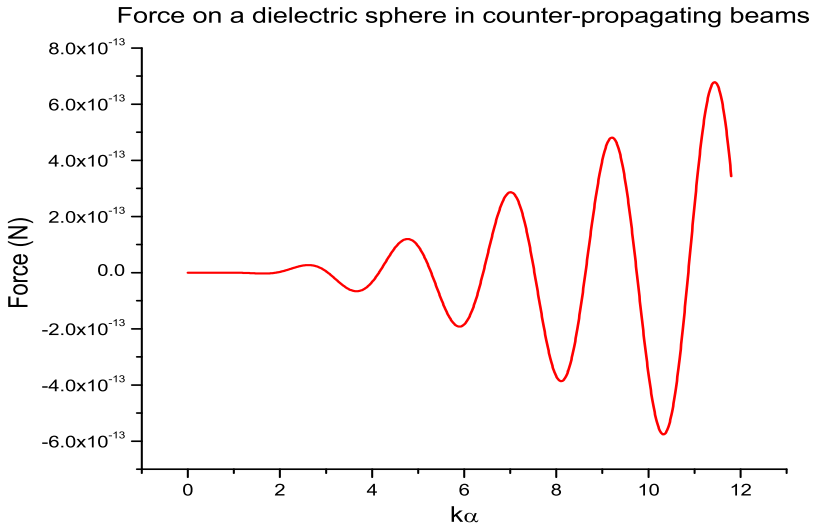

Figure 2.12: Force on a dielectric sphere in counter-propagating plane waves ($\lambda = 1064$ nm). The sphere is located on a fringe maximum. A positive force indicates that the sphere is attracted to a bright fringe and a negative force to a dark fringe.

2.5 Outlook

In this chapter the Generalized Lorentz-Mie Theory of light scattering by a homogeneous sphere has been presented. The theory starts with Maxwell's equations which were used to derive the vector wave equations for an electromagnetic field. The solutions to the vector wave equation are two scalar potentials that satisfy the scalar wave equation. In turn, the solutions to the

scalar wave equation have been expressed in spherical coordinates in terms of spherical Bessel functions and Legendre polynomials. The determination of the coefficients of the internal and scattered fields were determined for the appropriate boundary conditions.

Using the scalar potentials we have simulated the fields inside and outside a homogeneous sphere for different configurations and beam shapes. The intensity along the propagation axis for all cases considered is shown in Figure 2.13. The interference fringes of the counter propagating beams are modulated by the light scattered by the particle, and so at a first level of approximation it may be expected that these spheres form optically bound structures where the particles are trapped at the maxima and separated by distances equal to the fringe spacing.

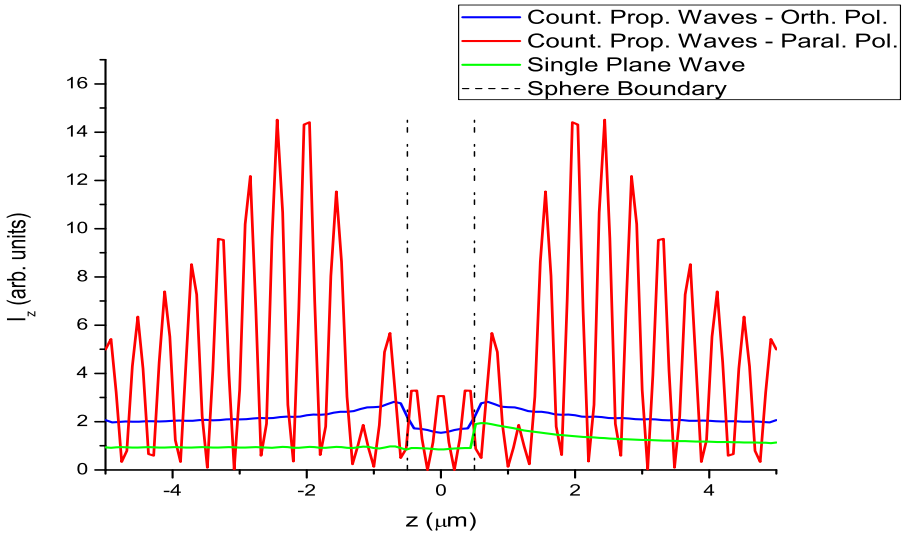

Figure 2.13: Summary of the intensity profile in the z-direction for all cases examined. The calculations are for an 1μm sphere and incident wavelength ($\lambda = 1064$ nm).

Along with the field simulations, we have presented calculations of the force acting on the scattering sphere. These calculations were based on GLMT and provide a better understanding on how the system works. The experiments that will be presented in the next chapters use evanescent fields which can be accurately approximated by the plane wave simulations.

While the above discussion gives a qualitative understanding of the optical binding process several other factors must be accounted for a full description

of the experimental geometry used, including the amplitude variation across the particle of the incident evanescent field, multiple scattering between the particle and the prism (Chapter 4) or tapered fibre surface (Chapter 7), and multiple scattering between the particles in the optically bound structure.

Chapter 3

Evanescent Field Surface Trap: Method

3.1 Introduction

This chapter describes in detail the experimental set-up used to produce the experimental results presented in the following chapter. The experiment consists of the 'Kretschmann configuration' (Figure 1.5) where a prism is used to totally reflect an incoming beam. The evanescent waves generated penetrate a short distance in the medium on top of the prism and confine particles whose size is comparable to the incident wavelength.

In addition, the particle tracking method used for the purposes of these experiments is described. Video microscopy can be utilised to record the Brownian motion of trapped particles using a high resolution CMOS camera [44, 45]. Subsequently, particle tracking software [46] is used to follow the trajectory of the bound particles.

3.2 Experimental Set-up

The experiment is conducted in two parts. The first part consisted of optical binding in counter-propagating evanescent fields formed by total internal reflection at the surface of a Dove prism. The experiment is then extended to use two orthogonal pairs of counter-propagating beams by replacing the Dove prism with an approximately hemispherical lens of the same material. The following sections describe both geometries in detail. An illustration of the general experimental set-up is shown in Figure 3.1.

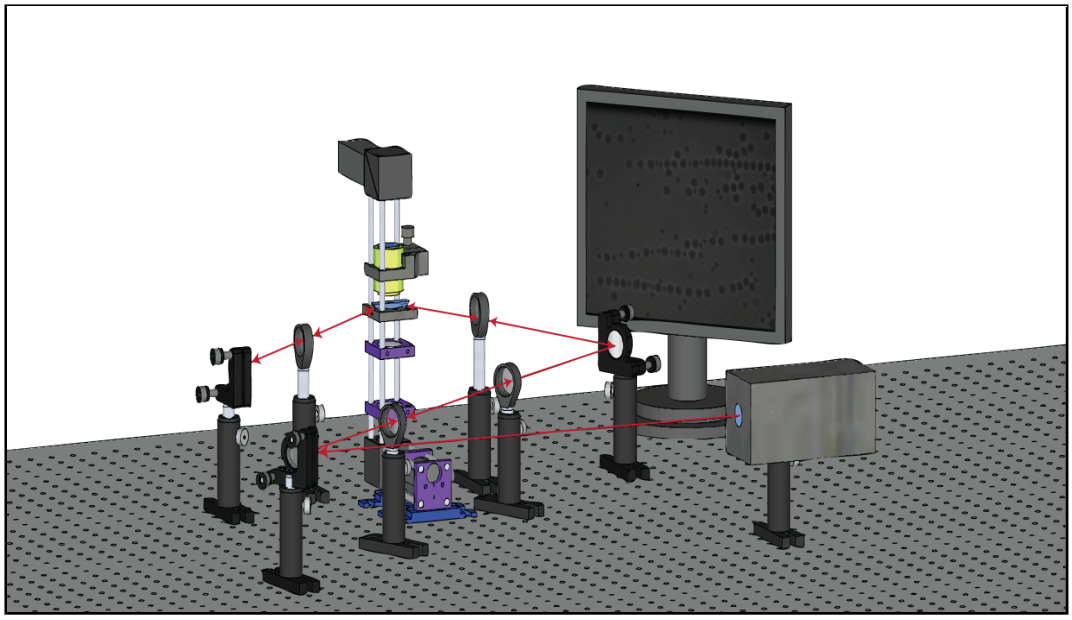

Figure 3.1: 3D Illustration of the experimental set-up for optical manipulation of micro-particles using evanescent waves.

3.2.1 One-dimensional Surface Trap

The evanescent wave surface trapping experiment is realised in a custom-made upright microscope built in a 30 mm cage system. The cage system allowed quick and high precision alignment. A high power white LED array (MWWHL3 by Thorlabs Inc. NJ) acts as an illumination source with the aid of two aspheric lenses as a condenser system (ACL1815-A by Thorlabs Inc. NJ). The illumination light is guided to the upright direction by using a cube-mounted protected silver turning mirror. A custom made stage is used to incorporate a (N-BK7) Dove prism (PS991 by Thorlabs Inc. NJ) which it

is secured by two small clamping arms. A solution (volume 15 μL) containing silica micro particles suspended in deionised water is placed on the upper surface of the glass prism and sealed beneath a microscope cover slip. The solution also includes 10% by volume Triton-X-100 (non-ionic surfactant) to prevent particles sticking on the prism surface. The sealing of the sample is achieved with 9 mm diameter double-sided adhesive spacers (Secure-Seal^{TM}) which create a 0.12 mm deep well. The sample is then sealed with a microscope cover slip.

An Nd:YVO_4 laser system (5-1064-DPSS-2.0-LN by Altechna Co., λ = 1064 nm) with maximum output power of 2 W is used as the laser source. The laser beam is first expanded into a collimated beam with diameter 8 mm by a telescope arrangement. This is done so a tighter focus (and thus stronger confinement of the particles) is achieved at the surface of the prism. The beam is then focused onto the prism-water interface at an angle slightly greater than the critical angle (Figure 3.2) for total internal reflection. The refractive index of N-BK7 glass is $n_{N-BK7} = 1.52$ [47] and therefore the critical angle for the N-BK7 - water interface is calculated to be $\theta_{crit} = 61.3°$ using Snell's Law (Eqn. 2.41).

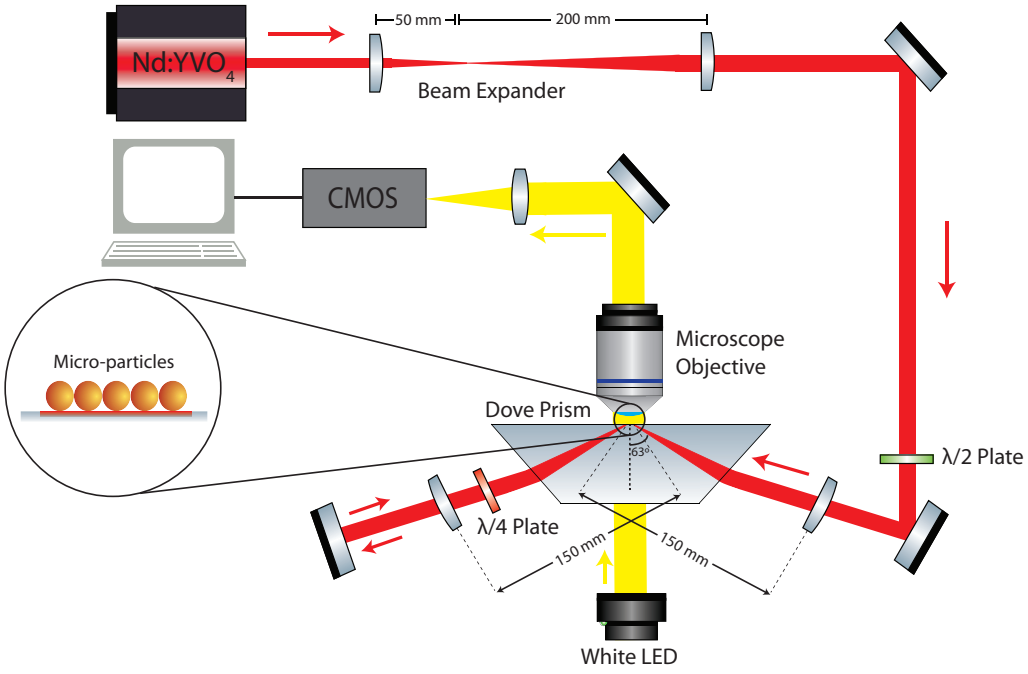

Figure 3.2: Schematic of the experimental set-up used for optical binding experiment.

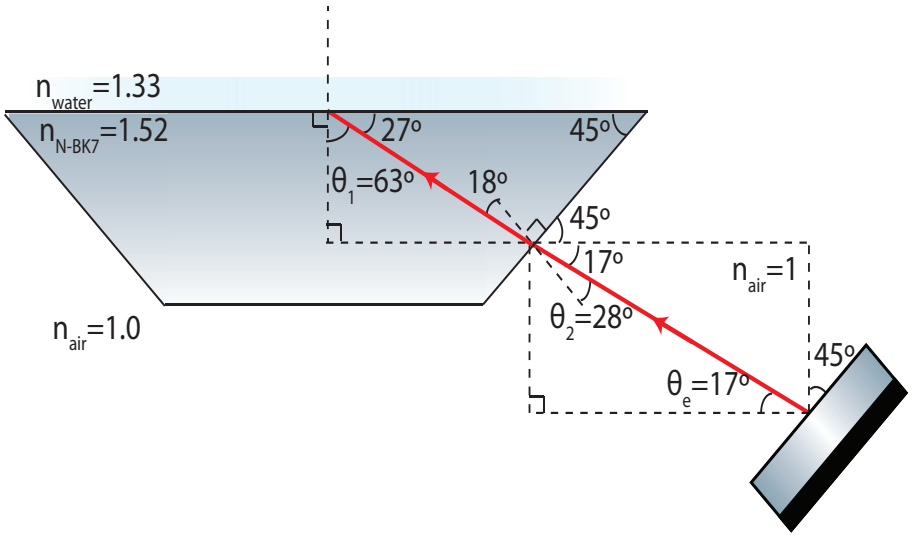

Figure 3.3: Elevation angle determination for the 1D binding set-up. Ray-tracing and Snell's Law were used to calculate the elevation angle for the incident beam in order to achieve slightly above critical angle incidence. The elevation angle from horizontal is $\theta_e = 17°$.

The elevation angle θ_e of the input beam was calculated by starting from the prism-water interface. Since the required angle at that interface must be just above the critical angle, θ_{crit}, it was chosen to be $\theta_1 = 63°$. The angle from the normal on the front face of the Dove prism was calculated to be 18°. By using Snell's Law again for the air-prism interface, the resulting angle θ_2 is 28°. The angle between the upper surface of the Dove prism and faces is 45°. The elevation angle from the horizontal was therefore calculated to be $\theta_e = 17°$ (see Figure 3.3).

A half-wave plate is used to control the polarisation of the incident beam, either s-polarized (perpendicular to interface) or p-polarized (parallel to interface). A 150 mm focal length lens is placed before the microscope to focus the beam on the centre of the top surface of the prism. The lens is inclined so the incoming beam is normal to it to avoid introducing excessive aberrations. The beam is then re-collimated and retro-reflected to create a standing wave and balance the radiation pressure on the micro-particles in the evanescent field. A quarter-wave plate is used to control the polarisation of the retro-reflected beam to be either parallel or perpendicular to the incident beam. The microscope objective is positioned above the crossing point of the two beams on a

z-axis translation mount (SM1Z by Thorlabs Inc. NJ). Lower power microscope objectives (x10 and x40) are used during the alignment of the two beams as they allow a wider field of view. During experiments the sample is imaged using a x100, NA 1.25 oil immersion microscope objective lens (Leica Achro 100/1.25 OIL).

Images and video were recorded with a high resolution (1280×1024 pixels; 3.6 μm pixel size) CMOS camera (DCC1645C by Thorlabs Inc. NJ). The high power LED array allows the capture of high frame rate video as the exposure time of the CMOS camera drops as the frame rate increases. An IR filter is also used when viewing of the particles is desirable in order to block the scattered laser light from the particles and the surface of the prism, to get a clear image of the particles.

In order to obtain the dimensions of the beam size and therefore the overlap region, light scattered by high concentration of micro particles was imaged onto the CMOS camera (Figure 3.4).

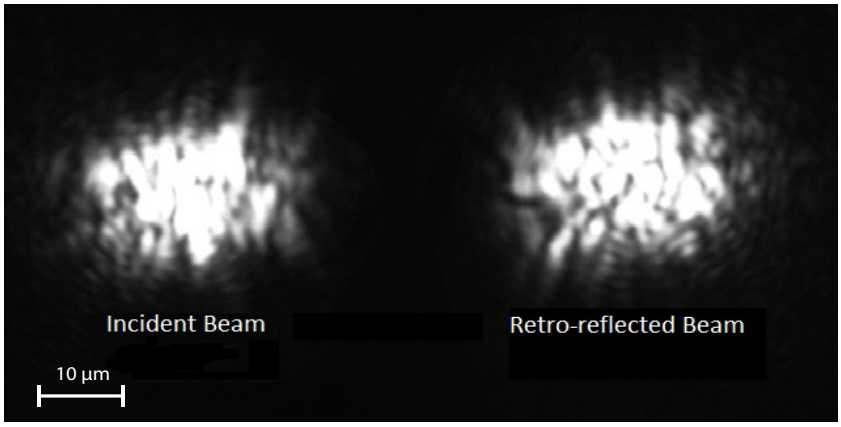

Figure 3.4: Scattered evanescent waves by a group of micro-particles at prism - water interface.

The beam profile was calculated by fitting Gaussians and averaging the widths for a number of frames as recorded using a x4 microscope objective. This is done since the evanescent waves can be only imaged from the forward-scattered light from the sample. The spot size on the prism surface was approximately (45.8 ± 0.4) μm along the x-axis and (41.6 ± 0.7) μm along the y-axis (Figure 3.5). These values compare well to the width of a Gaussian

beam at the focal point as obtained by Gaussian beam analysis, $w = 45$ μm.

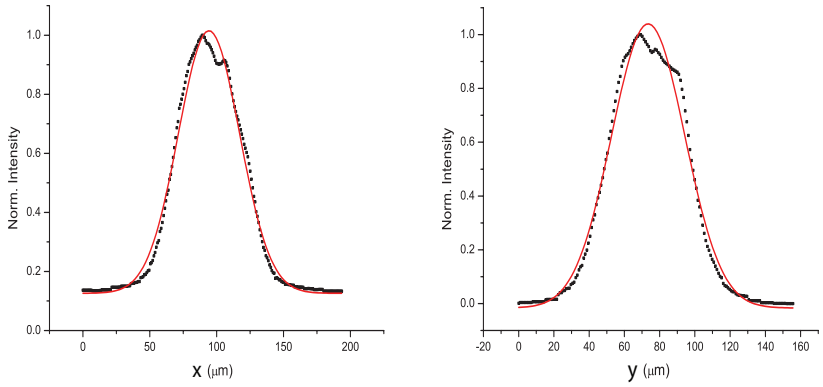

(a) **(b)**

Figure 3.5: Beam profile of the weakly focused beam at the prim-water interface (red curve represents the Gaussian fit on actual data): (a) along x-axis with width $\simeq 23$ μm; (b) along y-axis with width $\simeq 21$ μm.

Gaussian beam analysis was used to ensure that the beam incident on the surface can be well approximated by a plane wave. The analysis includes the Gaussian beam passing through the focusing lens ($f = 150$ mm) and then being incident at the Dove prism top surface. The distance d along the z-axis between the two extremes of the beam at the focal point was calculated to be 155 μm which is much smaller than the Rayleigh range $z_R = \pi w_0^2/\lambda$ for $\lambda = 1.064$ μm and a calculated $w_0 = 45$ μm (Figure 3.6).

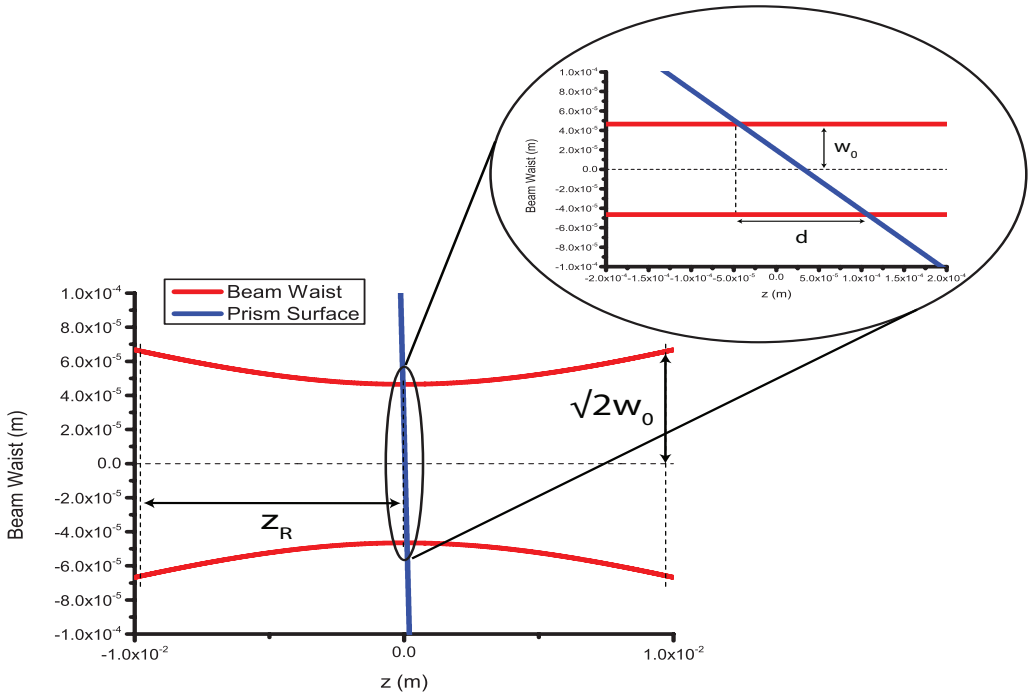

Figure 3.6: Gaussian beam analysis for the Dove prism. The beam is being focused on the upper surface of the prism. The distance between the beam extremes at the focal point is found to be $d = 155$ μm and the Rayleigh range $z_R = 9.7$ mm.

3.2.2 Two-dimensional Surface Trap

The optical binding experiment was extended to two dimensions using two orthogonal pairs of counter-propagating beams. The Dove prism is replaced by a plano-convex lens, (LA1951 by Thorlabs Inc. NJ, $d = 25.4$ mm and $R = 13.1$ mm). A perfect half-ball lens would be preferred for symmetry but due to the limited sizes (maximum diameter available 10 mm) and their high pricing one was not used. The mounting stage was also replaced by a new custom made stage, designed to incorporate the lens and allow two orthogonal pairs of counter-propagating beams to be incident on the curved surface. The laser beam is split to two beams by a 50:50 beam splitter. The second beam is then guided through a configuration similar to that described in the previous chapter (Figure 3.7). The half-wave plates control the polarisations of the two pairs and can be either parallel or orthogonal to each other. The short focal length lenses that are used to focus the four beams at the surface of the lens and are tilted so that the beam passes through them perpendicularly to reduce aberrations (i.e. the beam propagates nearly along the radius of the sphere

from which the lens is cut).

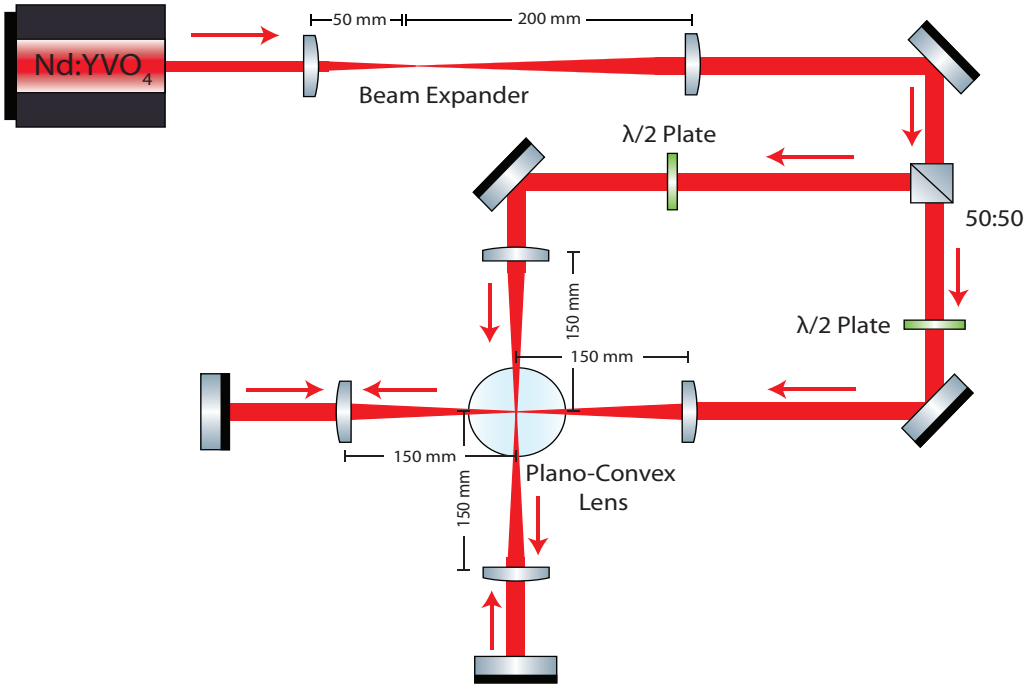

Figure 3.7: Experimental set-up used for the optical binding experiment extended in two-dimensions.

Calculations similar to the previous section were made to find the elevation angle. Since the substrate used is not a perfect hemisphere the incident beam is not along the radius. Figure 3.8 shows the deviation angle θ_d on the incident beam from the radius of the sphere from which the aspheric lens is taken. The deviation angle ($\theta_d = 2°$) is small compared to the elevation angle ($\theta_{asph.} = 27°$) thus the aberrations that are introduced do not significantly affect the quality of the focused beam. (i.e. the beam propagates nearly along the radius of the sphere from which the lens is cut).

Gaussian beam analysis was again used to confirm that the incident beam can be approximated by a plane wave. This time the analysis was made for the curved surface of the N-BK7 lens. The distance d along the z-axis between the two extremes of the beam at the focal point and the Rayleigh length are smaller than calculated in the previous section since the curved surface of the lens introduces further focusing of the beam. (Figure 3.9).

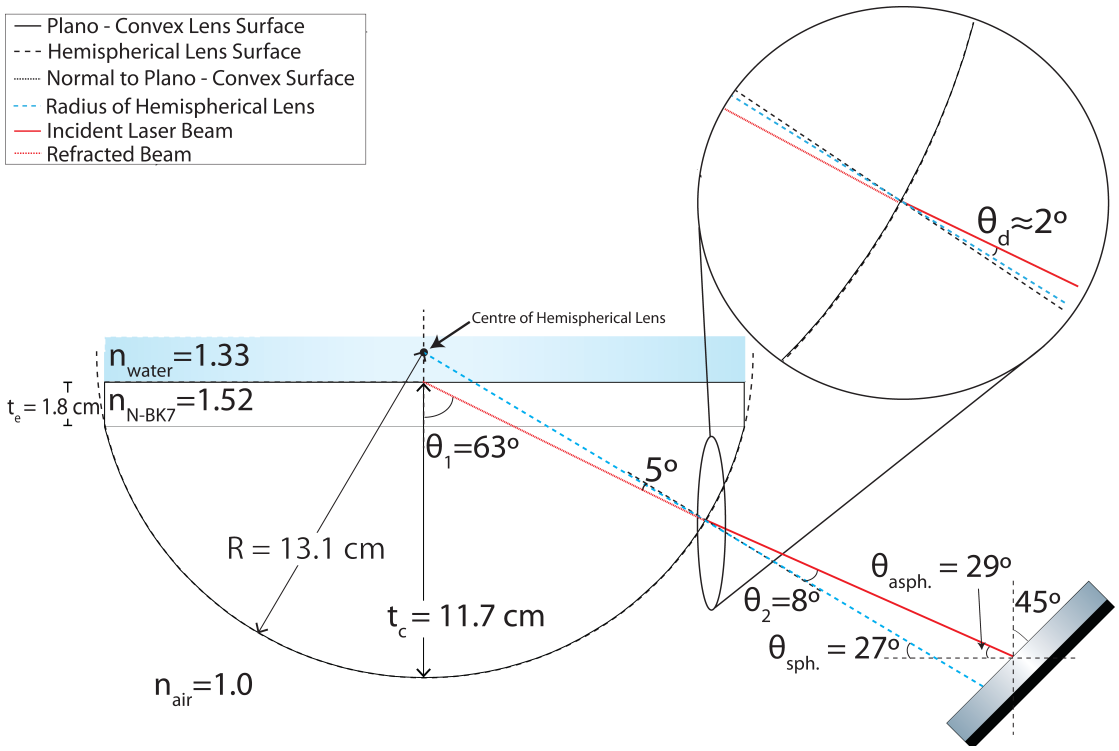

Figure 3.8: Elevation angle determination for the 2D binding set-up. Ray-tracing and Snell's Law were used to calculate the elevation angle for the incident beam in order to achieve slightly above critical angle incidence. The elevation angle from the horizontal is $\theta_{asp.} = 27°$. Since the lens used is not hemispherical the deviation of the incident beam from the radius of the sphere from which the lens is taken is calculated $\theta_d = 2°$.

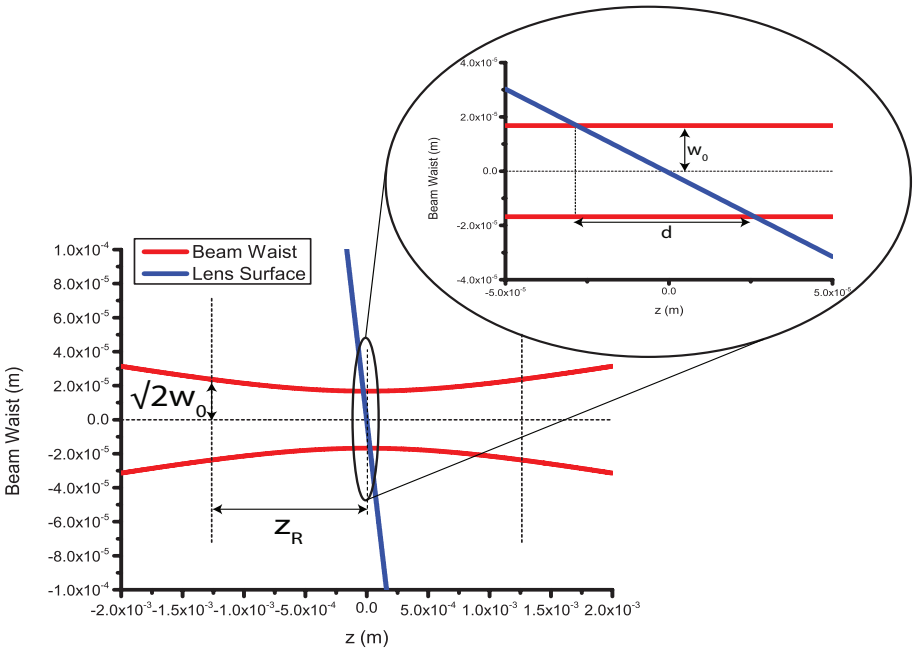

Figure 3.9: Gaussian beam analysis for a hemispherical lens. The beam is being focused on the upper surface of the lens. The distance along the z-axis between the beam extremes at the focal point is found to be $d = 54$ μm and the Rayleigh range $z_R = 1.3$ mm.

3.3 Particle Tracking

We use video microscopy to observe the dynamics of the optically bound particles. Particle tracking software (Particle Tracking Code for Matlab by Blair and Dufresne, Georgetown University, Physics Department [48]) is used to follow the trajectory of particles in the optically bound states for a number of frames depending on the video length and for a frame rate up to 300 fps.

The video is first split into individual frame images. Before tracking occurs the colours of each image are adjusted, if needed, so the particles are bright compared to the background. Each image is then spatially filtered by a spatial bandpass filter which smooths the image and subtracts the background. There are two parameters used for this filter: the length scale of noise and the size of the particles both in pixels. The filter first creates a smoothed image by convolving with a Gaussian.The second creates another smoothed image by convolving the original with a step function this time. Finally the second image is subtracted from the first and a sharpened image is produced.

The particles are then identified in each frame by locating the local maxima in the image. The brightness threshold can be predetermined and pixels with values above the threshold are identified. Another parameter for this step is again the size of the particles. If multiple peaks are found within the diameter of the particle then code selects the brightest one. The centroid of these selected pixels is then calculated within a particle radius and the location of the sphere centre is estimated within sub-pixel accuracy (Figure 3.10).

There are a few parameters here one should consider. The first one is the maximum distance that a particle can move between subsequent frames and therefore each particle is considered to be the same. Another one is the number of frames a particle can 'disappear' for and still be tracked and finally the minimum number of tracks (number of tracks shorter than this are rejected). A flowchart summarising the tracking process is shown in Figure 3.11.

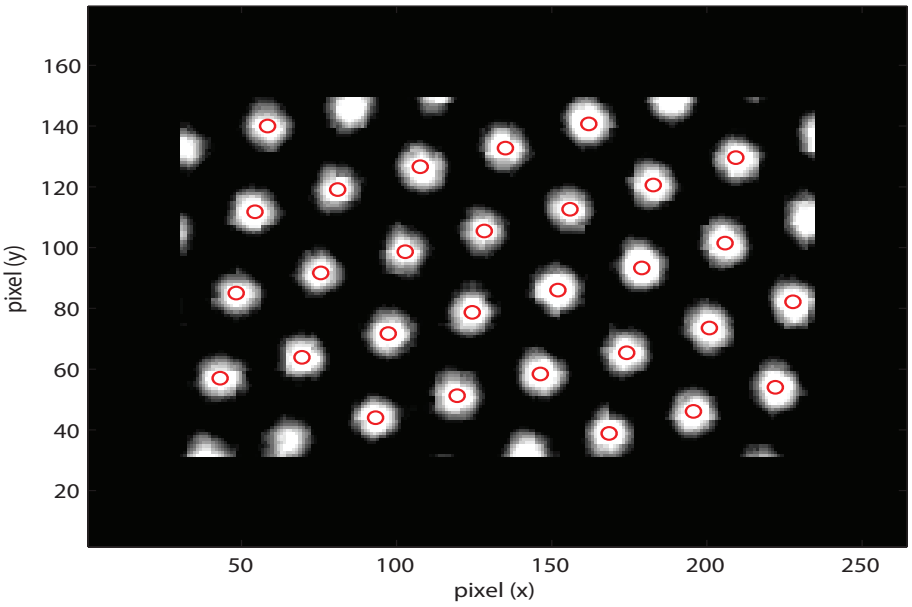

Figure 3.10: Particle Tracking: The centre of each particle is located in each frame.

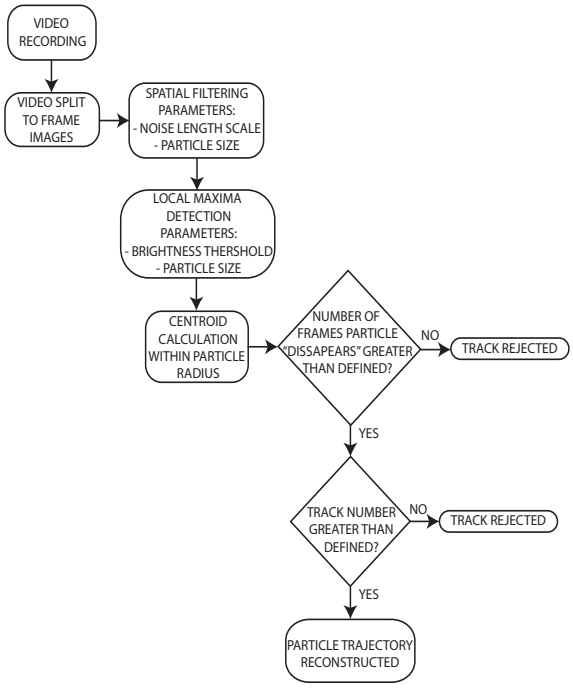

Figure 3.11: Flowchart of the particle tracking process.

The co-ordinates of the centroid of each particle are located in each frame and the particle trajectory can be therefore reconstructed (Figure 3.12). Even though this technique can be advantageous for tracking multiple particles, it is limited by the camera frame rate. Fast cameras can be used to overcome this limitation but they are very expensive.

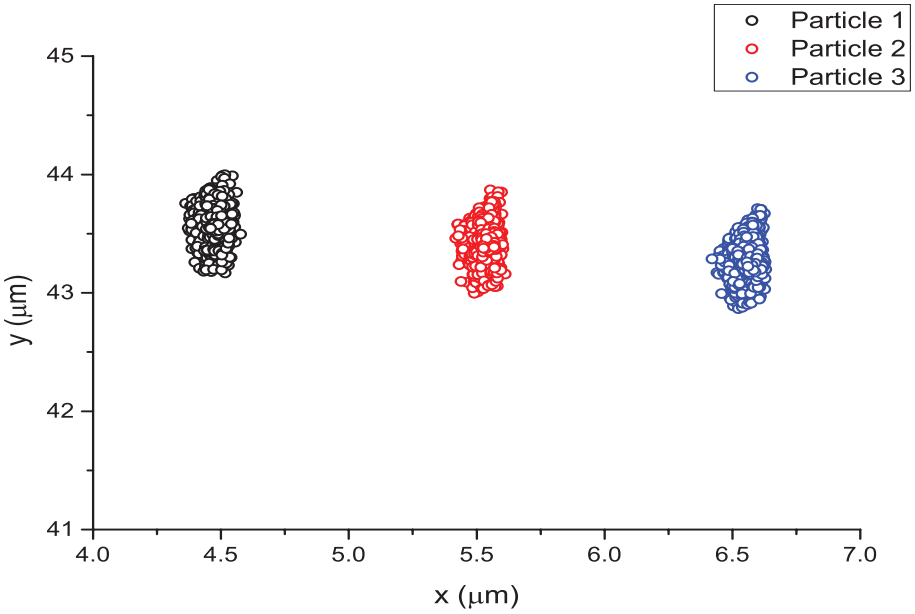

Figure 3.12: Particle trajectory reconstructed for 1 μm silica particles in one-dimensional bound chain. Particles were tracked over 1770 frames at 100 frames per second.

3.4 Outlook

The design and construction of an optical binding experiment of micro-particles using evanescent waves has been described in this chapter. The set-up constructed was designed such that can facilitate a number of laser beam configurations. Although the system was suitable for the experiments presented in this thesis, further work may be required for its optimisation. A Faraday isolator could be used for example to avoid any interference with the retro-reflected beams especially for the case of the two-dimensional trap configuration.

The set-up can be additionally extended to incorporate an optical tweezers set-up to provide quantitative measurements of the binding force by tracking utilizing a scattering detection technique. This technique uses a quadrant

photo-diode (QPD) to collect the scattered laser light forward-scattered or backward-scattered) of the surface of a trapped particle directly and provide particularly higher temporal resolution [49, 50, 51, 52]. A weak optical tweezers confines a single particle on top of the prism-water interface. The particle feels the presence of the evanescent field and moves by a measurable distance L_x from equilibrium. The force acting on the trapped particle can be then derived from the spring constant of the optical tweezers and compared to the results obtained in Chapter 2.4.

The apparatus described in this chapter is central to the experiments presented in the rest of this thesis and to the confirmation of the theoretical results presented in the previous chapter.

Chapter 4

Evanescent field surface trap: Results

4.1 Introduction

Following the description of the experimental apparatus used to conduct evanescent wave manipulation of micro-particles, we present the experimental results obtained. Particle tracking software was used to follow the trajectory of particles in the optically bound structures, the co-ordinates of the centroid of each particle are located in each frame and the particle trajectory reconstructed (Section 3.3). The reconstructed trajectories provide information for the particles in both one- and two-dimensional bound structures, namely the particle-to-particle separation, the binding spring constant and the lattice characteristics for the two-dimensional arrays.

4.2 Optical Binding Beam Configuration

First, we calculate the penetration depth Λ of the evanescent field. The penetration depth needs to be of the order of the particle size placed on the surface of the substrate so the evanescent field interacts with a significant fraction of the particle volume. Equation 2.44 gives the distance from the interface that the electric field falls at $1/e$ of the amplitude at the interface. For the laser wavelength used in the experiments ($\lambda = 1.064$ μm) and the glass-water interface, Λ is found to be 0.83 μm for an incidence angle of 63°.

In the one-dimensional surface trap the fringes formed (Figure 4.1a) by the two-counter propagating beams with parallel polarisations are spaced by a distance given by the following equation:

$$D = \frac{\lambda/n_{glass}}{2\sin(\theta_{inc})} \tag{4.1}$$

For the same parameters, as before, the fringe spacing D is 0.4 μm. The field scattered by the particles modifies the background interference pattern, which therefore dictates the optical binding geometry as discussed in Section 2.3.2.

For the case of the two-dimensional trap where two orthogonal pairs of counter-propagating beams cross at the top surface of the prism an interference pattern is formed. A representation of this pattern is shown in Figure 4.1b. In this case all four beams are incident on the interface at the same polar angle $\theta_{inc} = 63°$. The spacing between bright dots in the x- and y- directions is given by:

$$D = \frac{\lambda/n_{glass}}{\sin(\theta_{inc})} \tag{4.2}$$

The resulting spacing, D, for this configuration is 0.8 μm and the distance to nearest neighbours of the square lattice (i.e along the directions +/− 45 degrees in Figure 4.1b) is 0.6 μm.

The scattered light from the particles surface modulates the background fringe pattern, and thus dictates the lattice geometry of the two-dimensional structure [21].

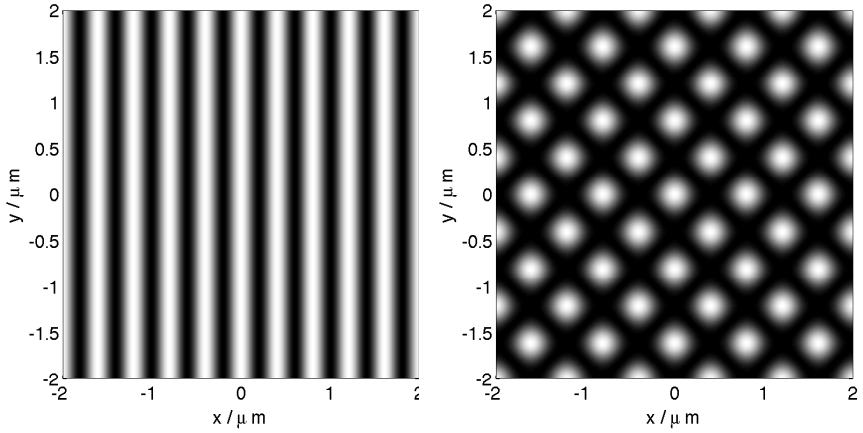

Figure 4.1: Representation of the interference pattern formed (a) by two counter-propagating beams. Both beams propagate along the x-axis and are polarised in the y-direction; (b) by the two orthogonal counter-propagating laser beam pairs ($\lambda = 1064$ nm). One pair propagates along the x-axis and the other along y-. Both pairs are polarised in the z-direction.

4.3 1D Binding

This section discusses the results obtained by the experimental configuration described in Section 3.2.1. The two counter-propagating beams generate an evanescent field at the prism-water interface, causing the dielectric particles to align them selves in well-defined one-dimensional chains (Figure 4.2). Qualitatively, this is due to the maximum intensity 'hot spots' that are created near the surface of the spheres as described in Chapter 2. These intensity 'hot spots' can be considered to act as an optical trap for a nearby particle, resulting in an optically mediated attractive force between the two particles. The experiments were conducted to characterise the optical binding interaction for spheres of different sizes including measurements of inter-particle separation and optical binding spring constant. This case has been approached theoretically in Section 2.3.2.

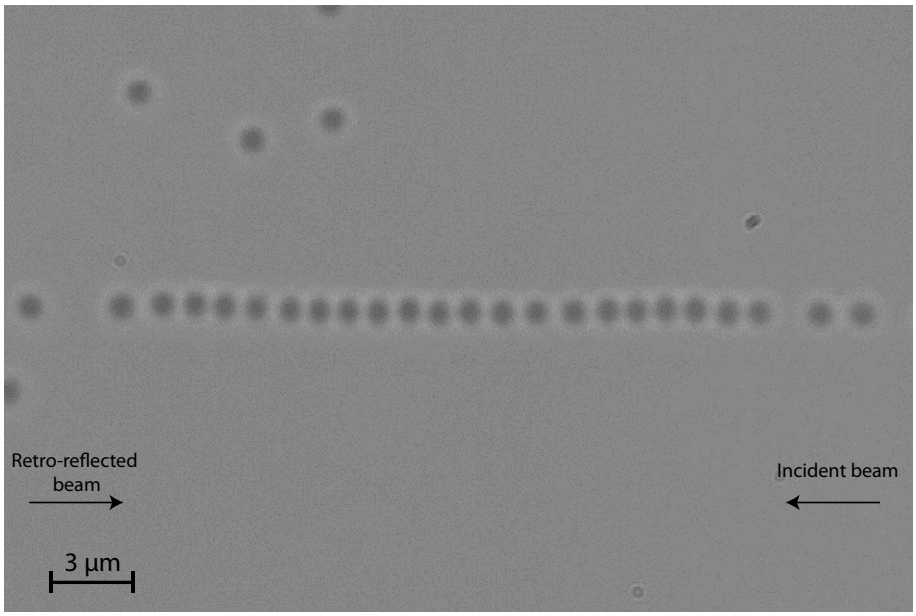

Figure 4.2: One-dimensional chain formation of 1 μm silica spheres in evanescent wave surface trap where two counter-propagating beams are used. Both beams here are s-polarised.

4.3.1 Particle Separation

The particle-to-particle separation in a 1D chain is derived by averaging the separations for a number of frames in a video. The frame images are passed through the image filters as explained in Section 3.3. The particles are now brighter compared to the background and the region of the bound chain is isolated for each frame. A MATLAB code finds the peaks in brightness in the image by fitting a Gaussian to the bright spots (particles) and marks them as the centre of the particles. The position of each particle is then plotted in space. Figure 4.3a shows an example of the particle positions in a single frame extracted from a video and Figure 4.3b shows the position distribution of the spheres recorded over 450 frames. The broader position distribution perpendicular to the chain axis shows that the particles are weakly confined in this direction (like a weak optical tweezers system) by the transverse intensity distribution of the binding beams. The distribution of particle fluctuations will be later quantitatively analysed to obtain the binding spring constant. The inter-particle separation can be then found by converting the distances between then particles from pixels to metres. This is done by using the camera's pixel size (3.6 μm $\times$ 3.6 μm) and the magnification of the objective lens used.

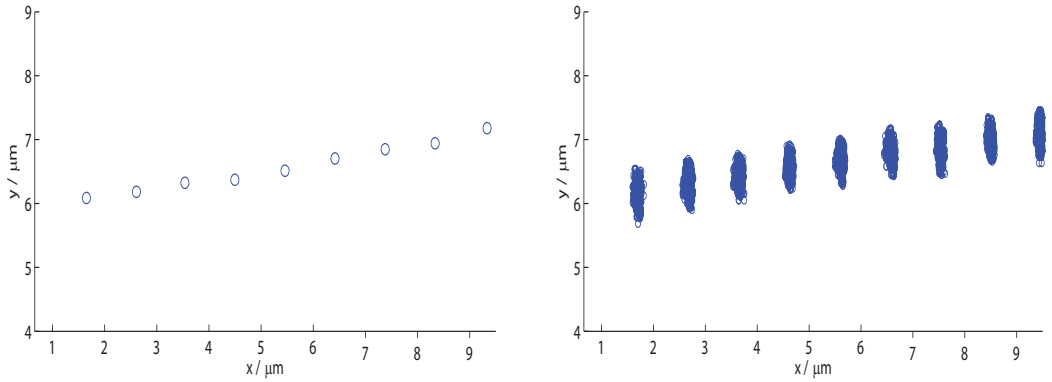

(a) **(b)**

Figure 4.3: Position of spheres in 1D chain as detected by image analysis (a) for a single frame; (b) for 450 frames.

Here we present particle separations as a function of laser power for silica spheres of various diameters (0.8 μm, 1.0 μm and 1.5 μm). The incident and retro-reflected beams are both s-polarised and therefore interference fringes are formed. The particle-to-particle separation in the bound structures are plotted as a function of the incident beam power.

It should be noted that even though the sample density was made the same for all cases, the number of particles in the bound structures was not controlled.

4.3.1.1 Parallel Polarisations

The behaviour of the particles in the presence of interference fringes was considered. Figure 4.4 shows the force (calculated using the same method described in Section 2.4.2) on a silica sphere immersed in water and positioned between a bright and dark fringe as function of the parameter $k\alpha$, where $k = 2\pi/\lambda_{water}$ and α is the particle radius. A single particle is attracted to a bright fringe when the force has a positive value [53, 43, 23]. Similarly a negative force indicates that the particle is attracted to an intensity minimum in the interference pattern. For all particle sizes considered here, the particles are attracted to bright fringes. This calculation is carried out for a single particle in counter-propagating beams to provide insight into the optical binding phenomenon. Detailed calculations accounting for multiple scattering between particles [23]

have demonstrated that the trapping behaviour is affected by the number of particles in the chain, and a particle that is attracted to dark fringes ('dark seeking') when isolated can become 'bright seeking' when in a longer optically bound chain.

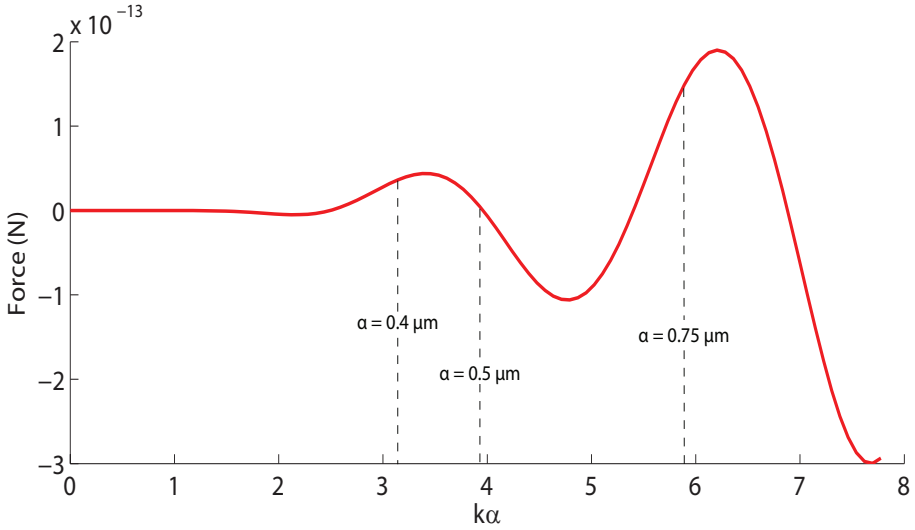

Figure 4.4: Force on silica sphere place between a bright and dark fringe as a function of $k\alpha$. Positive force indicates attraction to a bright fringe. The dotted lines denote the parameter $k\alpha$ for the particle sizes used in experiments.

Figure 4.5 presents the scattered field for each particle size used in experiments, in counter propagating beams with parallel polarisations. The fields here were calculated using Mie theory as described in Chapter 2. It can be seen that the scattered light modulates the background interference fringes and therefore creating a preferred trapping (binding) location for nearby particles.

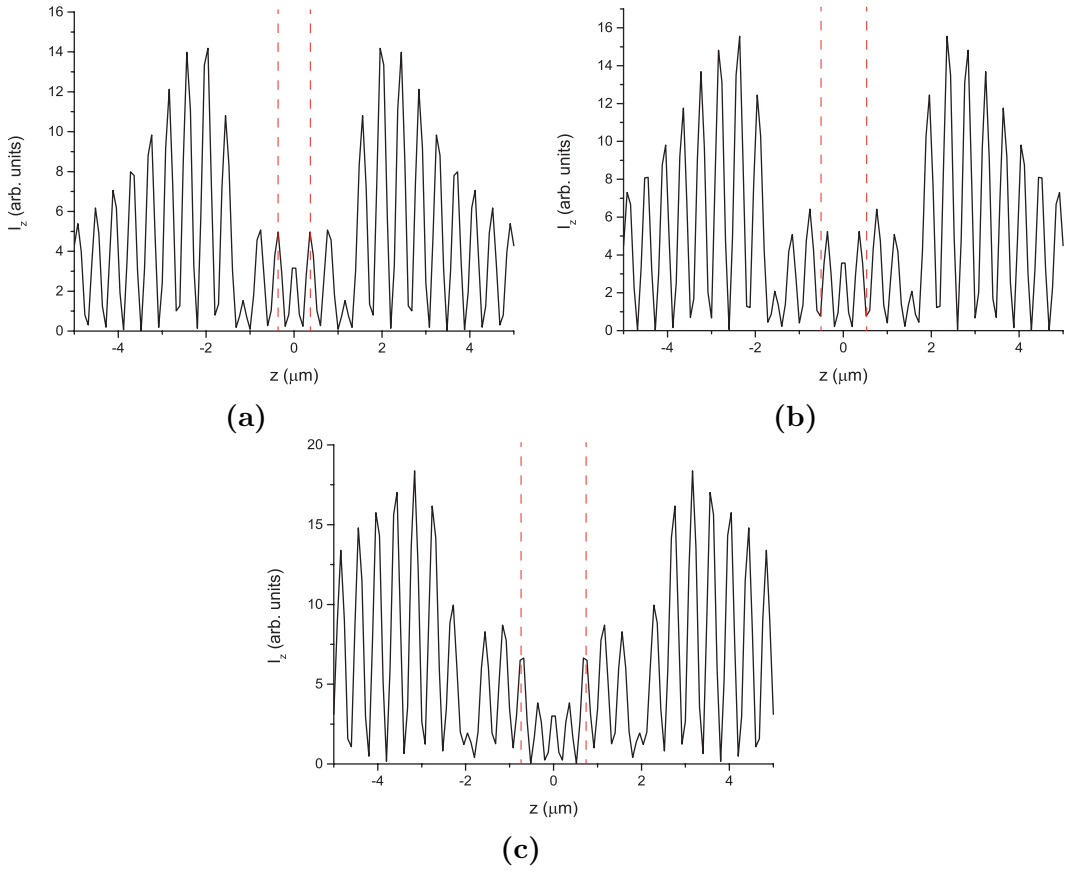

Figure 4.5: GLMT Calculation: Intensity measured along the propagation direction for silica spheres for diameters (a) 0.8 μm, (b) 1.0 μm and (c) 1.5 μm in counter propagating beams with parallel polarisations.

0.8 μm SiO_2 spheres

Figure 4.6 shows 0.8 μm diameter spheres bound by the evanescent field generated by the two counter-propagating beams both s-polarised. Following the procedure described at the beginning of this section, the inter-particle separation for different powers was obtained (Figure 4.7). It is apparent that the power does not alter the separation between particles. This is in agreement with the work of [15, 54]. For this case all separations were averaged and the mean inter-particle separation was found to be $d_m^{(0.8)} = (3.06 \pm 0.04)\mu$m. As seen in Figure 4.6, the spheres are not equally spaced. Hence the average particle-to-particle separation is found to be between seven and eight fringe spacings, $7D < d_m^{(0.8)} < 8D$. These fringes are not the brightest in the simple single sphere scattering model used so far, but it may be expected that multiple scattering modifies the intensities further. The potential wells formed 7-8

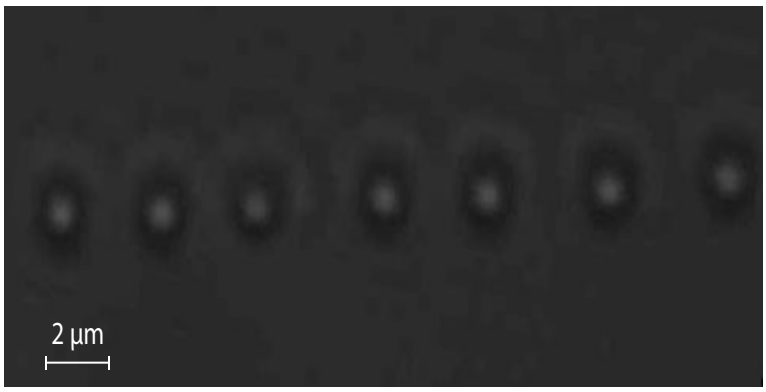

Figure 4.6: One-dimensional bound chain of 0.8 μm silica spheres.

fringe spacings away from one particle are apparently similar in depth (Figure 4.5a), so there is a low potential barrier between them and particles can 'hop' over the barrier from one to the other as a result of their Brownian motion.

While the number of particles in the bound structure increases the optical binding force increases, as the interaction between the particles becomes stronger [55, 56, 57]. Therefore the average inter-particle separation decreases. Here, the number of particles in the chain studied was not high enough (N $\sim$ 7) to further decrease the particle separation.

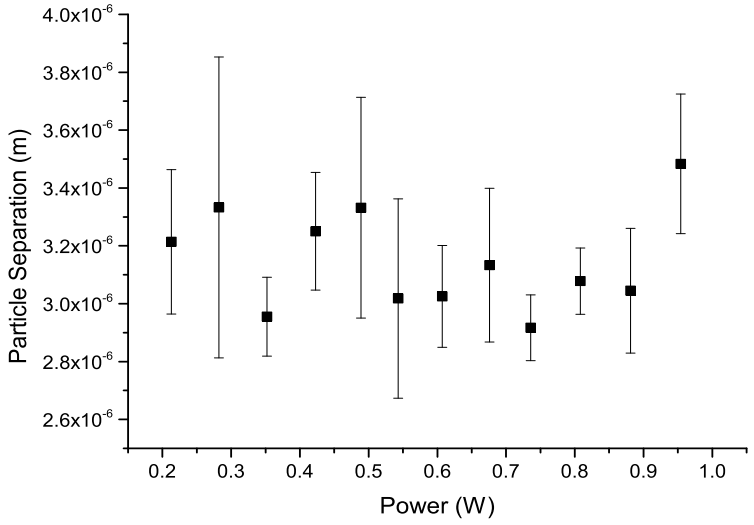

Figure 4.7: Inter-particle separation of 0.8 μm silica spheres in counter-propagating beams with parallel polarisations as a function of laser power. The averaged separation is $d_m^{(0.8)} = (3.06 \pm 0.04)\mu$m.

1.0 μm SiO_2 spheres

Similarly, the same procedure was repeated for 1.0 μm silica spheres optically bound in a one-dimensional 'chain-like' structure (Figure 4.8). The result here is the same in the sense that the varying laser power does not affect the particle separation (Figure 4.9). Contrary to the previous case, the parti-

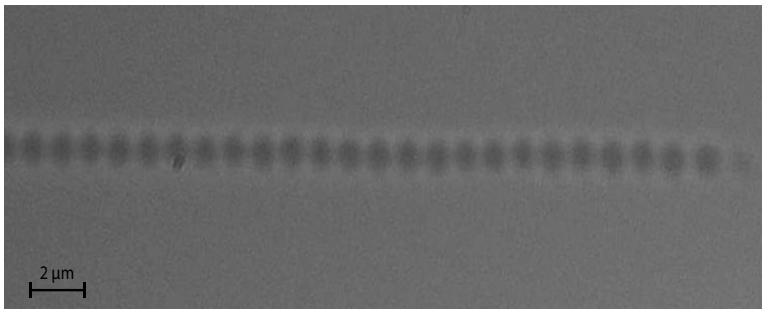

Figure 4.8: One-dimensional bound chain of 1.0 μm silica spheres.

cles are almost adjacent to each other. The mean inter-particle separation is $d_m^{(1.0)} = (1.05 \pm 0.01)\mu$m. The forces originating from the interference fringes compete with the forces arising from the scattered fields from the surface of the bound spheres. Since a diameter of 1.0 μm is close to the point where the optical landscape force vanishes (Figure 4.6) a small number of particles in the chain can overcome the optical landscape influence. The optical binding force dominates and the particles are attracted to the intensity maximum created near other particles as discussed in Chapter 2 and shown in Figure 4.5b. Furthermore, the number of spheres in the chain is high (N $\sim$ 16), leading to an overall inter-particle separation decrease.

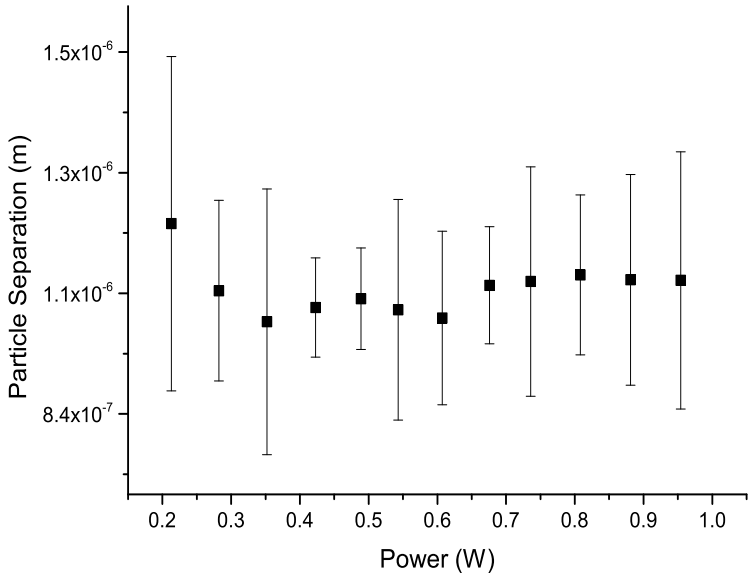

Figure 4.9: Inter-particle separation of 1.0 μm silica spheres in counter-propagating beams with parallel polarisations as a function of laser power. The averaged separation is $d_m^{(1.0)} = (1.05 \pm 0.01)\mu$m.

1.5 μm SiO_2 spheres

Last is the case of 1.5 μm silica spheres in a bound chain formed in two counter-propagating beams with parallel polarisations (Figure 4.10). The mean inter-

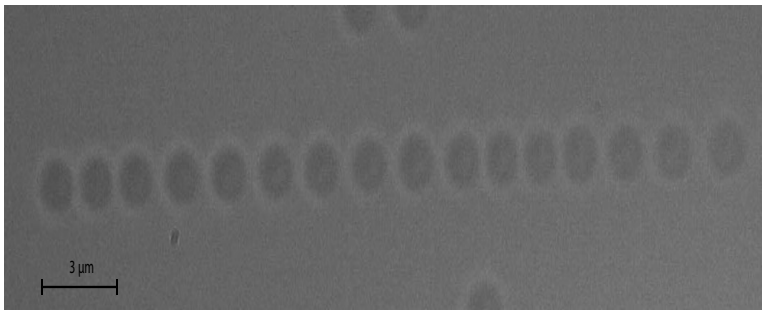

Figure 4.10: One-dimensional bound chain of 1.5 μm silica spheres.

particle separation was found to be $d_m^{(1.5)} = (1.86 \pm 0.02)\mu$m from Figure 4.11. The optical landscape force for this particle size is close to a maximum and therefore it is significant to the net force acting on the particles. These particle separations found, almost coincide with a maximum in intensity (Figure 4.5c). The particles are attracted to bright fringes, enhancing the scattered field from nearby particles. The fact that the scattered fields are greater than

in the case of the 0.8 μm spheres (Figure 4.5) where the forces arising from the fringes are also significant leads to smaller average particle separations. We can also observe that for this case the particle separation decreases with increasing power. As the intensity of the laser beam increases, more particles were attracted to the chain causing the average inter-particle separation to decrease as discussed before.

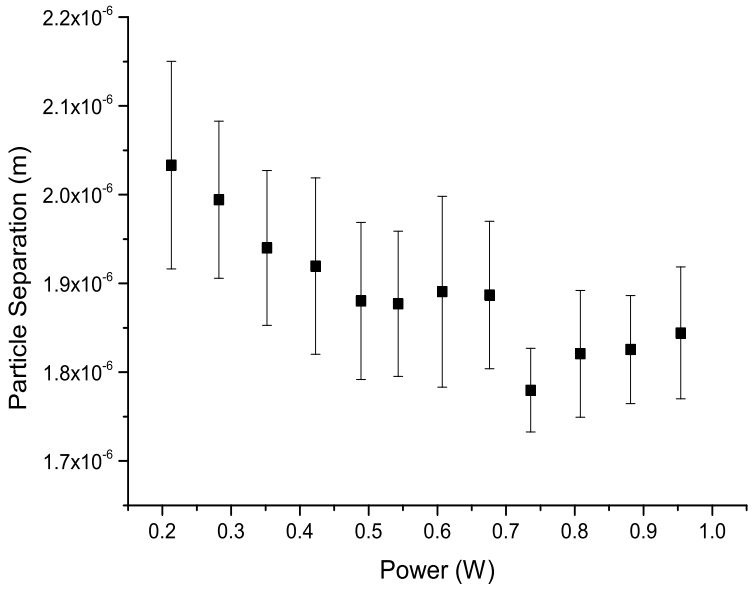

Figure 4.11: Inter-particle separation of 1.5 μm silica spheres in counter-propagating beams with parallel polarisations as a function of laser power. The averaged separation is $d_m^{(1.5)} = (1.86 \pm 0.02)\mu$m.

4.3.1.2 Orthogonal Polarisations

Next, we consider the configuration where the two counter-propagating beams have orthogonal polarisations. Namely, the incident beam is s-polarised and the retro-reflected is p-polarised. The separations of the bound particles are derived the same way as in the parallel polarisation configuration. Here the absence of an optical landscape formed by beam interference means that we only need to consider the forces that arise from the scattered light from the surface of the particles. Figure 4.12 shows the inter-particle separation for all particle sizes used for this part of the experiment.

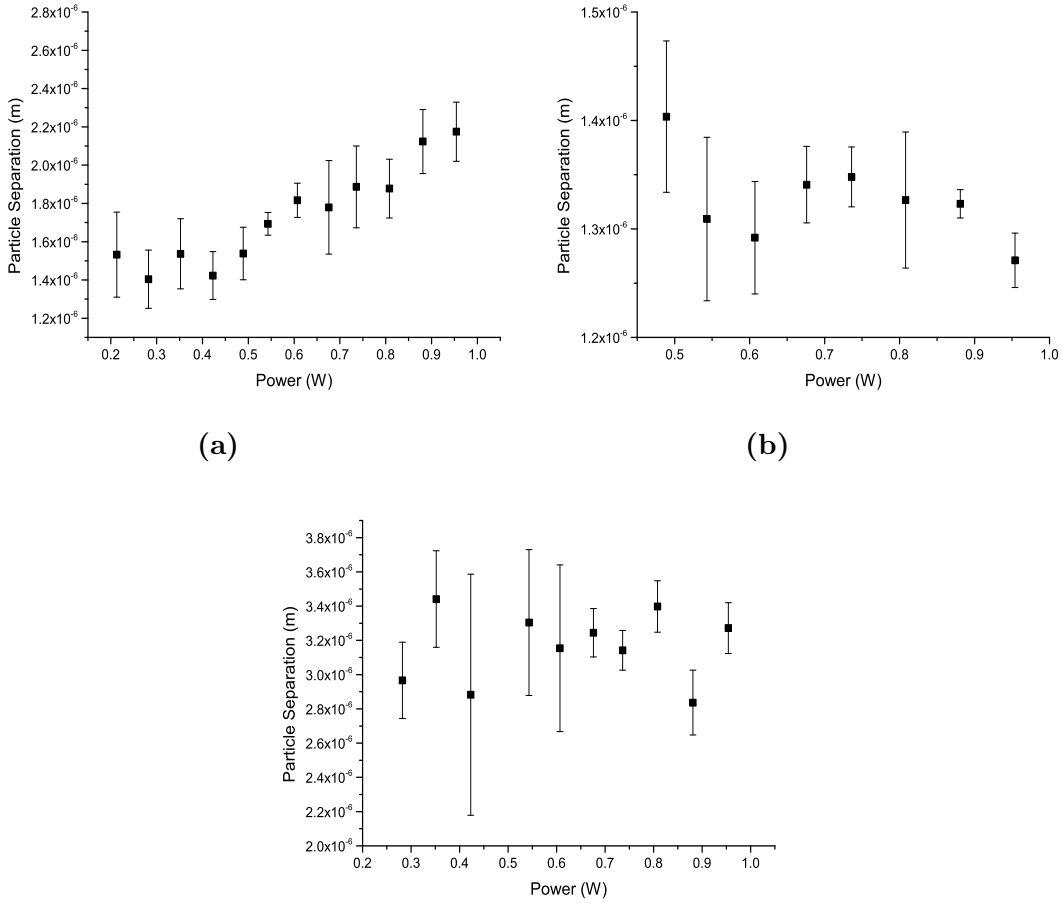

Figure 4.12: Inter-particle separation for 0.8 μm, 1.0 μm, 1.5 μm in counter-propagating beams with orthogonal polarisations. (a) 0.8 μm silica spheres, average separation $d_m^{(0.8)} = (1.72 \pm 0.06)\mu$m; (b) 1.0 μm silica spheres, average separation $d_m^{(1.0)} = (1.32 \pm 0.01)\mu$m; (c) 1.5 μm silica spheres, average separation $d_m^{(1.5)} = (3.20 \pm 0.05)\mu$m.

For the case of the 0.8 μm spheres we observe an increase in particle separation with increasing power. Due to their thermal energy, the particles were able to overcome the binding forces leading to different separations. Figure 4.13a shows an example at low power where the distance of a sphere from its two adjacent ones (left and right) differs i.e. $d_2 < d_1$. This resulted in smaller average separations. For higher powers the spheres were strongly trapped and spaced by larger equilibrium separations as shown in Figure 4.13b.

Mie scattering theory predicts an intensity maximum close to the surface of the sphere as shown in Figure 4.14. Based on these calculations, particles

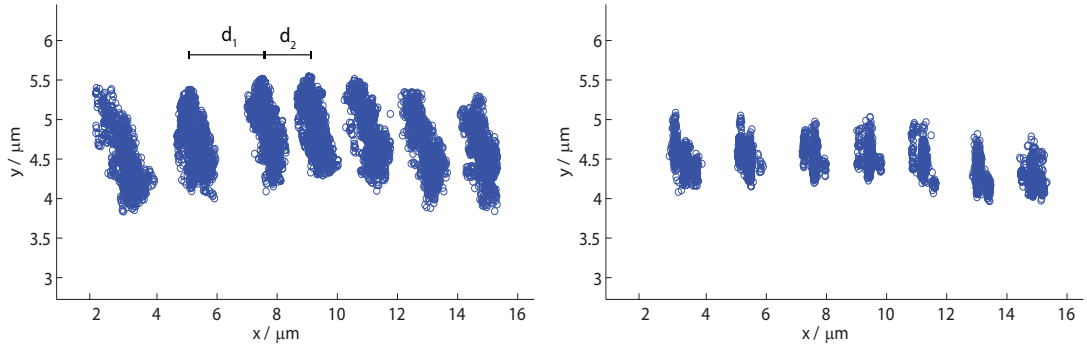

Figure 4.13: 0.8 μm bound particle trajectories in a chain structure (a) at low power (P = 0.213 W) where the distances of a sphere from its two adjacent ones differ; (b) at higher power (P = 0.954 W) where the spheres are strongly trapped and equally separated.

are expected to physically be in contact with each other as the intensity of the scattered fields increases with decreasing distance from the sphere surface. In all cases considered here the particles occupy equilibrium positions further away from these positions. Since the calculations are made for a single particle, they do not represent the results obtained here. The multiple scattering of the particles in the bound structure needs to be accounted. The forces arising from the interaction of the scattered fields and the incident beams change in sign with varying particle separation, denoting repulsive (negative sign) and attractive (positive sign) nature. Therefore, the particles occupy equilibrium positions in the chain where the net force of the scattered fields is zero [55, 58, 59].

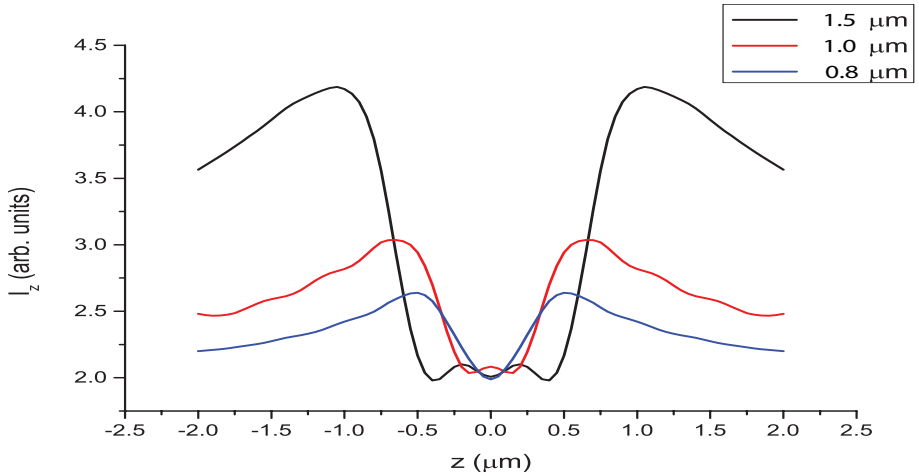

Figure 4.14: GMLT Calculation: Intensity in the propagation direction for silica spheres with sizes used in experiment in counter propagating beams with orthogonal polarisations.

4.3.2 Spring Constant

After the trajectories of the particles are reconstructed (Figure 4.3b), histograms of the Brownian motion of the particles are then derived in order to measure the extent of particle fluctuations in the direction of propagation (Figure 4.15). The change in the extent of the position fluctuations it is apparent with varying power.

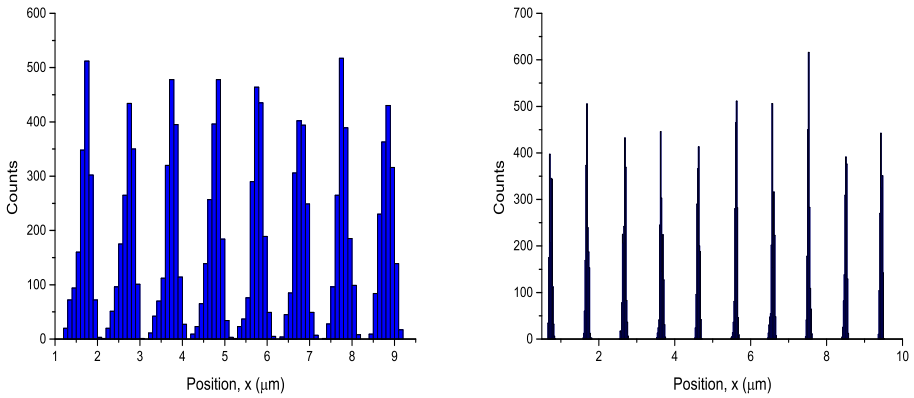

(a) **(b)**

Figure 4.15: Histograms of bound 1.0 μm particles in one-dimensional chain with both beams being s-polarised. (a) For low laser power, P = 0.213 W; (b) for high laser power, P = 0.954 W.

In order to avoid fluctuations in the motion of the particle due to the water being heated by the laser beam or due to periodic oscillations (Figure 4.16) of the bound structures [13, 60, 61, 62] we first plot the particle position in the

beam propagation direction in respect to time. From such plots we can then select data for which the the bound structures are more 'stable'.

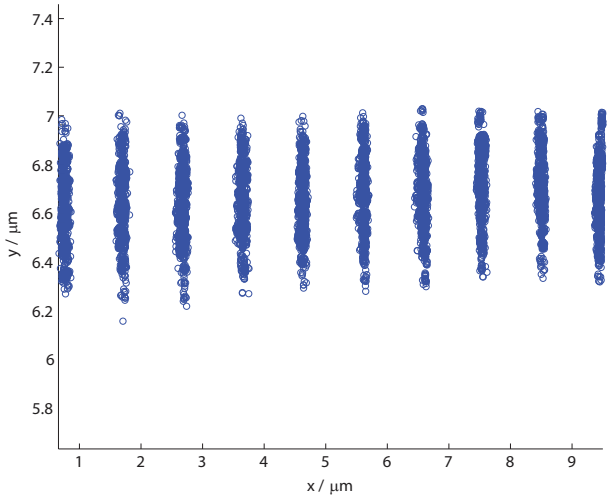

Figure 4.16: Oscillating optically bound chain of 1.0 μm for laser power P = 0.954 W. The oscillation in the direction orthogonal to propagation (y-) is apparent.

Figure 4.17 shows an example of the selection of such data. Another feature apparent in this figure is the discrete jumps between equilibrium positions A, B and C. The distance between these positions coincides with the fringe spacing, $AB = (0.43 \pm 0.04)\mu$m and $BC = (0.37 \pm 0.04)\mu$m indicating that the chain 'jumps' between fringes. This suggests that particles with large enough thermal energies overcome the binding energies and move to different equilibrium positions.

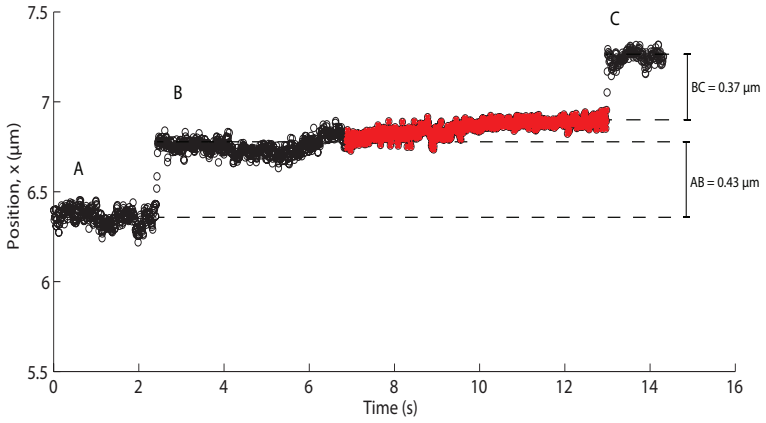

Figure 4.17: Selection of data for which the 1D bound structure is more stable.

Assuming that the particle experiences a harmonic potential due to the combination of the incident laser field and the scattered fields from the other

particles in the chain, we can calculate the spring constant of the particles in these structures.

$$\frac{1}{2}K_BT = \frac{1}{2}\kappa\langle x\rangle^2 \tag{4.3}$$

The $l.h.s$ of Equation 4.3 represents the mean energy of the oscillations of the particle in the system where K_B is the Boltzmann constant and T the temperature. The $r.h.s$ is the potential energy stored in a simple harmonic oscillator at position x and κ is the spring constant.

The spring constant can be obtained by fitting a Gaussian (Figure 4.18) to the histograms of the Brownian motion of individual particles. The Gaussian expression fitted to the histograms is of the following form:

$$f = A\mathrm{e}^{-\frac{\langle x\rangle^2}{2w^2}}, \tag{4.4}$$

where w is the width of the Gaussian fit. By combining Equations 4.3 and 4.4 we can assume that:

$$\kappa \to \frac{K_BT}{2w^2} \tag{4.5}$$

Substituting w from the fit into Equation 4.4, the spring constant is obtained.

In this section we present the spring constant of the optically bound 'chain-like' structures in the evanescent field of two counter-propagating beams as a function of laser power incident on the substrate. The data analysis was made for two polarisation schemes.

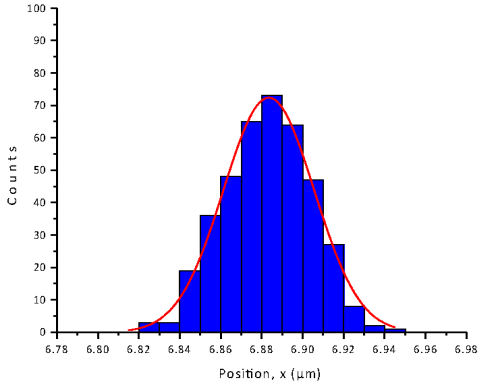

Figure 4.18: Position fluctuations of in the direction parallel to the chain about the equilibrium position of a single particle in the chain when optically bound using a single laser beam. Total number of counts is N = 407. The solid red line is a Gaussian fit to the histogram which gives a root-mean-square deviation from equilibrium.

4.3.2.1 Parallel Polarisations

The incident and the retro-reflected beams have parallel polarisations. Namely, both beams are s-polarised. Figure 4.19 shows the spring constant, κ, as a function of laser power for 0.8 μm, 1.0 μm and 1.5 μm silica particles.

We observe that the overall value of the spring constant increases with particle size. This is due to the fact that polarisability (and hence the trapping force) scales approximately with particle volume. It can be also seen that for all particle sizes the spring constant increases with power. This is expected as the optical forces restraining the particles in optical bound structures increase with intensity. Increasing the laser power the potential wells become deeper and therefore the well curvature is stronger leading to a larger spring constant.

4.3.2.2 Orthogonal Polarisations

Next, we consider the case where the two laser beam pairs have orthogonal polarisations (s- and p- polarisations). Figure 4.20 shows the spring constant as a function of laser power for this configuration. The results resemble those of the previous configuration in such a way that the spring constant grows with particle size and laser power.

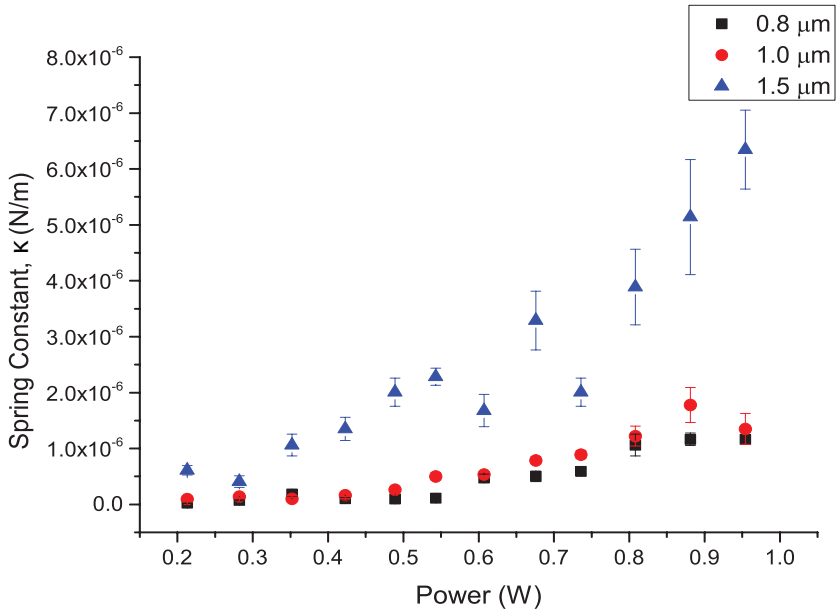

Figure 4.19: Spring constant vs Laser Power for 0.8 μm, 1.0 μm and 1.5 μm silica particles in one-dimensional bound chains formed in parallel polarised laser beams.

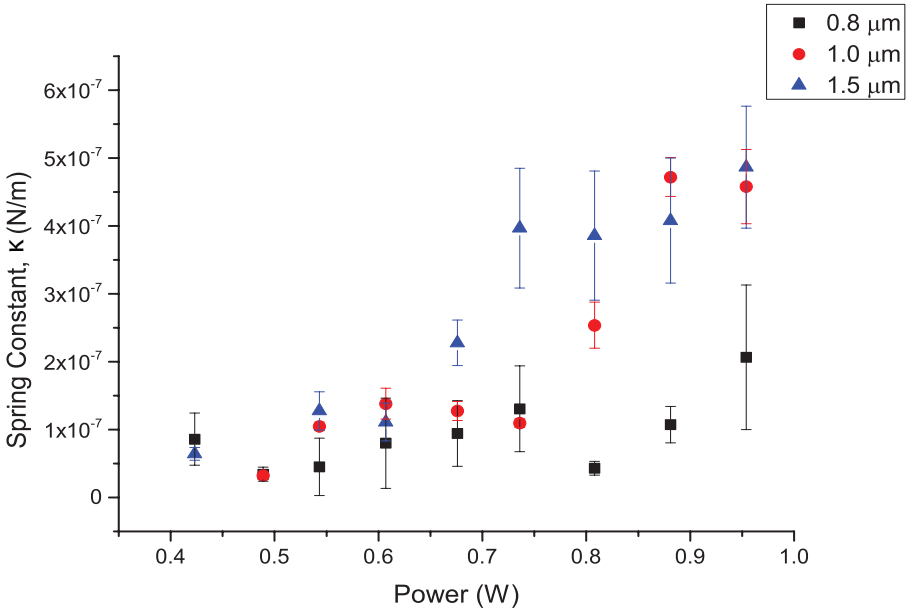

Figure 4.20: Spring constant vs Laser Power for 0.8 μm, 1.0 μm and 1.5 μm silica particles in one-dimensional bound chains formed in orthogonally polarised laser beams.

When comparing the values for the spring constant for each power and particle size we observe that for this configuration the value is lower than in the parallel polarisations configuration. This is due to the absence of the optical landscape forces which restrain the silica spheres even further. Figure 4.21 shows the difference between the magnitude of the forces, $\Delta F = F_{par} - F_{orth}$, acting on the particles for the different polarisation configurations as a function of laser power. These forces were derived from the calculated spring constant for each laser power setting. It is apparent that ΔF is comparable to the force arising from the optical landscape (Figure 4.4). The optical landscape force was found to be 1.45×10^{-13}N, 0.07×10^{-13}N and 0.36×10^{-13}N for 1.5 μm, 1.0 μm and 0.8 μm particle diameters respectively using GLMT.

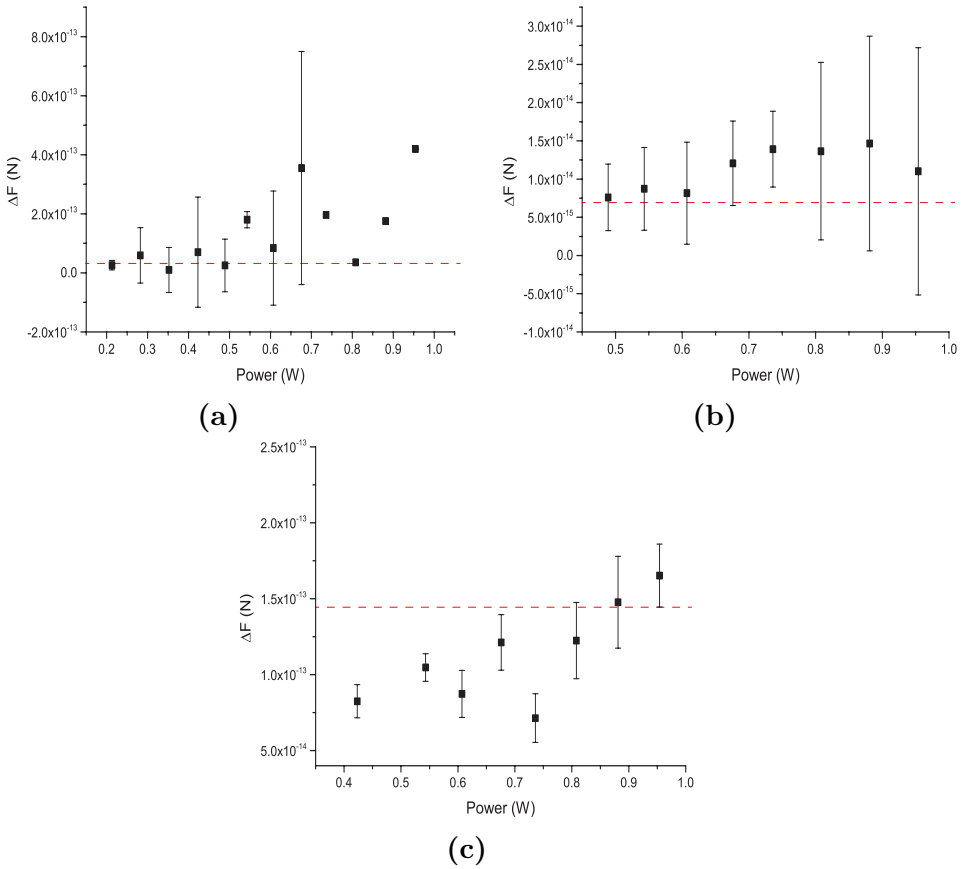

Figure 4.21: Difference between the force magnitudes for the parallel and orthogonal polarisation cases as a function of laser power. (a) 0.8 μm; (b) 1.0 μm; (c) 1.5 μm silica spheres. The red dashed lines indicate the force arising from the optical landscape as in Figure 4.4

It can be seen in Figure 4.21c that ΔF values mainly lie below the optical landscape force line. This was caused due to the fact that for the orthogonally

polarised beam configuration more particles were present in the chain. This lead to an increase of the optical binding force [55, 56, 57] and therefore smaller ΔF values for this case.

4.4 2D binding

In Chapter 3 we have described the extension of the binding set-up to two-dimensions using two orthogonally propagating pairs of counter-propagating beams. The results obtained using this trapping geometry are presented in this section. Similarly to the one-dimensional surface trap, we study two different polarisation configurations. The first is the case where the two pairs are parallel polarised and for the second are orthogonally polarised. In both cases the bound spheres form two-dimensional arrays.

4.4.1 Lattice Geometry

Next, we study the lattice geometry of the two-dimensional arrays of 1.0 μm silica particles formed for the different relative polarisations of the two beam pairs. For the first case both pairs (incident and retro-reflected beams) have s-polarisations and for the second case one pair is s-polarised and the other p-polarised.

There are two kinds of lattices we shall consider here. The lattice constant is the distance between the unit cells in the lattice. Two-dimensional lattices are defined by two lattice constants. Figure 4.22 shows the representation of square and hexagonal lattices. For a square lattice $a = c$ and for a hexagonal lattice $c = \sqrt{3}a$.

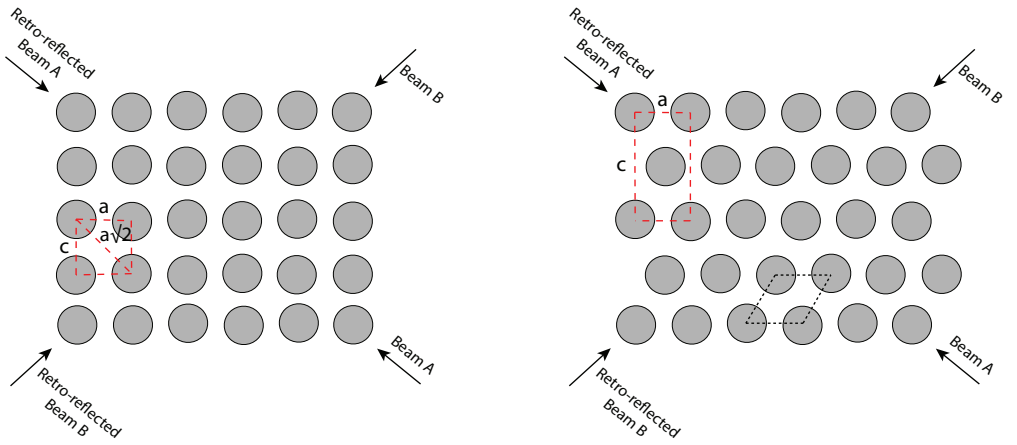

Figure 4.22: (a) Square lattice representation. The distance between two subsequent particles in both x- and y- directions is equal. (b) Hexagonal or equilateral lattice representation. The distance between two subsequent particles in both y- direction is $\sqrt{3}$ times greater than that in the x- direction. The black dashed lines here define the unit cell for this lattice.

We also construct Voronoi diagrams for the lattice geometries observed in experiments. A Voronoi diagram is used to divide space to different regions. A Voronoi cell encloses a site and every point in this region is closer to the this site than to any other. In our case the sites are the bound particle centres as identified by the particle tracking software. A Voronoi tessellation gives rise regular square cells for a square lattice and regular hexagons for a hexagonal lattice [63]. The averaged area of this cell was found for these cases.

Additionally we calculate the bond orientational order parameter for each case studied here. The bond orientational order parameter quantifies the local order in the lattice [64]. For a square lattice where each particle has 4 nearest neighbours the bond orientational order parameter for particle j is:

$$\psi_4 = |\frac{1}{z_j}\sum_{m=1}^{z_j}\exp(4\mathrm{i}\theta_{\mathrm{m}}^{\mathrm{j}})| \tag{4.6}$$

where z_j is the co-ordination number (number of nearest neighbours), and θ_m^j is the angle made by the line from particle j to its m-th neighbour and the x-axis. Perfect square ordering gives $\psi_4 = 1$. For the case of a hexagonal lattice

where a particle j has six nearest neighbours, the above equation becomes:

$$\psi_6 = |\frac{1}{z_j}\sum_{m=1}^{z_j}\exp(6\mathrm{i}\theta_{\mathrm{m}}^{\mathrm{j}})| \tag{4.7}$$

and for a perfect hexagonal lattice $\psi_6 = 1$. Similar code as described before tracks the centre of each particle in each video frame. Next, it identifies the z_j nearest neighbours for each particle, measures angle θ and calculates ψ. Finally, it averages over the whole area of the bound array and we obtain a measure of ordering.

4.4.1.1 Square Lattice

A square lattice is observed when the two beam pairs are of the same polarisation. Figure 4.23 shows 1 μm silica spheres organised into a a square lattice (N $\approx$ 200 particles).

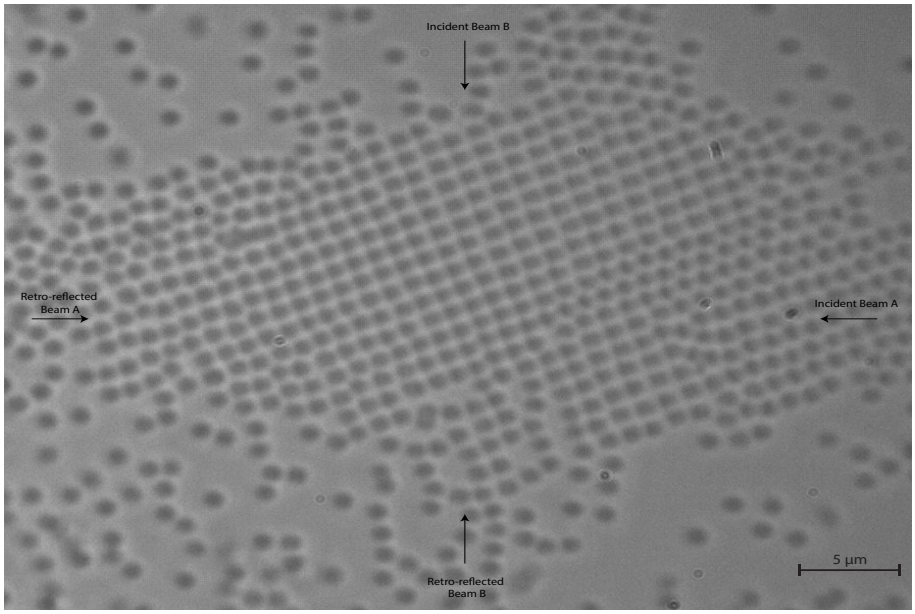

Figure 4.23: Square lattice formed by 1 μm silica spheres at the crossing point of two orthogonal counter-propagating beam pairs.

Video frames are analysed to retrieve the lattice constant of the structure. Particle centres contained in a selected region are detected (Figure 4.24a) in the same manner described in Section 4.3.1. Next, the code calculates the distances between the particle centres and finally uses them to construct a histogram as seen in Figure 4.24b. The first peak in this plot denotes the

lattice constant a which in this case was found to be 1.19 μm. The second peak in this case is the diagonal of a unit cell and its labelled as γa. For a square lattice $\gamma = \sqrt{2}$. From the data analysed γ was found to be 1.44 with an estimated error due to resolution of $\pm$ 0.04 which indicates a square lattice. Every third peak labelled as $2a$ is the distance from the closest particle of the adjacent unit cell.

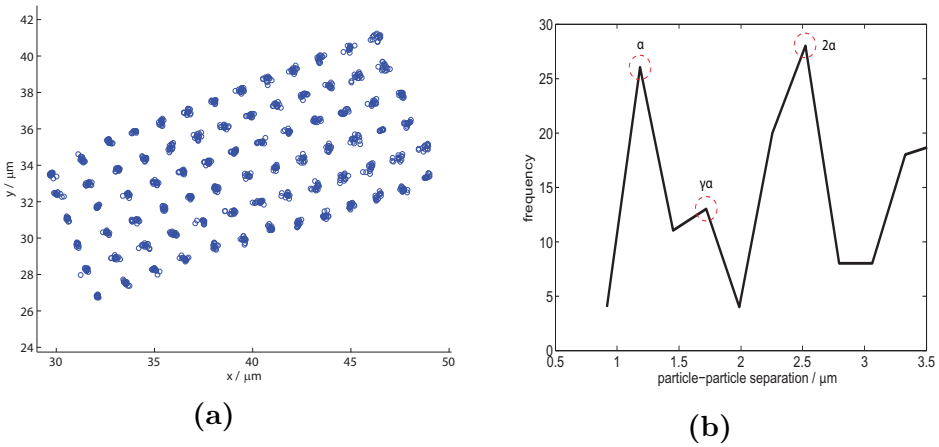

Figure 4.24: Square Lattice Characterisation: (a) Particle centre trace; (b) Particle distance distribution, in square lattice.

Figure 4.25a shows the position of the spheres and the field distribution (shown in the background) for this case. The symmetry of the arrangement of the spheres matches that of the initial underlying interference pattern but they are not all located exactly on top of a bright fringe due to the multiple scattering, and hence optical binding effects. The background field is modified by the multiple scattering so the equilibrium separations of the spheres are not equal to the separation between bright fringes, even though the interference pattern sets the symmetry of the optically bound structure. This is especially significant for the 1 μm diameter spheres where the binding forces may be strong compared to the background landscape forces. Figure 4.25b shows the same particles considered in Figure 4.25a in the bound structure. Furthermore, we used GLMT to calculate the fields for a single sphere in a four beam interference pattern (Figure 4.25c). It can be seen that the interference fringes are modified by the scattered fields.

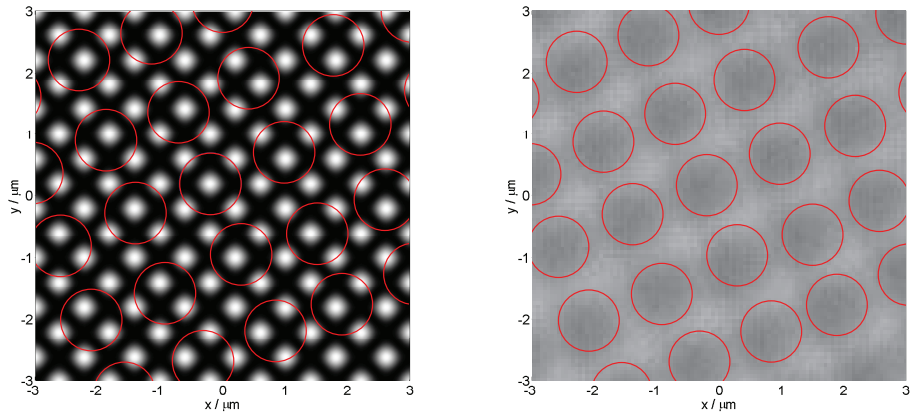

(a) **(b)**

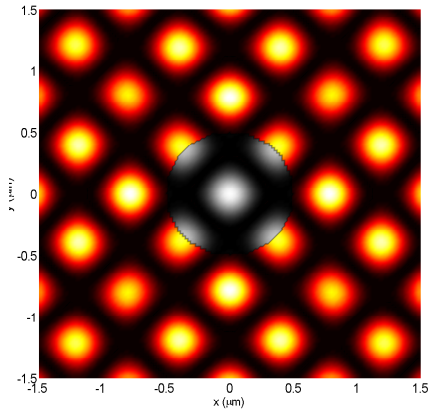

(c)

Figure 4.25: (a) Positions of 1 μm silica spheres and the interference landscape created by two orthogonal pair of beams with parallel polarisations at $\lambda = 1064$ nm. (b) Image of actual particles considered in part (a). The background interference pattern is significantly modified by scattering by the particles (not shown in part (a) and (b)) which determines their equilibrium positions. (c) GLMT calculation for a single sphere in a four beam interference pattern showing evidence of the modification of the interference pattern.

The observations are qualitatively supported by the work presented by Grzegorczyk *et al* where they computed the scattered field from an arbitrary number of infinite dielectric cylinders [29]. They treated cylinders rather than spheres and considered scattering in two dimensions only to reduce the complexity of the multiple scattering problem. They have similarly shown that the cylinders do not always settle on high intensity regions i.e. the final position of the particles is not always the one predicted for a single particle. They have considered the modification of the incident-field pattern by the scattered field by all particles and their interactions predict the location of the traps. The calculations were made by extending the Mie scattering theory to cylindrical particles and by using the Foldy-Lax multiple scattering equations. Figure 4.26 [29] shows the positions of 20 dielectric cylinders and the field distribution for various cases: (a) an example of initial positions of the cylinders, (b) the final positions of the cylinders with the incident field shown, (c) same as (b) but with the total field shown and (d) final positions of the cylinders corresponding to different initial positions. In (b) particles occupy separate traps whereas in (d) particles are located in regions where the total field is such that the neighbouring traps exert no force on nearby particles. Furthermore, the background interference pattern controls the symmetry of the bound structure, even though the particles do not lie on the maxima, and this is also what we have observed.

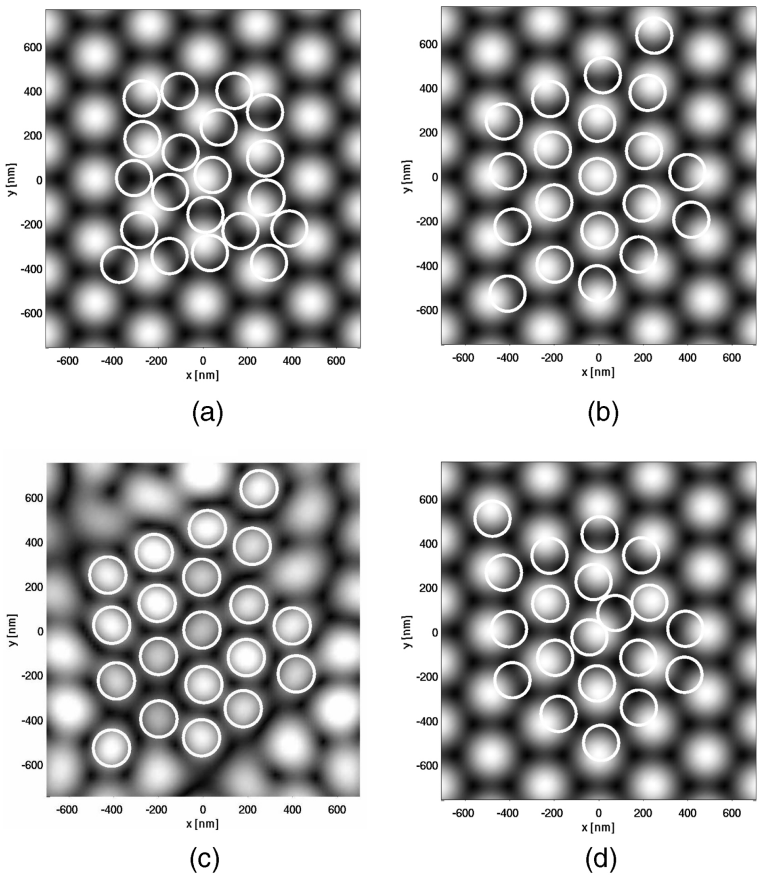

Figure 4.26: Positions of 20 dielectric cylinders and field distributions (shown in the background) for various cases: (a) random initial position in a three-plane-wave interference pattern (incident field shown); (b) organized final position due to trapping and binding forces (incident field shown); (c) same as case (b) but with the total field shown; (d) organized final position corresponding to another set of initial positions different from that in case (a). In all cases, the parameters are λ=546 nm and cylinder radius 0.15λ. The background patterns show the absolute value of the electric field (either incident or total field) on a scale from 0 (black) to 3 V/m (white) [29].

Figure 4.27 shows the Voronoi diagram for this case[1]. The appearance of the Voronoi cells provides further qualitative evidence of the influence of the underlying square lattice interference pattern on the ordering of particles. The averaged area of these cells was found to be $(1.4 \pm 0.3)\mu\text{m}^2$. The area of the Voronoi cell here is in agreement with the cell area obtained by using the measured nearest particle separations which is equal to $(1.4 \pm 0.1)\mu\text{m}^2$.

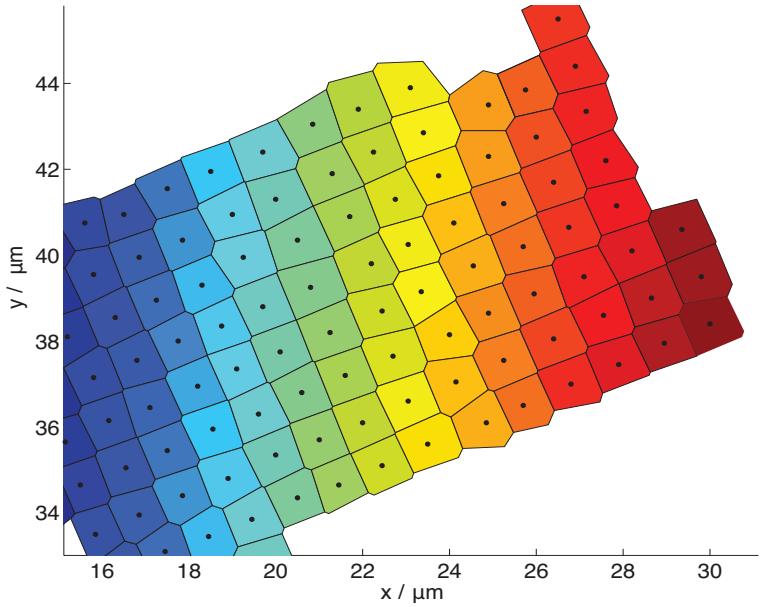

Figure 4.27: Voronoi diagram for the square lattice of 1.0 μm silica particles.

Finally, we calculated the bond orientational order parameter ψ_4, as a function of time for the square lattice using Equation 4.6. Figure 4.28 shows ψ_4 for two videos captured: first when the laser source was turned off (black curve) and second with the laser source turned on (red curve). It can be seen that when laser is off ψ_4 varies with time and has values well below 1 since the particles are free in water causing angle θ_m^j to vary with time. When the laser source is on, the particles are bound in a square lattice and ψ_4 obtains values close to one (optical binding in this configuration produces a stable, well-ordered square lattice).

[1]The edges of the diagram have been removed since an infinite area cell is constructed due to the absence of nearby particles.

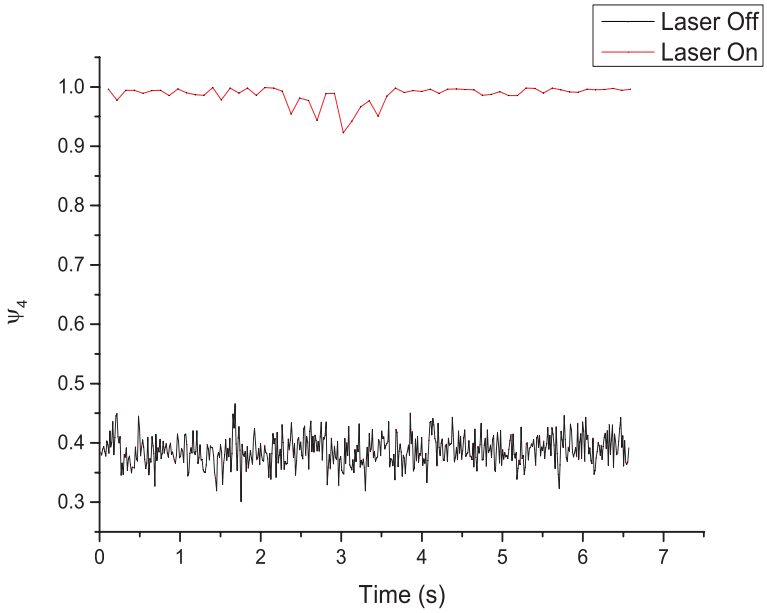

Figure 4.28: Bond orientational order parameter as a function of time for a square lattice. The black and red curves are for the case when the laser source is switched off and on respectively.

4.4.1.2 Hexagonal Lattice

When the two counter-propagating beam pairs are of orthogonal polarisations, we observe a hexagonal lattice as shown in Figure 4.29. The distances between

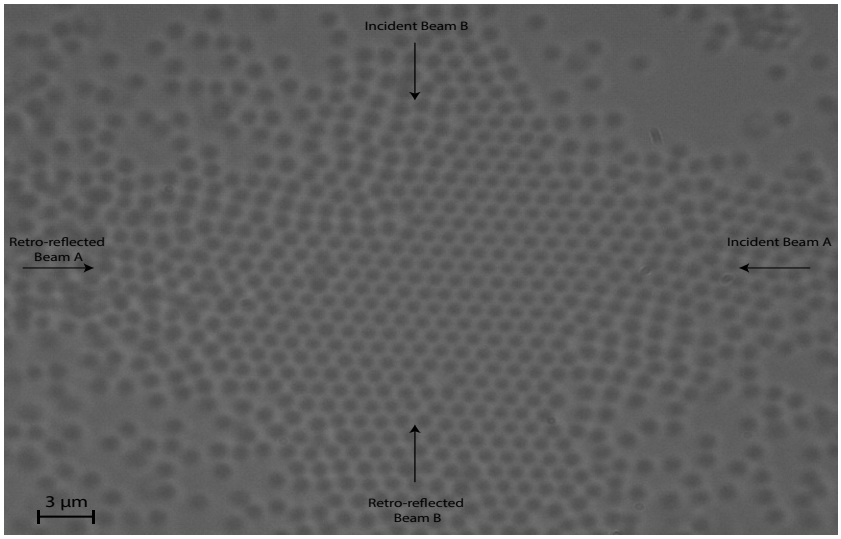

Figure 4.29: Hexagonal lattice formed by 1 μm silica spheres at the crossing point of two orthogonal counter-propagating beam pairs of orthogonal polarisations.

the silica spheres in this cluster are calculated in the same way as before. Figure 4.30 shows the traced particle centres in a video frame and the plot of the inter-particle distribution. The second peak in the separation distribution

plot labelled as γa is the lattice constant $c = a\sqrt{3}$ for a hexagonal lattice. Here we found $a = 1.01$ μm and $\gamma = 1.71$, indicating a hexagonal lattice.

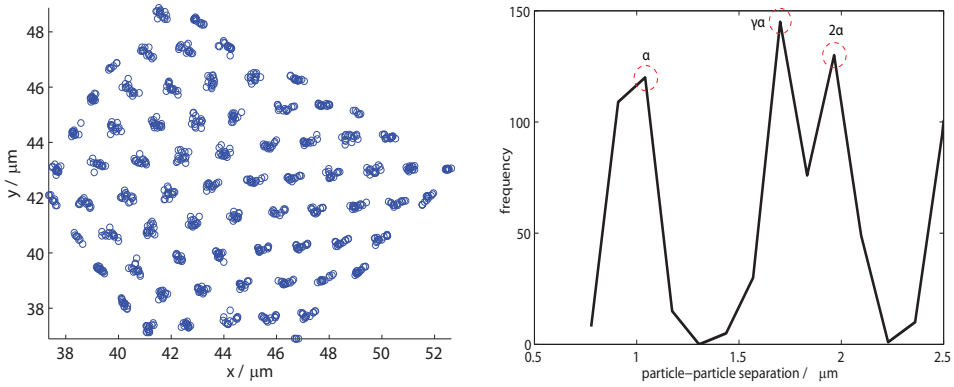

(a) **(b)**

Figure 4.30: Hexagonal lattice characterisation: (a) Particle centre trace; (b) Particle distance distribution, in hex lattice.

Figure 4.31a shows the optical landscape created by the two beam pairs in the background and the positions of the silica spheres. In this configuration despite there being some underlying structure from the incident beams, even with the effects of multiple scattering between the spheres there is no localization on a regular square lattice, and the spheres collapse into a close packed (hexagonal) array due to the optical interactions between the scattered fields. Figure 4.31b shows the particle set considered in Figure 4.31a.

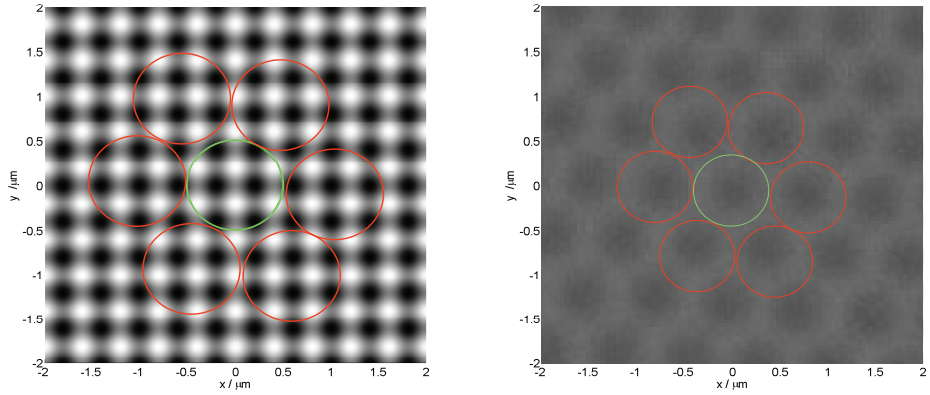

(a) **(b)**

Figure 4.31: Particle positions of 1 μm silica particles and optical landscape created by two cross polarised orthogonal beam pairs. (b) Image of actual particles considered in part (a).

Figure 4.32 shows the Voronoi diagram for this case. The cells here are

hexagons which reflects the fact that the bound lattice is hexagonal and have the same area as the lattice unit cell. The averaged area of the hexagonal Voronoi cells was found to be $(1.1 \pm 0.2)\mu m^2$. The area of the lattice unit cell obtained by using the measured nearest particle separation is $(1.0 \pm 0.1)\mu m^2$ and agrees with the Voronoi cell area with the calculated errors.

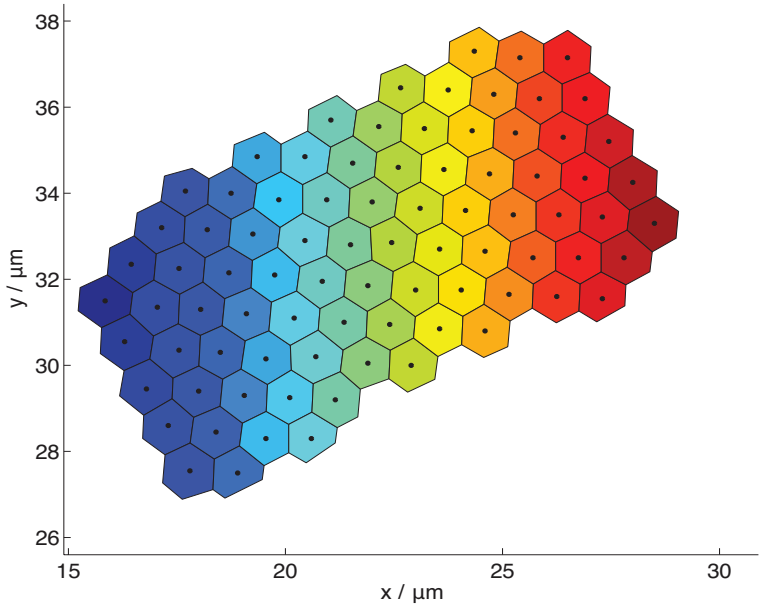

Figure 4.32: Voronoi diagram for the hexagonal lattice of 1.0 μm silica particles.

Finally, the bond orientational parameter ψ_6 is plotted as a function of time (Figure 4.33) for the case when the laser source is turned on (P = 0.954 W) and off. We observe that when the laser is on, ψ_6 is close to 1 for the whole video length. This shows once again that the bound array is regular hexagonal. When the laser source is switched off ψ_6 is varying and is of lower values.

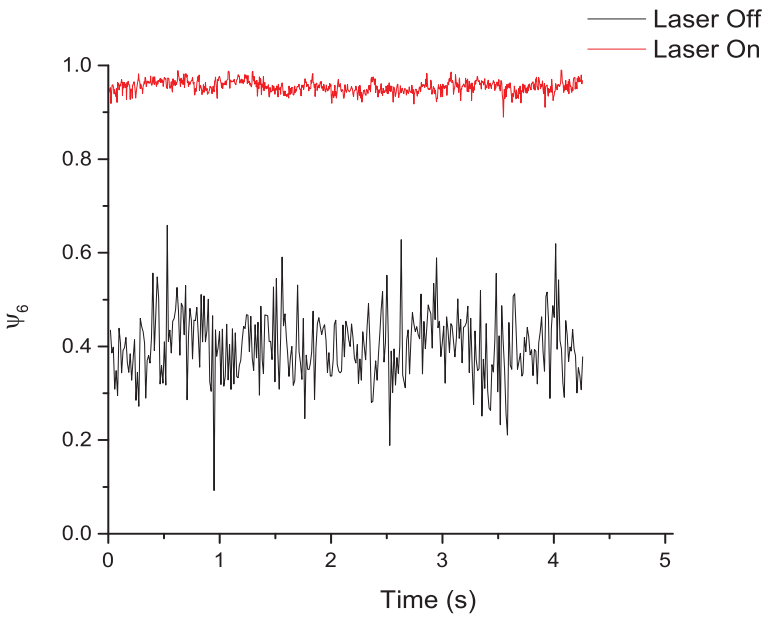

Figure 4.33: Bond orientational order parameter as a function of time for a hexagonal lattice. The black and red curves are for the cases when the laser source is switched off and on respectively.

4.4.2 Spring Constant

The spring constant of two-dimensional hexagonal arrays was derived in the same manner as in the one-dimensional optical binding experiment for silica particles with diameters 0.8 μm (Figure 4.34) and 1.0 μm. The spring constant was calculated for hexagonal arrays only since the 0.8 μm silica spheres did not form a square lattice for the parallel polarisations configuration. As the particle size becomes smaller the particles are influenced by less trapping sites thus a different bound geometry is observed. Furthermore, due to their large number, multiple particles are often closed packed over a single high intensity region. These statements once again agree with the observations made by Grzegorczyk *et al*, 2006.

Figure 4.35 shows the spring constant, κ as a function of the laser power after the 50:50 beam splitter i.e. the single beam power (Figure 3.7). The overall spring constant for each particle size is larger than that of the one-dimensional case. This is to be expected since the binding force increase with the number of bound particles and similarly the spring constant. In a two-dimensional array there is an order of magnitude more particles than in the one-dimensional case.

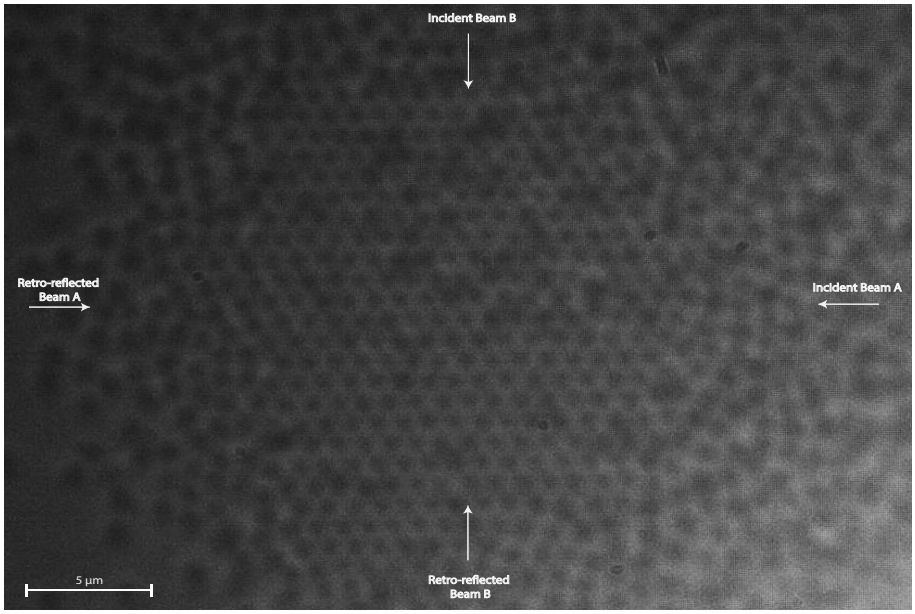

Figure 4.34: Hexagonal lattice formed by 0.8 μm silica spheres at the crossing point of two orthogonal counter-propagating beam pairs of orthogonal polarisations.

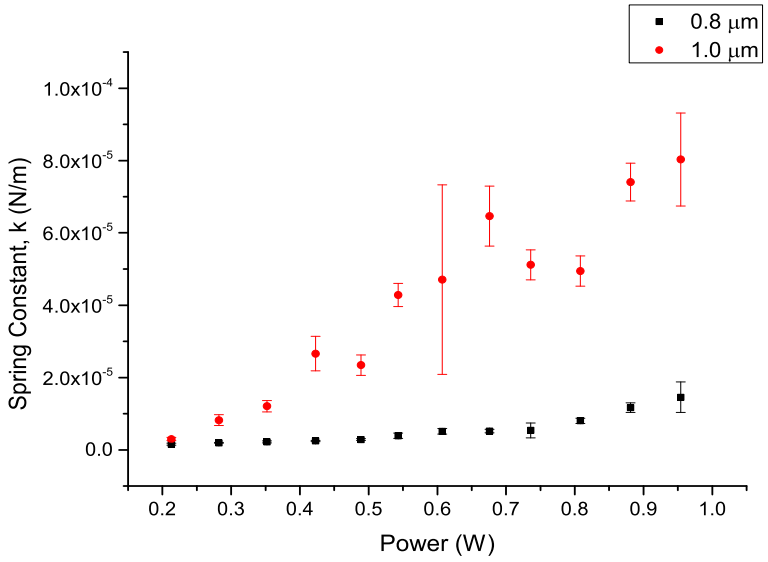

Figure 4.35: Spring constant vs Laser Power for 0.8 μm and 1.0 μm silica particles in a hexagonal two-dimensional array.

Finally, we compare the spring constant values obtained for square and hexagonal lattice formations of 1.0 μm silica particles at a laser power of 0.49 W. For the square lattice case the spring constant was found to be $\kappa_{sq}^{(1.0)} = (3.9\pm0.7)\times10^{-5}$ N/m and for the hexagonal case $\kappa_{hex}^{(1.0)} = (2.3\pm0.5)\times10^{-5}$ N/m. We observe that the confinement of the particles is stronger in the presence of interference fringes. This is in agreement with the results obtained for the one-dimensional cases.

4.5 Optical Binding of Carbon Nano-tubes (CNT)

In addition to the silica sphere experiments, we have successfully observed the one-dimensional optical binding of graphenated carbon nano-tube (CNT) bundles in the evanescent fields of two counter-propagating beams (Figure 4.36). It is to our knowledge that this is the first observation of optical binding of carbon nano-tubes or, indeed, any particle with a shape other than a sphere.

The carbon nano-tube bundles had lengths of 1 - 2 microns and diameters of few nano-meters and were provided by the Department of Engineering, Cambridge University. The CNT bundles were immersed in water and ultrasonicated before conducting the experiment. This was done to remove residual catalyst particles and big bundles. Using CNT bundles lead to complications as it was difficult to monitor them by the microscope objective due to their small diameter. For the same reason only a small number of these bundles would sink to the top surface of the prism and interact with the evanescent field. These complications may be overcome by using other types of elongated structures such as dielectric nano-wires which are more manageable.

The cylindrical particles would align along the propagation axis and not parallel to the interference fringes formed by the two counter-propagating beams. Theoretical models considering the Mie scattering and optical forces between finite cylindrical objects have been developed by various groups [65, 66, 67, 29]. Existing theoretical work does not describe the experimental observations described in this section. Even a simple theory for the orientation

of the cylinders under optical binding is lacking. Grzegorczyk *etal*. considered binding of cylinders only so that a 2D model could be implemented (i.e. it does not model the actual scenario of the experiment). Also, Andrews *etal*. presented calculations for a configuration where the CNTs are taken to be parallel to each other which was not observed in our experiments.

Videos of chain like CNT bound structures were recorded. The tracking of the nano-tubes was achieved by the use of another tracking software this time (Tracker by Douglas Brown, Cabrillo College) [68], since the code used for the spherical particles cannot handle cylindrical objects. The software creates a template image of a feature of interest and then searches each frame of the video for the best possible sub-pixel match of that template. The matching is done by comparing the template and the match pixels for RGB differences. Figure 4.37 shows the position of three different nano-tube bundles along the propagation axis in respect to time.

Histograms of the position fluctuations along the propagation axis were plotted in the same way as described before. Figure 4.38 shows an example of such a histogram. The spring constant was calculated for a laser power of P = 0.954 W to be $\kappa_{CNT} = (1.0 \pm 0.1) \times 10^{-6}$ N/m. The experiment was also carried out to study the orientation of the CNTs while rotating the polarisation of the incident and retro-reflected beams (both beams still having the same polarisation direction). No change in orientation was observed for different polarisations. We found that once the one-dimensional chain was formed, it persisted for all incident polarisations.

This system is still under investigation and a full explanation will require a full multiple scattering model for a number of finite cylindrical particles as a function of length, aspect ratio and orientation. An interesting future experiment might be to investigate the orientation of cylinders in this sort of optical binding experiment as a function of their length (as has been done for nano-wires in optical tweezers [69]).

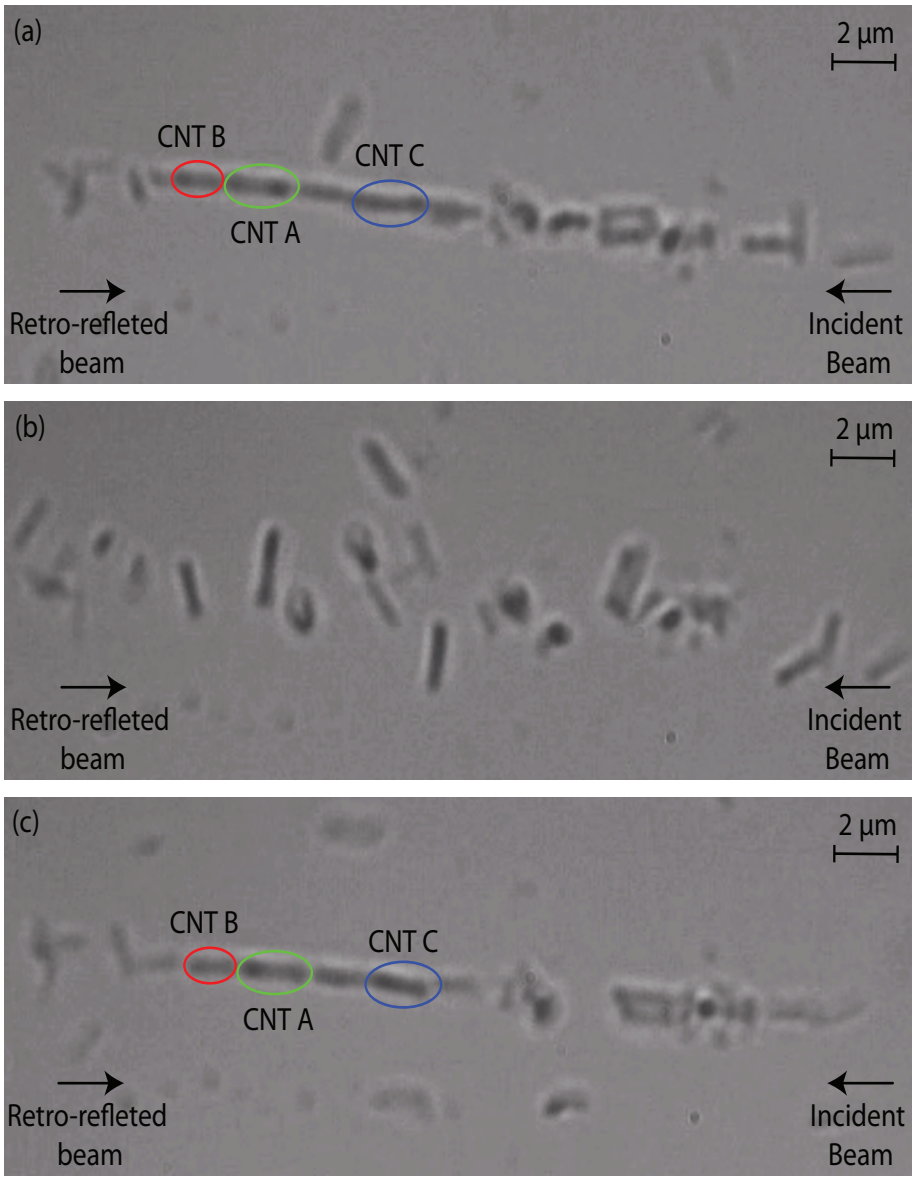

Figure 4.36: Optical Binding of Carbon Nano-tubes using evanescent waves. (a) CNTs in an optically bound chain; (b) Laser switched off and CNTs move freely in water; (c) Laser switched on and CNTs align themselves in one-dimensional chain again.

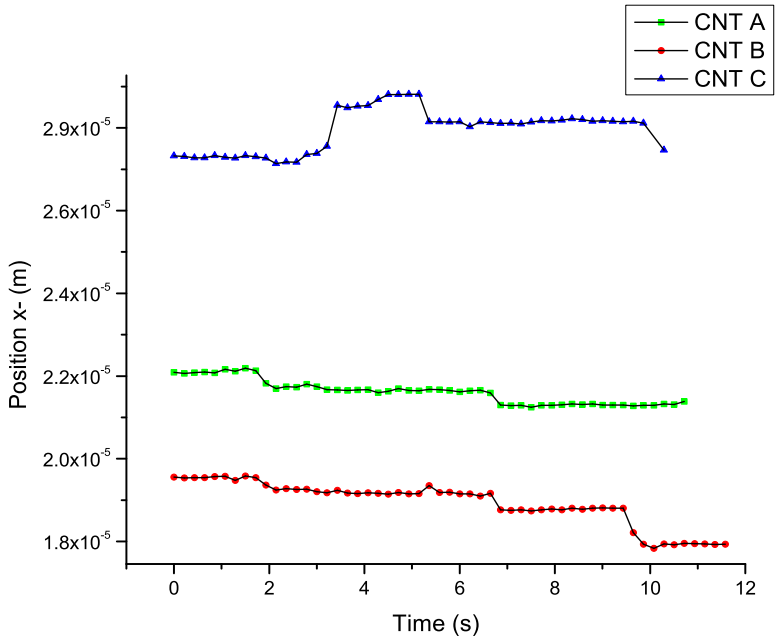

Figure 4.37: Carbon Nano-tubes trace with video microscopy.

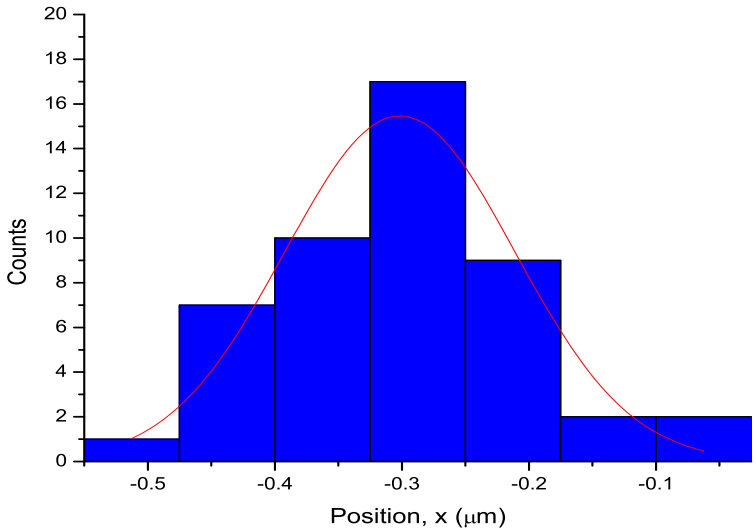

Figure 4.38: Carbon Nano-tubes position fluctuations histogram in one-dimensional bound structure for laser power, P = 0.954W and number of counts, N = 51.

4.6 Outlook

We have presented the results obtained on the evanescent field surface trap for two trapping configurations. The first configuration consisted of two-counter propagating beams lead to the formation of one-dimensional bound structures of spherical particles in the evanescent fields generated. The inter-particle separations in the chain like formations were experimentally measured for two polarisation configurations. The spring constant was also derived from the Brownian motion of the bound particles. The spring constant increases with laser intensity. The bound structures are more stable since the particles are held in deeper potential wells.

Similar results were obtained for the second trapping configuration, where two orthogonal pairs of counter-propagating beams were used to create two-dimensional bound arrays. Again, two different polarisation schemes were considered. The arrays were characterised and the spring constant was calculated in the same way as for the one-dimensional binding. We have found that for two orthogonal beam pairs with parallel polarisations the particles are bound in square-lattice bound structures. Alternatively when the beam pairs are cross-polarised the particles are trapped in a hexagonal-lattice geometry. The observations lead to the conclusion that the underlying interference pattern dictates the bound array geometry but not the exact trapping locations as the scattered fields modify the background field. In the case of absence of interference the particles arrange themselves in close packed arrays due to the optical binding force.

Finally, we have demonstrated the optical binding of carbon nano-tube bundles in the evanescent field of two counter-propagating fields. We observed that the orientation of the cylinder axis does not change with polarisation but further investigation is needed to deduct conclusions. Mono-dispersed carbon nano-tubes and the development of a tracking software that can detect the Brownian motion of cylindrical particles are needed to complete this study. The existing theoretical models treating infinite cylindrical objects having their

long axis parallel to each other cannot interpret the observations shown in this chapter since the scattered field at the edges of each particle has to be calculated. Even though a theoretical model is lacking, the alignment of carbon nano tubes as presented in this section could lead to new and interesting applications in nanotechnology.

The results presented in this chapter suggest that the optical binding force is the dominant force in this phenomenon. Deviations from theory, indicate that optical binding phenomena are highly sensitive to the experiment parameters (which cannot be measured precisely or omitted from the theory calculations). Additionally, the effects of hydrodynamic coupling and electrostatic interactions between the spheres and the substrate need to be considered for a more comprehensive understanding.

Chapter 5

Fields and Forces Around a Nano-Fibre

5.1 Introduction

A different approach for generating evanescent optical fields is considered in this chapter. An optical wave-guide with dimensions comparable to that of the guided light can be used to trap micro-particles. Examples of such sub-wavelength wave-guides are integrated and slot wave-guides [70, 71], optical wires [72] and optical fibres that are tapered to a diameter of 1 μm or less [27]. In this chapter we consider the use of the latter for optical manipulation. In these tapered fibres a large fraction of the power is carried in the evanescent field that penetrates a significant distance into the medium surrounding the fibre [26]. Such tapered optical fibres have been used to demonstrate evanescent wave trapping [8] and probing [73] of laser-cooled atoms. They have also been utilised for sensing [74] and in non-linear optics applications [75]. The trapping and guiding of microscopic particles using such configuration, rele-

vant to this thesis, has been also presented [9, 76, 77]. Recently the propulsion of biological samples, namely bacteria, was demonstrated [78].

In this chapter numerical calculations of the field distribution around a tapered optical fibre are presented. Furthermore, the optical trapping and scattering forces originating from the evanescent field in the tapered region are calculated using a simple dipole model. These calculations provide an insight to the behaviour of micro- and nano- particles around a nano-fibre. Additionally, plasmonic optical forces on metallic (silver and gold) nano-particles are calculated in this chapter. We show how the plasmon resonance of metallic nano-particles can be exploited to enhance the optical trapping force, and suggest how a two-colour or bi-chromatic nano-fibre trap [79] for plasmonic particles may be implemented for controlling the particle trajectory along the fibre.

5.2 Evanescent Field Distribution Around the Tapered Region of a Nano-Fibre

A single-mode optical fibre consists of the buffer coating, the cladding and the core glass. Typically the buffer coating has diameters of about 250 μm, the cladding 125 μm, and the core 6 μm. There is a small refractive index mismatch between the cladding and the core ($n_{clad} < n_{core}, |n_{core} - n_{clad}|/n_{core} << 1$). This ensures that light propagates along the core due total internal reflection (Figure 5.1). Snell's Law determines the angle at the core - cladding interface for a given incident angle at the air-core interface:

$$\theta_{inc} \leq \arcsin \sqrt{n_{core}^2 - n_{clad}^2} \tag{5.1}$$

where $\sqrt{n_{core}^2 - n_{clad}^2}$ is defined as the fibre numerical aperture.

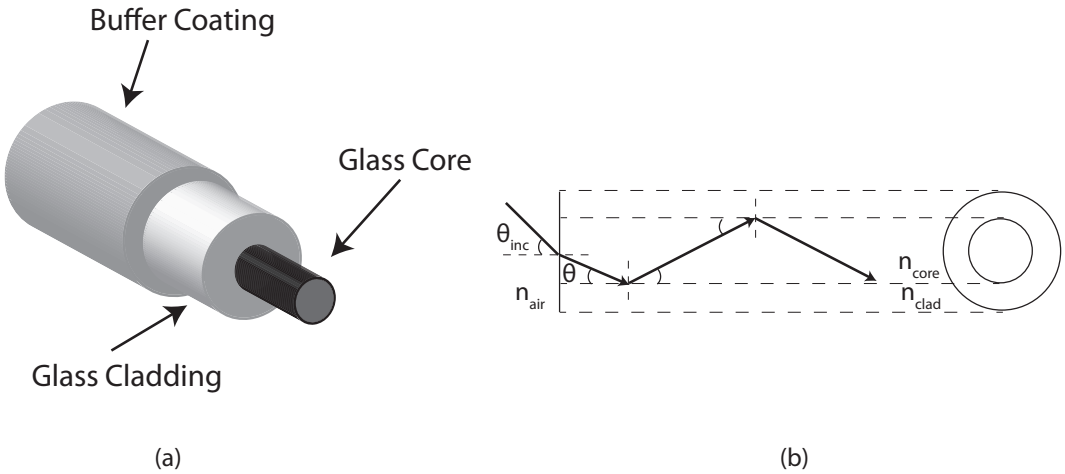

Figure 5.1: (a) Optical fibre cross-section; (b) Propagation of light ray in an optical fibre.

The electric field distribution around the tapered region of a nano-fibre can be calculated by using the exact solution of Maxwell's equations in a cylindrically symmetric geometry [80, 81, 82]. The boundary conditions require the transverse and longitudinal components of the electric and magnetic fields inside and outside the fibre core to be equal to each other at $r = \rho$, with ρ being the fibre core radius. Here we consider the case where n_1 is the refractive index of the fibre and n_2 the refractive index of the surrounding medium. In a standard optical fibre n_1 and n_2 are represented by n_{core} and n_{clad} respectively.

The Maxwell's equations in cylindrical coordinates are given by:

$$\nabla \times \bar{H} = \varepsilon(r)\frac{\partial \bar{E}}{\partial t}, \tag{5.2}$$

$$\nabla \times \bar{E} = -\mu_0\frac{\partial \bar{H}}{\partial t}, \tag{5.3}$$

$$\nabla \cdot (\varepsilon(r)\bar{E}) = 0, \tag{5.4}$$

$$\nabla \cdot \bar{H} = 0, \tag{5.5}$$

where $\varepsilon = n^2\varepsilon_0$ is the permittivity of the material and ε_0 is the permittivity of vacuum. μ_0 is the permeability of vacuum and is equal to 1 assuming that the material is non-magnetic. Equation 5.4 also assumes that there no charges i.e. in a dielectric. In the case where charges are present the right hand side of this equation is equal to the enclosed charge density. Combining Equations

5.2 - 5.5 we obtain the wave equation of the fields:

$$\nabla^2 \bar{E} - \mu_0 \varepsilon(r) \frac{\partial^2 \bar{E}}{\partial t^2} = -\nabla(\frac{\bar{E}}{\varepsilon(r)} \cdot \nabla \varepsilon(r)) \tag{5.6}$$

We write the solutions to Equation 5.6 for the z-component as follows:

$$E_z(\bar{r}, t) = E_z(r, \phi) \mathrm{e}^{i(\omega t - \beta z)}, \tag{5.7}$$

where β is the axial propagation constant of the field, i.e. the component of the wavevector, k, parallel to the fibre axis. Note that due to the symmetry of the problem $\partial\varepsilon(r)/\partial z$ vanishes and therefore we can express the radial and transverse components of the field E_r and E_ϕ in terms of E_z. The wave equation in cylindrical coordinates can be now obtained:

$$\left[\partial_r^2 r + \frac{1}{r}\partial_r + \frac{1}{r^2}\partial_\phi^2 + (k^2 - \beta^2)\right] E_z(r, \phi) = 0, \tag{5.8}$$

where $k^2 = \mu_0 \varepsilon \omega^2$. Equation 5.8 has solutions of the following form:

$$E_z(r, \phi) = R(r) \mathrm{e}^{i(\pm\ell)\phi} \tag{5.9}$$

where $\ell = 0, 1, 2, ...$ An equation for the radial variation of the electric field can be obtained:

$$\left[\partial_r^2 r + \frac{1}{r} + (k^2 - \beta^2 - \frac{\ell^2}{r^2})\right] R(r) = 0. \tag{5.10}$$

The general solutions of this equation are Bessel functions of order ℓ:

$$k^2 - \beta^2 \begin{cases} > 0 & R(r) = c_1 J_\ell(hr) + c_2 Y_\ell(hr), \\ < 0 & R(r) = c_3 I_\ell(qr) + c_4 K_\ell(qr), \end{cases} \tag{5.11}$$

where $J_l(x)$ is the Bessel function of the first kind, $Y_l(x)$ the Bessel function of the second kind, $I_l(x)$ the modified Bessel function of the first kind and $K_l(x)$ the modified Bessel function of the second kind. The transverse components

of the mode wavevector h and q for the fields inside and outside the fibre respectively satisfy the following equations:

$$h = (n_1^2 k_0^2 - \beta^2)^{1/2}, \tag{5.12}$$

$$q = (\beta^2 - n_2^2 k_0^2)^{1/2}, \tag{5.13}$$

with $k_0 = 2\pi/\lambda_0$ is the vacuum wavevector. The transverse component q outside the fibre is imaginary, implying a rapidly decaying evanescent field. The fields must be finite as r approaches zero and must vanish as r obtains large values. Therefore we can set $c_2 = c_3 = 0$ as Y_ℓ diverges for small arguments and I_ℓ diverges as $r \to \infty$. E_z can be then expressed as:

$$E_z(r, \phi, z, t) = AJ_\ell(hr)\mathrm{e}^{i(\omega t \pm \ell\phi - \beta z)} \tag{5.14}$$

for $r < \rho$. Similarly, H_z is given by:

$$H_z(r, \phi, z, t) = BJ_\ell(hr)\mathrm{e}^{i(\omega t \pm \ell\phi - \beta z)} \tag{5.15}$$

For $r > \rho$:

$$E_z(r, \phi, z, t) = CK_\ell(qr)\mathrm{e}^{i(\omega t \pm \ell\phi - \beta z)} \tag{5.16}$$

$$H_z(r, \phi, z, t) = DK_\ell(qr)\mathrm{e}^{i(\omega t \pm \ell\phi - \beta z)} \tag{5.17}$$

The following operator in cylindrical coordinates can be used along with Equations 5.2 and 5.3 to deduce expressions for the rest of the components of $\bar{E}$ and $\bar{H}$.

$$\left[\nabla \times \bar{A}\right]_{r,\phi,z} = (\frac{1}{r}\partial_\phi A_z - \partial_z A_\phi)\hat{r} + (\partial_z A_r - \partial_r A_z)\hat{\phi} + (\partial_r A_\phi - \frac{1}{r}\partial_\phi A_r)\hat{z} \tag{5.18}$$

E_r, E_ϕ, H_r and H_ϕ for $r < \rho$ can be expressed as:

$$E_r(r,\phi,z,t) = -\frac{\beta}{h}\left[iAJ'_\ell(hr) - \frac{\omega\mu_0(\pm\ell)}{\beta}B\frac{J_\ell(hr)}{hr}\right]\mathrm{e}^{i(\omega t\pm\ell\phi-\beta z)}, \tag{5.19}$$

$$E_\phi(r,\phi,z,t) = \frac{\beta}{h}\left[(\pm\ell)A\frac{J_\ell(hr)}{hr} + \frac{i\omega\mu_0}{\beta}BJ'_\ell(hr)\right]\mathrm{e}^{i(\omega t\pm\ell\phi-\beta z)}, \tag{5.20}$$

$$H_r(r,\phi,z,t) = -\frac{\beta}{h}\left[iBJ'_\ell(hr) - \frac{\omega\varepsilon_1(\pm\ell)}{\beta}A\frac{J_\ell(hr)}{hr}\right]\mathrm{e}^{i(\omega t\pm\ell\phi-\beta z)}, \tag{5.21}$$

$$H_\phi(r,\phi,z,t) = \frac{\beta}{h}\left[(\pm\ell)B\frac{J_\ell(hr)}{hr} + \frac{i\omega\varepsilon_1}{\beta}AJ'_\ell(hr)\right]\mathrm{e}^{i(\omega t\pm\ell\phi-\beta z)}, \tag{5.22}$$

where $\varepsilon_1 = n_1^2\varepsilon_0$, the dielectric constant inside the fibre. For $r > \rho$:

$$E_r(r,\phi,z,t) = \frac{\beta}{q}\left[iCK'_\ell(qr) - \frac{\omega\mu_0(\pm\ell)}{\beta}D\frac{K_\ell(qr)}{qr}\right]\mathrm{e}^{i(\omega t\pm\ell\phi-\beta z)}, \tag{5.23}$$

$$E_\phi(r,\phi,z,t) = -\frac{\beta}{q}\left[(\pm\ell)C\frac{K_\ell(qr)}{qr} + \frac{i\omega\mu_0}{\beta}DK'_\ell(qr)\right]\mathrm{e}^{i(\omega t\pm\ell\phi-\beta z)}, \tag{5.24}$$

$$H_r(r,\phi,z,t) = \frac{\beta}{q}\left[iDK'_\ell(qr) + \frac{\omega\varepsilon_2(\pm\ell)}{\beta}C\frac{K_\ell(qr)}{qr}\right]\mathrm{e}^{i(\omega t\pm\ell\phi-\beta z)}, \tag{5.25}$$

$$H_\phi(r,\phi,z,t) = -\frac{\beta}{q}\left[(\pm\ell)D\frac{K_\ell(qr)}{qr} - \frac{i\omega\varepsilon_2}{\beta}CK'_\ell(qr)\right]\mathrm{e}^{i(\omega t\pm\ell\phi-\beta z)}, \tag{5.26}$$

where $J'(x) = dJ(x)/dx$ and $K'(x) = dK(x)/dx$ are their derivatives and $\varepsilon_2 = n_2^2\varepsilon_0$, the dielectric constant of the surrounding medium. The $\pm\ell$ in the exponential corresponds to solutions for circular polarisation with the + sign corresponding to clockwise and the − sign to counter-clockwise rotations of the transverse component $E_\perp$ around the fibre axis. For linearly polarised light instead of Equation 5.9 we use $E_z(r,\phi) = R(r)\cos(\ell\phi)$ or $E_z(r,\phi) = R(r)\sin(\ell\phi)$ depending on the direction of the polarisation. The index ℓ is also related to the orbital angular momentum of the propagating field since an individual photon may have an orbital angular momentum with values $\ell\hbar$ [83].

The boundary conditions dictate that the transverse components of the electric and magnetic fields are continuous across the boundary. These are the same boundary conditions used in the derivation of the Mie scattering formulae

shown in Chapter 2.

$$E_{\phi,z}^{(n_1)}(r=\rho) = E_{\phi,z}^{(n_2)}(r=\rho) \tag{5.27}$$

$$H_{\phi,z}^{(n_1)}(r=\rho) = H_{\phi,z}^{(n_2)}(r=\rho) \tag{5.28}$$

Imposing these boundary conditions on Equations 5.14 - 5.26 we obtain the magnitudes A, B, C, and D:

$$AJ_\ell(h\rho) - CK_\ell(q\rho) = 0, \tag{5.29}$$

$$A\left[\frac{i(\pm\ell)}{h^2\rho}J_\ell(h\rho)\right] + B\left[-\frac{\omega\mu_0}{h\beta}J'_\ell(h\rho)\right] + C\left[\frac{i(\pm\ell)}{q^2\rho}K_\ell(q\rho)\right] + D\left[-\frac{\omega\mu_0}{q\beta}K'_\ell(q\rho)\right] = 0, \tag{5.30}$$

$$BJ_\ell(h\rho) - DK_\ell(q\rho) = 0, \tag{5.31}$$

$$A\left[\frac{\omega\varepsilon_1}{h\beta}J'_\ell(h\rho)\right] + B\left[\frac{i(\pm\ell)}{h^2\rho}J_\ell(h\rho)\right] + C\left[\frac{\omega\varepsilon_2}{q\beta}K'_\ell(q\rho)\right] + D\left[\frac{i(\pm\ell)}{q^2\rho}K_\ell(q\rho)\right] = 0. \tag{5.32}$$

Equations 5.29 - 5.32 are written as a matrix equation with the requirement that the determinant must vanish:

$$\begin{vmatrix} J_\ell(h\rho) & 0 & -K_\ell(q\rho) & 0 \\ \frac{i(\pm\ell)}{h^2\rho}J_\ell(h\rho) & -\frac{\omega\mu_0}{h\beta}J'_\ell(h\rho) & \frac{i(\pm\ell)}{q^2\rho}K_\ell(q\rho) & -\frac{\omega\mu_0}{q\beta}K'_\ell(q\rho) \\ 0 & J_\ell(h\rho) & 0 & -K_\ell(q\rho) \\ \frac{\omega\varepsilon_1}{h\beta}J'_\ell(h\rho) & \frac{i(\pm\ell)}{h^2\rho}J_\ell(h\rho) & \frac{\omega\varepsilon_2}{q\beta}K'_\ell(q\rho) & \frac{i(\pm\ell)}{q^2\rho}K_\ell(q\rho) \end{vmatrix} = 0 \tag{5.33}$$

Finally, the fibre eigenvalue equation is obtained by evaluating the determinant of the above matrix:

$$\begin{aligned} \left(\frac{J'_\ell(h\rho)}{h\rho J_\ell(h\rho)} + \frac{K'_\ell(q\rho)}{q\rho K_\ell(q\rho)}\right)\left(\frac{n_1^2 J'_\ell}{h\rho J_\ell(h\rho)} + \frac{n_2^2 K'_\ell(q\rho)}{q\rho K_\ell(q\rho)}\right) \\ = \left(\frac{l\beta}{k_0}\right)^2\left[\left(\frac{1}{h\rho}\right)^2 + \left(\frac{1}{q\alpha}\right)^2\right]^2, \end{aligned} \tag{5.34}$$

The $J'_\ell(x)$ and $K'_\ell(x)$ terms can be substituted by $J'_\ell(x) = J_{\ell-1}(x) - \frac{\ell}{x}J_\ell(x)$ and $K'_\ell(x) = -\frac{1}{2}\left[K_{\ell-1}(x) + K_{\ell+1}(x)\right]$ respectively. Equation 5.34 can be then re-written as:

$$\frac{J_{\ell-1}(h\rho)}{h\rho J_\ell(h\rho)} = \left(\frac{n_1^2 + n_2^2}{2n_1^2}\right)\frac{K_{\ell-1}(q\rho) + K_{\ell+1}(q\rho)}{2q\rho K_\ell(q\rho)} + \frac{\ell}{(h\rho)^2} \pm R, \tag{5.35}$$

with

$$R = \left[\left(\frac{n_1^2 - n_2^2}{2n_1^2} \right)^2 \left(\frac{K_{\ell-1}(q\rho) + K_{\ell+1}(q\rho)}{2q\rho K_\ell(q\rho)} \right)^2 + \left(\frac{\ell\beta}{n_1 k_0} \right)^2 \left(\frac{1}{(q\rho)^2} + \frac{1}{(h\rho)^2} \right)^2 \right]^{1/2} \tag{5.36}$$

The positive and negative solutions in Equation 5.35 come from the fact that Equation 5.34 is quadratic. This leads to two different sets of modes: the HE for the negative sign and the EH for the positive. For the HE mode H_z is greater than E_z and for the EH mode the opposite. These modes are labelled as $\mathrm{HE}_{\ell\mathrm{m}}$ and $\mathrm{EH}_{\ell\mathrm{m}}$. Index m is a radial mode index which gives the number of radial nodes in the field for a fixed ℓ. The values of m that are possible depend on the radius of the fibre. For the case where $\ell = 0$ the modes are labelled as $\mathrm{TE}_{0\mathrm{m}}$ and $\mathrm{TM}_{0\mathrm{m}}$. These are special cases where these transverse modes have at least one vanishing component ($\mathrm{TE}_{0\mathrm{m}}$ has zero longitudinal electric field and $\mathrm{TM}_{0\mathrm{m}}$ has zero longitudinal magnetic field) whereas EH and HE modes have none of their components vanishing.

5.3 Mode Calculations Guided in Tapered Fibres

Here we consider the HE_{11} fundamental mode with quasi-linear and circular polarisations, individually, propagating in a tapered fibre. The calculations that follow are based on the equations derived in Section 5.2. The fundamental mode was chosen for this calculations since it is the only mode allowed to propagate in the taper for diameters up to 1.4 μm surrounded by water at $\lambda = 1064$ nm. This is shown in Figure 5.2 which is a plot of the propagation constant β normalised to k_0 as a function of the fibre diameter for the hybrid modes HE and EH. As it will be discussed in later chapters the tapered fibres achieved experimentally typically have diameters of less than 1.0 μm and therefore meet the single mode condition. For all the cases considered here the dispersion of the fused silica glass of the optical fibre was taken into account using the tabulated Sellmeier coefficients [84].

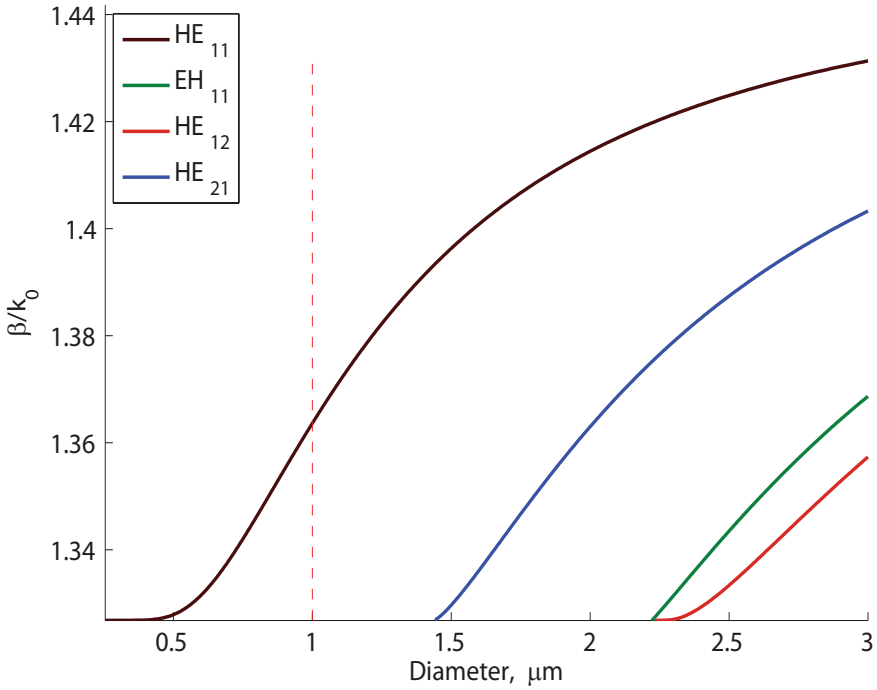

Figure 5.2: Normalised propagation constant β/k_0 vs Fibre diameter. The dashed red line indicates the 1μm diameter which corresponds to the diameter achieved experimentally.

5.3.1 Linearly Polarised Light

In this section, we study the case of the quasi-linearly (x-) polarised mode (electric field in the y- direction not completely negligible) HE_{11} guided in an optical fibre with radius $\rho = 0.25$ μm and surrounded by water. The penetration depth of the evanescent wave generated is $\Lambda = q^{-1} \simeq 16\rho$. Figure 5.3 shows the field distributions for this case. The fibre can support only the fundamental mode since the cut-off frequency for single mode operation is $V_c = 2.405$ which is greater than the normalised size parameter of the taper, $V = k\rho\sqrt{n_1^2 - n_2^2} \simeq 0.831$.

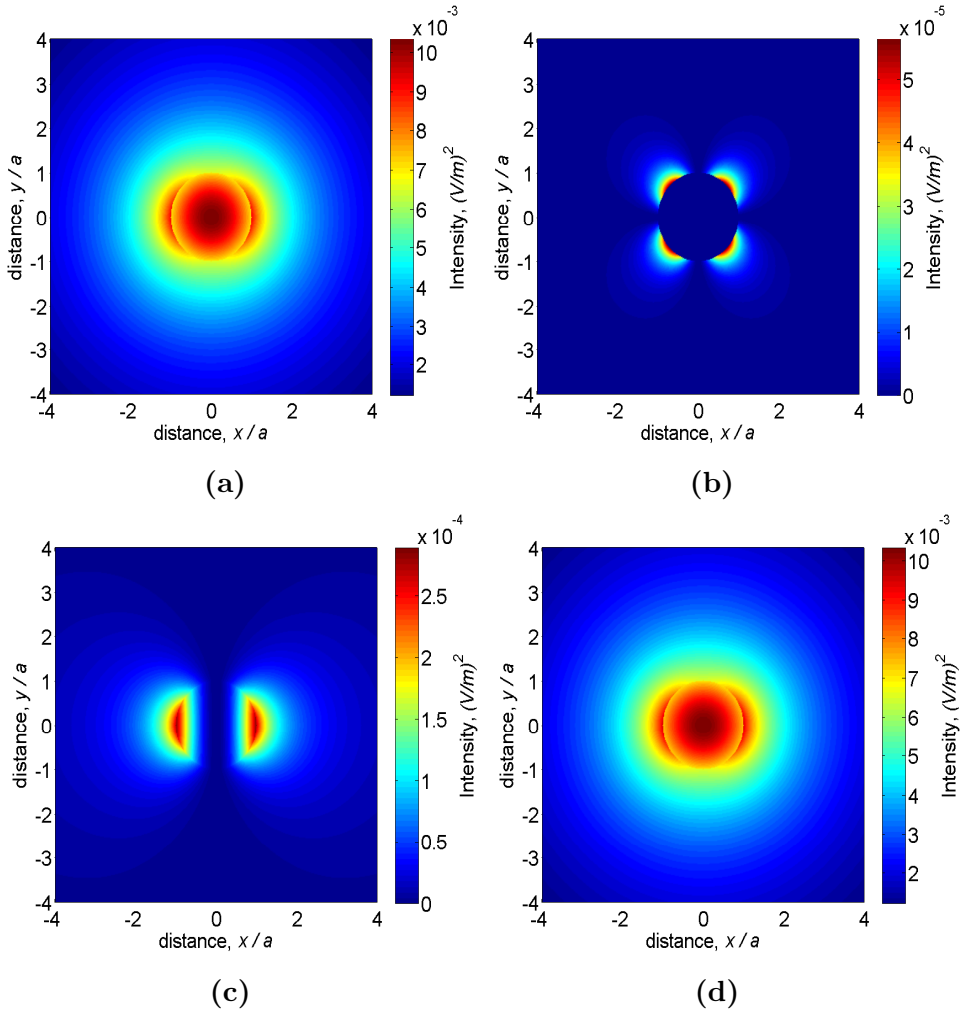

Figure 5.3: Directed fields for the quasi-linearly (x-) polarised fundamental HE_{11} mode in silica fibre with radius 250 nm, wavelength $\lambda = 1.064$ μm and total mode power $P = 3.9 \times 10^{-11}$ W. (a) field in the dominant polarisation direction, x; (b) field in the orthogonal polarisation direction, y; (c) field in the propagation direction, z; (d) Total field.

It is apparent in Figure 5.4 that a discontinuity of $|E_x|^2$ is observed at the fibre surface in the x- direction but not in the y-. This is due to the conditions for continuity of the electric field components perpendicular ($\varepsilon_1 E_1^{\perp} = \varepsilon_2 E_2^{\perp}$) and parallel ($E_1^{\parallel} = E_2^{\parallel}$) to the fibre surface.

Even though the intensities of the transverse component E_y and the longitudinal component E_z are weaker than the intensity of the major transverse component E_x they are not insignificant. Since the transverse components of the electric field have the same phase, the orientation of the total transverse component $E_{\perp}$ varies slightly in direction due to the small component of E_y. However, there is a phase difference of $\pi/2$ between the transverse components and the longitudinal component E_z causing the total electric field $\bar{E}$ to rotate elliptically in a plane parallel to the propagation axis, z. Furthermore, inside

the fibre there is a small variation in the transverse component direction due to the non-zero E_y component hence the designation quasi-linear polarization. Outside the fibre, E_y is considerable causing $E_\perp$ to vary in space [85].

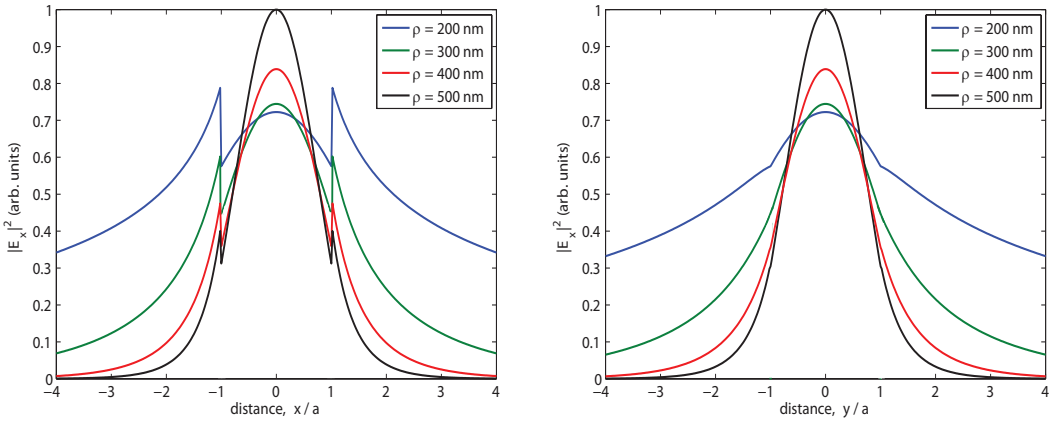

(a) **(b)**

Figure 5.4: $|E_x|^2$ in the fundamental mode HE_{11} with quasi-linear (x-) polarisation for various fibre radii and $\lambda = 1064$ nm. (a) as a function of x at $y = 0$. A discontinuity in the field at the boundary of the fibre is observed for all cases; (b) as a function of y at $x = 0$. The penetration depth Λ of the evanescent wave generated increases as the fibre radius decreases. The parameters for the black curve are close to those used to conduct experiments.

5.3.2 Circularly Polarised Light

Next, we consider the case of the circularly polarised HE_{11} mode which is guided in an optical fibre with the same parameters as in the previous section. Figure 5.5a shows the field distribution of the intensity of the transverse component of the electric field while Figure 5.5b shows the intensity distribution of the longitudinal component of the electric field. The moduli of longitudinal and transverse components for various fibre radii are shown in Figure 5.7. Similarly to the quasi linear polarisation case the penetration depth Λ of the evanescent wave generated increases as the fibre radius decreases.

The total intensity for this case is cylindrically symmetric. $|E_x|^2$ in the x-direction and $|E_y|^2$ in the y-direction have equal magnitudes and phase difference of $\pi/2$ indicating that inside the fibre the total transverse component of the electric field is circularly polarised. For the region outside the magnitude of ellipticity is constant, but there is an azimuthal phase gradient as the intensities of the two transverse components differ from each other with ϕ. The longitudinal component of the electric field E_z is cylindrically symmetric

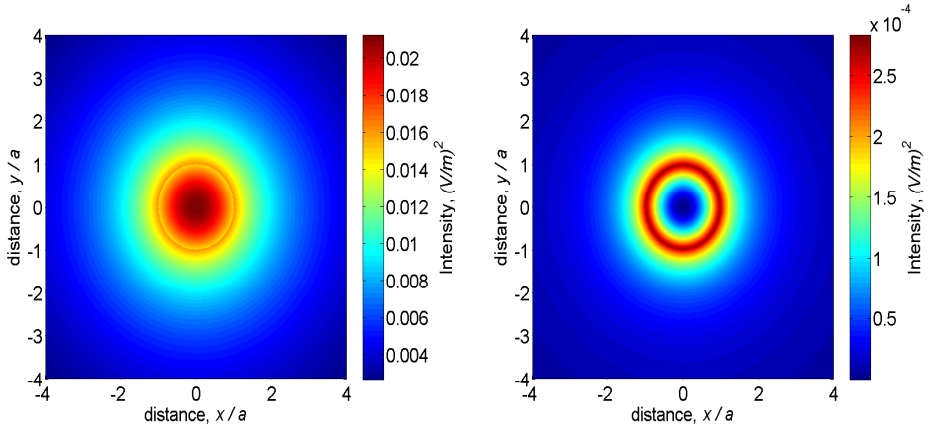

Figure 5.5: Directed fields magnitudes for the circularly polarised fundamental HE_{11} mode in silica nano-fibre with radius 250 nm, wavelength $\lambda = 1.064$ μm. (a) transverse component field; (b) longitudinal component field.

in the whole cross-section plane. Even though it is smaller than the transverse components it cannot be neglected [85].

5.4 Optical Forces Around Tapered Optical Fibres

In this section we consider the forces originating from the evanescent field of a tapered fibre. These optical forces acting on particles with radius r in the vicinity of the tapered region can be calculated for the Rayleigh regime ($r << \lambda$) in contrast with Mie regime ($r \approx \lambda$) discussed in Chapter 2. For this case the particles can be considered as point dipoles in an inhomogeneous electric field.

When a sphere is in an external electromagnetic field $\bar{E}$, a dipole moment is induced [86]:

$$\bar{d} = \alpha \bar{E} \tag{5.37}$$

where α is an effective polarisability that accounts for the effects of dynamic depolarization and radiative reaction [87] (see Section 5.4.1).

Using Lorentz force law and Maxwell's equations we get an expression for the time-averaged force acting on the dipole [88]:

$$\langle \bar{F} \rangle = \frac{1}{2} \mathrm{Re} \left(\sum^{i} \alpha E_i(r_1) \nabla E_i^*(r)|_{r=r_1} \right) \tag{5.38}$$

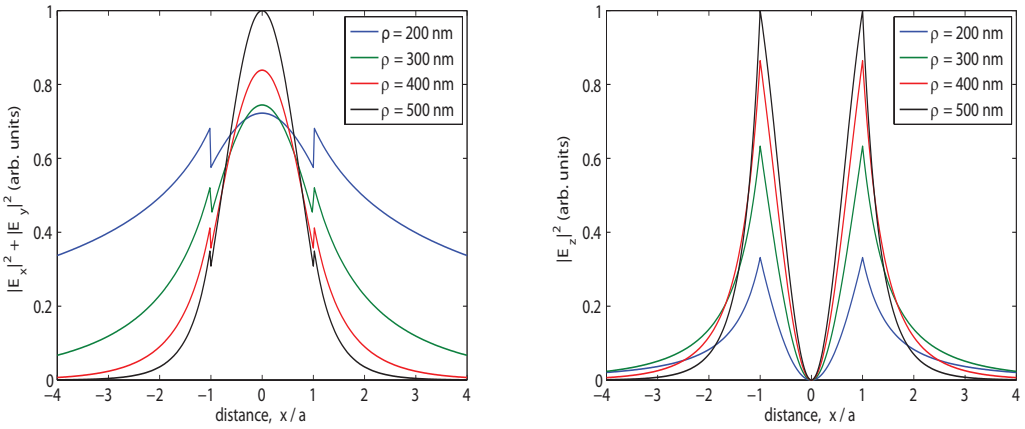

(a) **(b)**

Figure 5.6: (a) $|E_x|^2 + |E_y|^2$ as a function of x at $y = 0$; (b) $|E_z|^2$ as a function of x at $y = 0$. The penetration depth Λ of the evanescent wave generated increases as the fibre radius decreases. The parameters for the black curve are close to those used to conduct experiments.

By using the vector identity $\sum_i E_i \nabla E_i^* = (\bar{E} \cdot \nabla)\bar{E}^* + \bar{E} \times (\nabla \times \bar{E}^*)$ and $\nabla \times \bar{E} = i\omega\mu_0 \bar{H}$, Equation 5.38 can be re-written as:

$$\langle \bar{F} \rangle = \frac{1}{4}\mathrm{Re}(\alpha)\nabla|\bar{E}|^2 + \frac{\sigma_{scat}}{2c} Re(\bar{E} \times \bar{H}^*) + \frac{\sigma_{scat}}{2}\mathrm{Re}\left(i\frac{\varepsilon_0}{k_0}(\bar{E} \cdot \nabla)\bar{E}^*\right), \quad (5.39)$$

where c is the speed of light in vacuum and σ_{scat} is the scattering cross-section. The first term of the equation is the *'gradient force'* which is proportional to the gradient of the irradiance $|\bar{E}|^2$ [12]. The second term is the optical *'scattering force'* containing the time-averaged Poynting vector $\langle \bar{S} \rangle = \frac{1}{2}\mathrm{Re}(\bar{E} \times \bar{H}^*)$.

The third term is a force arising from the gradient of the time-averaged spin density [89]. In order to obtain a simplified expression for the time-averaged spin density we apply the vector identity $-2i\mathrm{Im}\{(\bar{E}^* \cdot \nabla)\bar{E}\} = \nabla \times (\bar{E} \times \bar{E}^*)$. Therefore:

$$\frac{\sigma_{scat}}{2} Re\left(i\frac{\varepsilon_0}{k_0}(\bar{E} \cdot \nabla)\bar{E}^*\right) = \sigma_{scat} c \nabla \times \left(\frac{\varepsilon_0}{4i\omega}(\bar{E} \times \bar{E}^*)\right) \quad (5.40)$$

The time-averaged spin density is given by:

$$\langle \bar{L}_S \rangle = \frac{\varepsilon_0}{4i\omega}(\bar{E} \times \bar{E}^*) \quad (5.41)$$

The curl of the spin density of the field is a force which is zero for a plane

wave [90] but it may significant when this is not the case such as high numerical aperture systems [91] or in the presence of strong polarisation gradients which makes it important to the discussion related to the evanescent fields around a tapered fibre.

Radiation pressure originates from the momentum transfer to the particle and it is in the direction of the momentum transfer which is the same as the direction of the propagating beam. It contains both the scattering and the spin curl forces. Both these forces contain the scattering cross-section σ_{scatt} which for a small particle can be expressed as:

$$\sigma_{scatt} = \frac{128r^6\pi^5}{3\lambda^4}\left[\frac{(n_{sph}/n_{med})^2 - 1}{(n_{sph}/n_{med})^2 + 2}\right]^2 \tag{5.42}$$

For unidirectional mode propagation in the tapered fibre, the gradient force traps the particles against the fibre and the radiation pressure, directed parallel to the fibre, propels the particles in the propagation direction (see Chapter 7).

The spin curl force is of high significance for strongly localised fields such as in the focal volume of high numerical aperture objective lens [91] and it is expected to be the case for guided modes in high numerical aperture fibres. Figure 5.7 shows the non-zero components of the spin density for the circularly-polarised HE_{11} mode guided in a fibre of radius $\rho = 500$ nm immersed in water.

The Poynting vector $\bar{S} = (1/2)\mathrm{Re}[\bar{\mathrm{E}} \times \bar{\mathrm{H}}^*]$ in a linear polarisation configuration has a non-zero longitudinal component and a zero azimuthal component. For the circularly polarised case both these components are non-zero which implies that particles in the vicinity of the tapered region will be driven in a helical trajectory along and around the fibre as it was calculated previously for ultra-cold atoms [92]. The radial component of the Poynting vector $S_r = (1/2)\mathrm{Re}[\mathrm{E}_\phi \mathrm{H}_\mathrm{z}^* - \mathrm{E}_\mathrm{z}\mathrm{H}_\phi^*]$ is zero for guided modes in any fibre structure [93]. Figure 5.8 shows the non-zero components of the Poynting vector for both linear and circular polarisations.

The presence of non-zero azimuthal components of the Poynting vector and the curl of the spin density give rise to an additional component to the force transverse to the axis of the fibre.

When calculating the optical forces we neglect the effects of multiple scattering between the particle and the tapered fibre. We assume that the particle is not too close to the fibre and that the contrast in the dielectric constant between the substrate and the surrounding medium is relatively low [94].

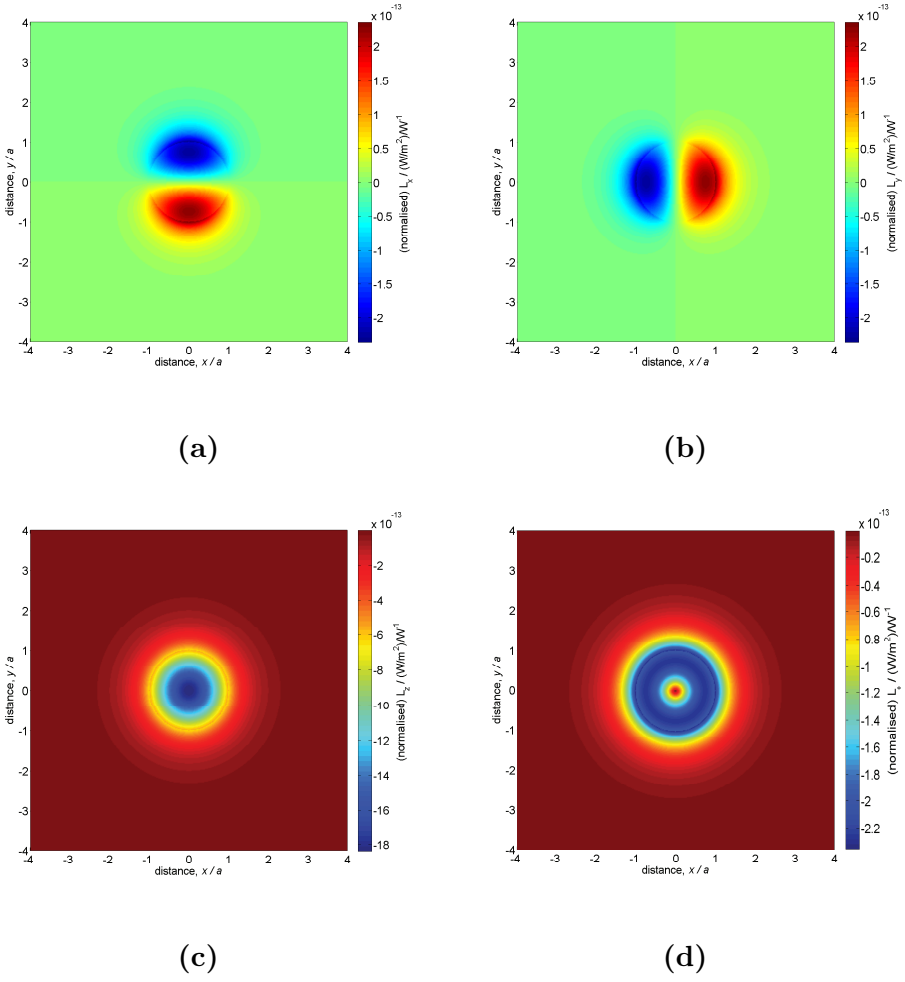

Figure 5.7: Components of the spin density in circularly polarised HE_{11} mode guided in a tapered fibre of radius $\rho = 500$ nm and $\lambda = 1064$ nm. (a) x-component; (b) y-component; (c) z-component; (d) ϕ-component.

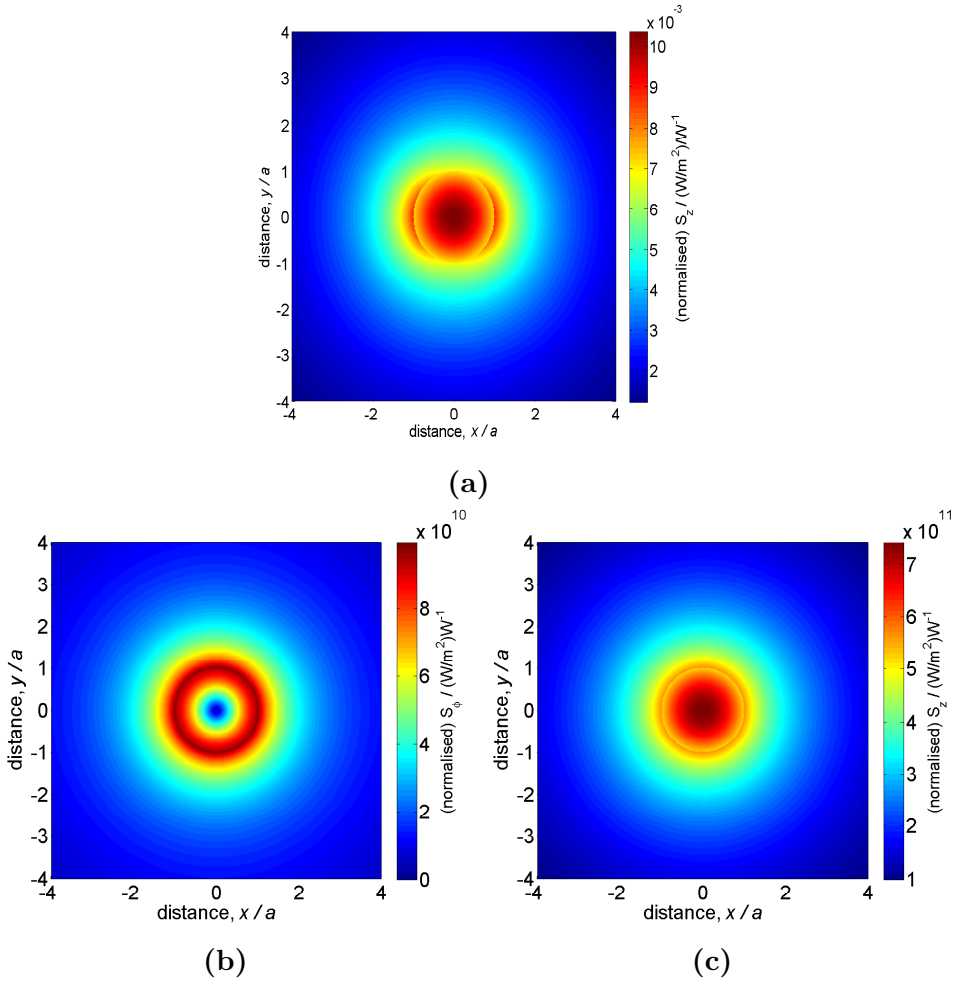

Figure 5.8: Non-zero components of the Poynting vector for the quasi-linearly (x-) and circularly polarised fundamental HE_{11} modes in a silica fibre with radius 250 nm, wavelength $\lambda = 1.064$ μm and total mode power $P = 3.9 \times 10^{-11}$ W. (a) Longitudinal component for the quasi-linearly (x-) polarisation; (b) azimuthal component and (c) longitudinal component for circular polarisation.

Additionally, we must keep in mind that particles in water solution experience a Brownian motion due to thermal fluctuations. The thermal energy of a particle is given by $k_B T$, where k_B is the Boltzmann constant and T is the temperature in Kelvin. This suggests that if the thermal energy is greater than the trapping potential (integral of gradient force):

$$U = \frac{2\pi n_{med} r^3}{c} \left[\frac{(n_{sph}/n_{med})^2 - 1}{(n_{sph}/n_{med})^2 + 2} \right], \tag{5.43}$$

the particle is likely to escape the trap.

5.4.1 Interaction with Metallic Nano-particles

First, we briefly discuss the Lorentz-Drude model which uses a number of damped harmonic oscillators to model the resonances in the frequency response of the metal.

The Drude model assumes that the valence electrons of the metallic atoms are free to move in the metallic structure while the metallic ions act as the immobile positive charges [95].

When a time-dependent electric field, $E(t) = E_0 e^{-i\omega t}$, is applied on a metal electrons exhibit an oscillatory motion, $x(t) = x_0 e^{-i\omega t}$. The equation of motion for the electrons is given by:

$$m_e \frac{\partial^2 x}{\partial t^2} + m_e \Gamma_0 \frac{\partial x}{\partial t} = -qE, \tag{5.44}$$

where m_e is the electron mass, Γ_0 is the collision dumping frequency and $q = e$ the electron charge. Solving the above equation leads to:

$$\varepsilon^{(f)}(\omega) = 1 - \frac{\Omega_p^2}{\omega(\omega - i\Gamma_0)}, \tag{5.45}$$

where $\varepsilon^{(f)}(\omega)$ is the intraband part of the dielectric function for the free-electron effects where Ω_p is the plasmon frequency of the free electron gas:

$$\Omega_p = \sqrt{\frac{n_d e^2}{m_e \varepsilon_0}}, \tag{5.46}$$

where n_d is the electron number density. Since the refractive index of a material is $n = \sqrt{\varepsilon(\omega)}$, the relation between ω_p ($\omega_p = \Omega_p/\sqrt{1/\Gamma_0}$) and ω determines whether the material is transparent or opaque. If $\omega_p > \omega$ the dielectric constant function is negative and therefore the refractive index is imaginary implying that the electron motion is sufficient to shield the electric field from entering the material. However if $\omega_p < \omega$ then the refractive index is positive meaning that electrons are unable to shield the light from entering the material which becomes transparent.

The interband part of the dielectric function for the bound electron effects is resembled by the Lorentz model result for insulators [96]:

$$\varepsilon^{(b)}(\omega) = \sum_{k=1}^{K} \frac{f_k \omega_p^2}{(\omega_k^2 - \omega^2) + i\omega\Gamma_k}, \tag{5.47}$$

where k is the number of oscillators with frequency ω_k, strength f_k and lifetime $1/\Gamma_k$.

The dielectric function $\varepsilon(\omega)$ can be expressed as the sum of $\varepsilon^{(f)}(\omega)$ and $\varepsilon^{(b)}(\omega)$ and is contained in the polarisability of small particles which is found from an expansion of the first TM mode of Mie theory to the second order in the size parameter, $x = \pi r/\lambda_0$ [87]:

$$\alpha(\omega) = \frac{1 - \frac{1}{10}(\varepsilon(\omega) + \varepsilon_m)x^2}{\left(\frac{1}{3} + \frac{\varepsilon_m}{\varepsilon(\omega) - \varepsilon_m}\right) - \frac{1}{30}(\varepsilon(\omega) + 10\varepsilon_m) - i\frac{4\pi^2\varepsilon_m^{3/2}}{3}\frac{V}{\lambda_0^3}} V \tag{5.48}$$

where V is the volume of the particle. For larger particles the Rayleigh approximation fails and retardation effects need to be accounted [97]. The above expression for the polarizibility reproduces the shift to longer wavelengths of the plasmon resonance with increasing particle size. The polarisability of metallic particles is larger than that of dielectric ones [98]. Hence the imaginary part of polarisability is of high significance for metallic particles. We can then express the absorption, σ_{abs}, and scattering, σ_{scat}, cross-sections in terms of the frequency depended polarisability $\alpha(\omega)$:

$$\sigma_{abs} = \frac{k_0}{\varepsilon_0}\mathrm{Im}\{\alpha(\omega)\}; \quad \sigma_{scat} = \frac{k^4}{6\pi\varepsilon_0^2}|\alpha(\omega)|^2 \tag{5.49}$$

Therefore, the total extinction cross-section, $\sigma_{ext} = \sigma_{abs} + \sigma_{scat}$, should be considered for metallic particles.

We use this model to calculate the plasmonic properties of metallic particles using parameters tabulated in [99] which produce a good fit to the experimental data of [96] in the range of $\lambda = 200 - 1000$ nm. Figure 5.9 shows an example of calculated optical properties of a silver nano-particle immersed in water with radius 20 nm for a wavelength range $\lambda = 200 - 500$ nm. It is apparent that there is a change of sign in the $\mathrm{Re}\{\alpha\}$ around the plasmon resonance region, and hence repulsive or attractive optical gradient forces for blue- or red-detuned laser frequencies respectively [100]. The peaks at $\lambda = 408$ nm for the scattering and absorbing cross-sections are due to the resonance feature of the imaginary part of the polarisability.

We can now write the optical forces around the nano-fibre in terms of the polarisabilty α and the extinction cross-section σ_{ext}. The gradient force

$$\bar{F}_{grad} = -\frac{1}{4}\mathrm{Re}\{\alpha\}\nabla|E|^2 \tag{5.50}$$

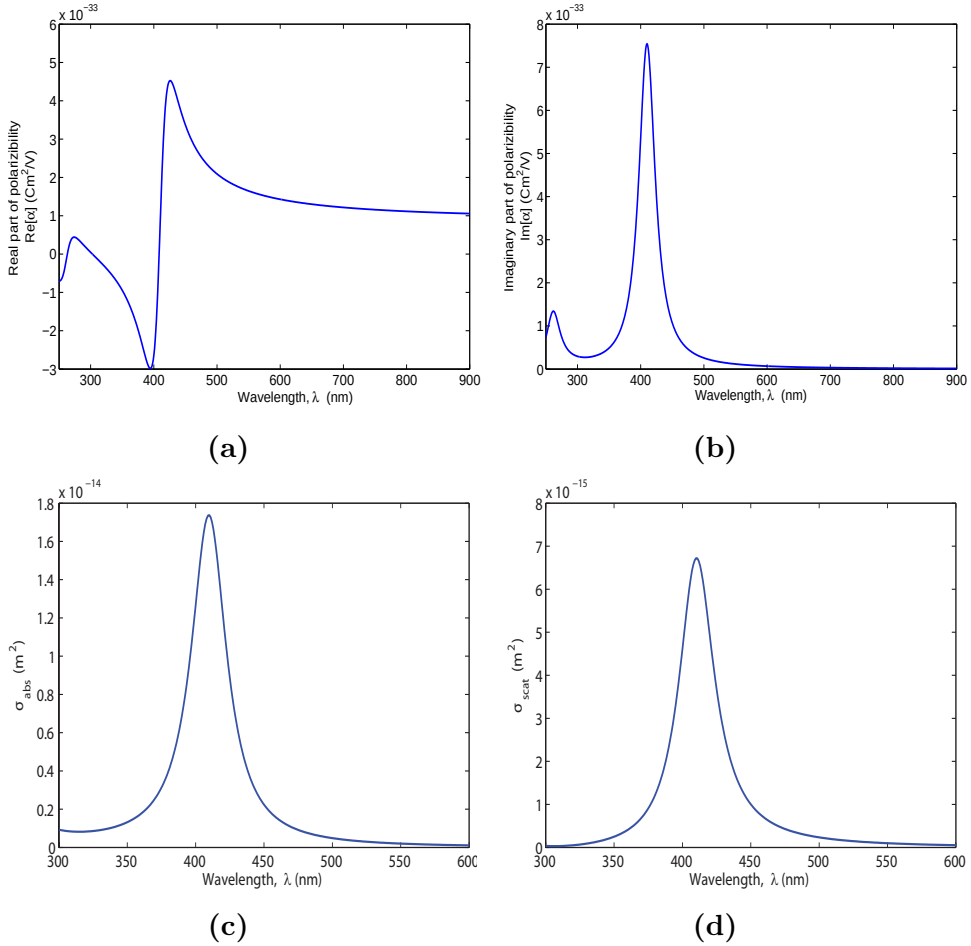

Figure 5.9: Optical properties of silver nano-particle with radius 20 nm calculated with the Lorentz-Drude model. (a) real part of the polarisability, Re[α]; (b) imaginary part of the polarisability, Im[α]; (c) absorption cross-section, σ_{abs}; (d) scattering cross-section, σ_{scat}.

that acts in the direction of the gradient of the intensity in the beam, the scattering force

$$\bar{F}_{scat} = \frac{\sigma_{ext}}{c}\langle \bar{S} \rangle \tag{5.51}$$

that acts in the direction of the time-averaged Poynting vector, and the spin curl force

$$\bar{F}_{spin} = c\ \sigma_{ext}(\nabla \times \langle \bar{L}_s \rangle), \tag{5.52}$$

which acts in the plane transverse to the direction of propagation. Figure 5.10 shows the components of the latter for the case of the circularly polarised HE_{11} mode guided in a fibre with radius $\rho = 500$ nm immersed in water. The force is acting on a silver nano-particle with radius $a = 20$ nm. The radial force is zero because it is a guided wave. The other forces are expected to propel a particle along (z) and around (ϕ) the fibre.

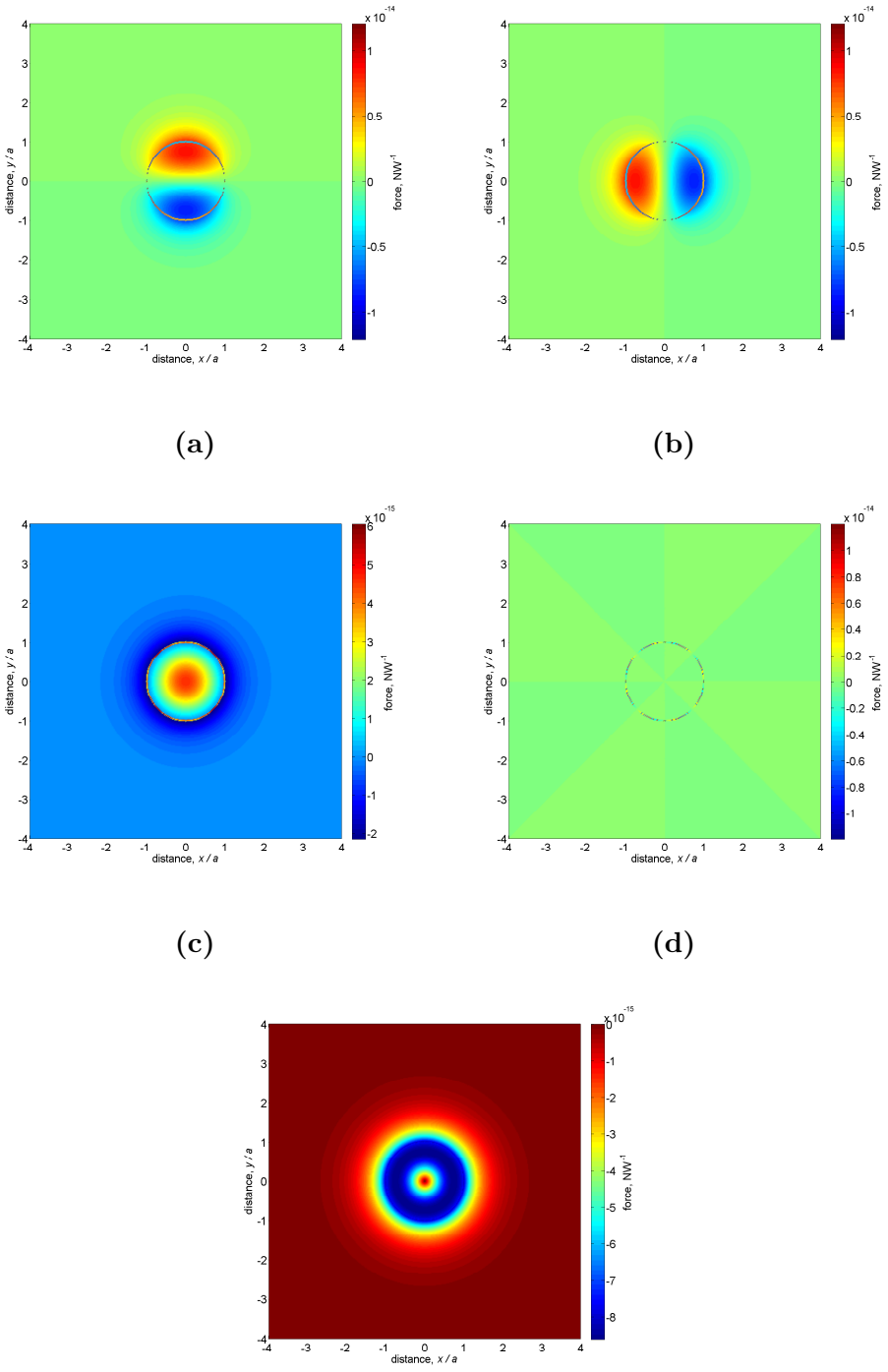

Figure 5.10: Components of the spin curl force acting on a 20 nm radius silver particle in circularly polarised HE_{11} mode guided in a tapered fibre of radius $\rho = 500$ nm and $\lambda = 1064$ nm. (a) x-component; (b) y-component; (c) z-component; (d) radial component; (e) ϕ-component.

5.5 Optical Manipulation of Metallic Nano-particles on Tapered Optical Fibres

This section deals with optical manipulation of metallic (silver and gold) nano-particles around the tapered region of a fibre. Metallic particles have unique optical properties due to the plasmon resonance in their scattering spectrum [101]. The optical forces can be enhanced by the proximity of the laser wavelength to such resonance in the particle. It has been demonstrated that such enhancement was utilised to achieve stable trapping in single-beam optical tweezers [102, 103] which might otherwise be difficult due to the volume scaling of the optical gradient forces for such small particles [104]. Recently good agreement between experimental results and theoretical calculations of trapping forces has been demonstrated for single metallic particles [105, 106] and nano-particle aggregates [107].

Optical manipulation of metallic nano-particles using the evanescent field of a channel waveguide fabricated by ion-exchange technique [108] has been demonstrated. In addition the enhancement of the optical forces using the surface plasmon of a thin gold thin film was used to manipulate both polystyrene [109] and gold particles [110].

The relatively narrow plasmon resonance line-shape of silver leads to a region on the blue-detuned side of the resonance where the real part of the polarisability of the nano-particle can be negative. As mentioned this causes the optical gradient force to be repulsive, and can be exploited to induce particle repulsion from a surface [111]. This is analogous to that used in the gravito-optical surface trap for ultra-cold atoms [112].

When using two counter-propagating laser beams, one which is red-detuned from the plasmon resonance and one that is blue-detuned, then the competition of the attractive and repulsive forces can be utilised as an extra degree of control over the optical trapping. A bi-chromatic trap for ultra-cold atoms in the evanescent field of a tapered fibre has been demonstrated [85].

5.5.1 Silver Nano-particles

Here we present calculations for the interaction energies of red- and blue-detuned wavelengths from the plasmon resonance of a silver particle with 20 nm radius in water at $\lambda_p = 408.3$ nm for different polarisation configurations. Figure 5.11 shows the extinction curve for silver particles of this size under

these conditions.

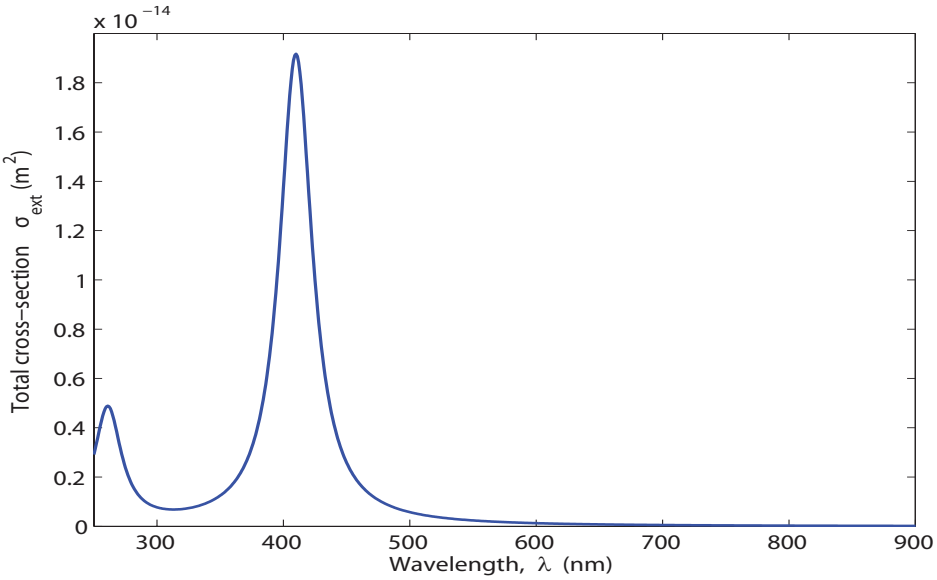

Figure 5.11: Total cross-section $\sigma_{ext} = \sigma_{scat} + \sigma_{abs}$ for silver as a function of wavelength.

5.5.1.1 Lin ∥ Lin Configuration

The first case we consider is that of two counter-propagating HE_{11} modes, red- and blue- detuned with respect to the plasmon resonance with parallel linear polarizations. The wavelengths chosen are those of commercially available diode laser systems, $\lambda_R = 457$ nm and $\lambda_B = 405$ nm. Due to the width of the plasmon resonance the typical difference in frequency between the two laser modes is sufficiently large so that any effects due to mode beating can be neglected and the forces arising from the two modes simply added [113]. The fibre radius is 150 nm, and the silver nano-particle has a radius of 20 nm (small enough to be treated as a Rayleigh particle).

Figure 5.12 shows the dipole interaction energies for red- and blue- detuned laser wavelengths. The interaction energies are plotted in terms of k_BT (k_B is the Boltzmann's constant and T a temperature of 293 K) and are normalised per unit power contained in the mode both inside and outside the fibre.

The intensity of the blue-detuned beam is scaled such that the energy is zero at the edge of the fibre. The shorter decay length of the blue-detuned evanescent field creates a potential barrier around the fibre.

Two potential energy minima exist where nano-particles may localise. For these parameters λ_B is close to the peak of the cross section, so it is expected that the force arising from the imbalance of the radiation pressure (10s of pN

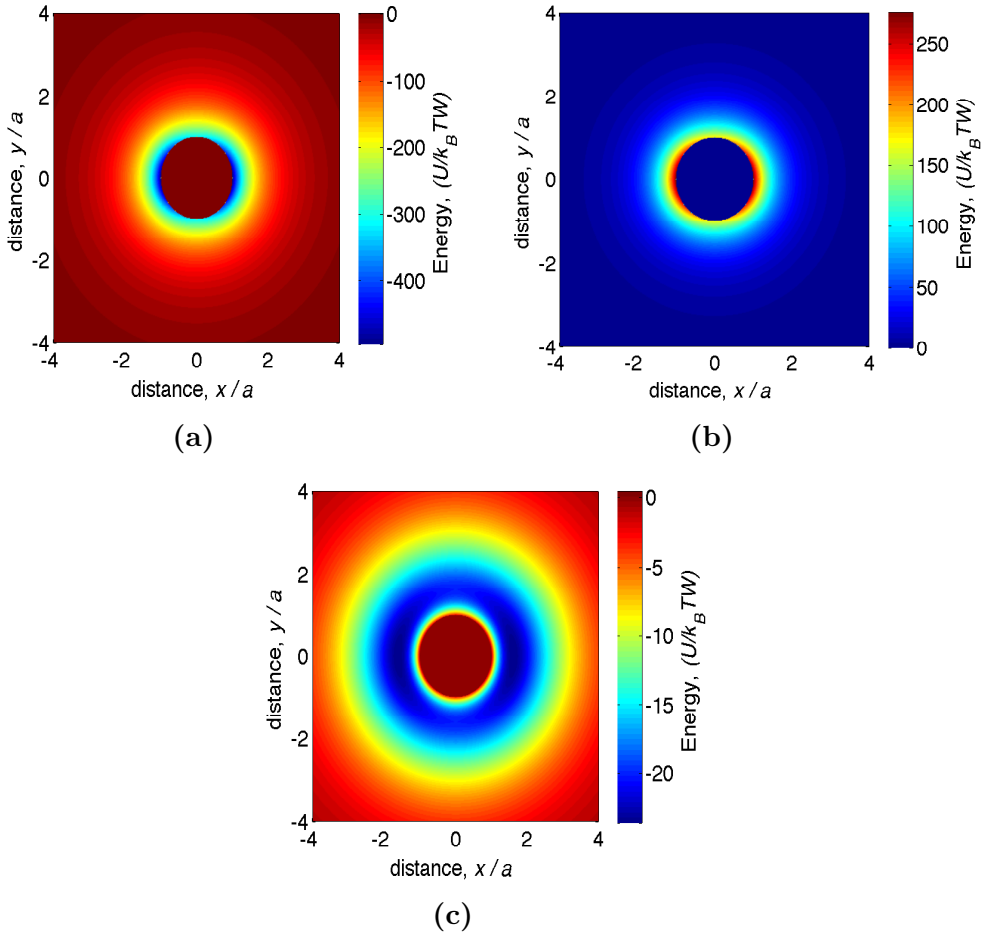

Figure 5.12: Normalised dipole interaction energies for red- and blue- detuned laser beams with parallel linear polarisations.(a) $\lambda_R = 457$ nm $> \lambda_\mathrm{p}$; (b) $\lambda_B = 405$ nm $< \lambda_\mathrm{p}$; (c) Total bi-chromatic interaction energy.

/ W) will drive the nano-particles along the fibre. Forces and energies scale linearly with power, so the values stated here are normalized for 1 W of total power in the mode. Stable trapping could be achieved by balancing radiation pressure with pairs of counter-propagating beams [21] which will also modulate the intensity (and hence the optical dipole potential) along the length of the fibre providing an additional degree of localisation [114].

For plasmonic nano-particles, the magnitude of the propelling force is maximum when the laser is tuned to the plasmon resonance, where the cross-sections are $\sigma_{abs} = 1.72 \times 10^{-14}$ m^2 and $\sigma_{scat} = 6.58 \times 10^{-15}$m^2, and the maximum propelling force adjacent to the fibre is $F_z = 507$ pN W^{-1}, decreasing to $F_z = 84$ pN W^{-1} at a distance from the fibre equal to the fibre radius (these forces are also normalised per unit power in the mode). At this distance, approximately 90% of the force arises from the radiation pressure, and the remaining 10% from the curl of the spin density. The resulting propaga-

tion speed of the particle along the fibre is estimated from the Stokes drag on a sphere corrected for the presence of a cylindrical boundary [115] to be $v_z = 224$ mm s^{-1} W^{-1}.

The net scattering force for the parameters used here is found to be 119 pN W^{-1} at the minimum of the dipole potential. Nano-particles would be driven by this force at an estimated speed of $v_z = 307$ mm s^{-1} W^{-1} in the direction of propagation of the blue-detuned beam.

We also consider evanescent field penetration depth dependency on laser wavelength. Figure 5.13 shows the normalised interaction potential in the predominant polarisation direction for different wavelengths. It can be seen that further detuning to the red side of the plasmon resonance the evanescent field penetrates further into the surrounding medium and the potential well becomes broader and shallower. However as we move further to the blue side of the plasmon resonance the effect is the opposite.

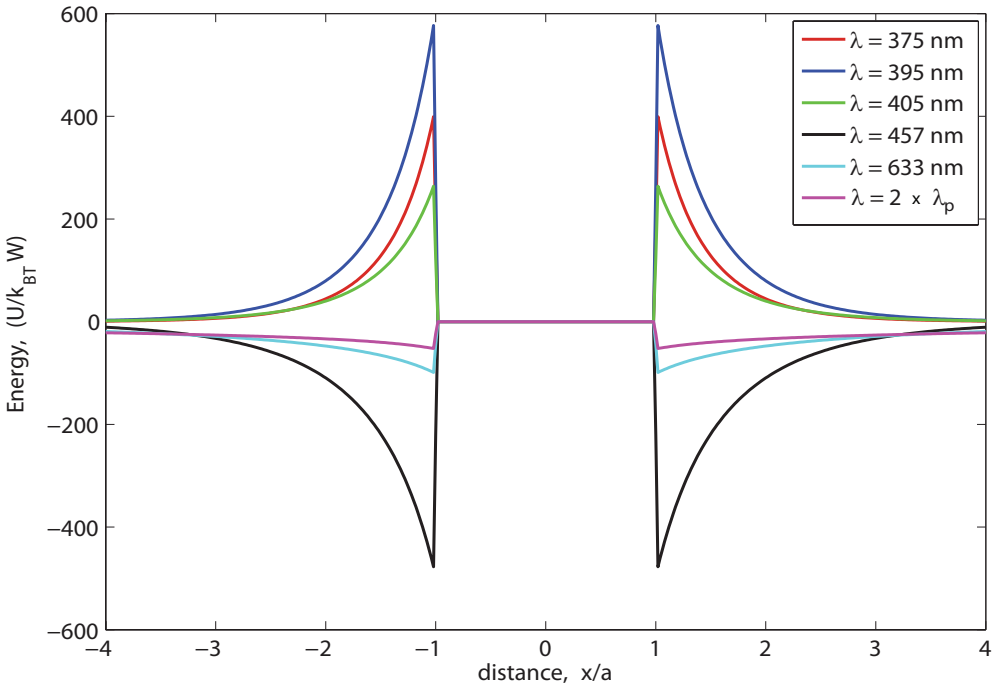

Figure 5.13: Dipole interaction energy for different wavelengths around silver resonance.

5.5.1.2 Lin ⊥ Lin Configuration

Next we consider two counter-propagating HE_{11} modes, red- and blue- detuned with respect to the plasmon resonance (same wavelengths as previous case) with orthogonal linear polarizations.

In Figure 5.14 we observe two shallow potential minima that are found along the direction of polarization of the red-detuned beam (x-direction). The amplitude of blue-detuned evanescent field is smaller in this direction as here its polarization is parallel to the fibre-water interface. Instead the intense blue-detuned evanescent field in the y-direction provides a strong barrier to azimuthal motion.

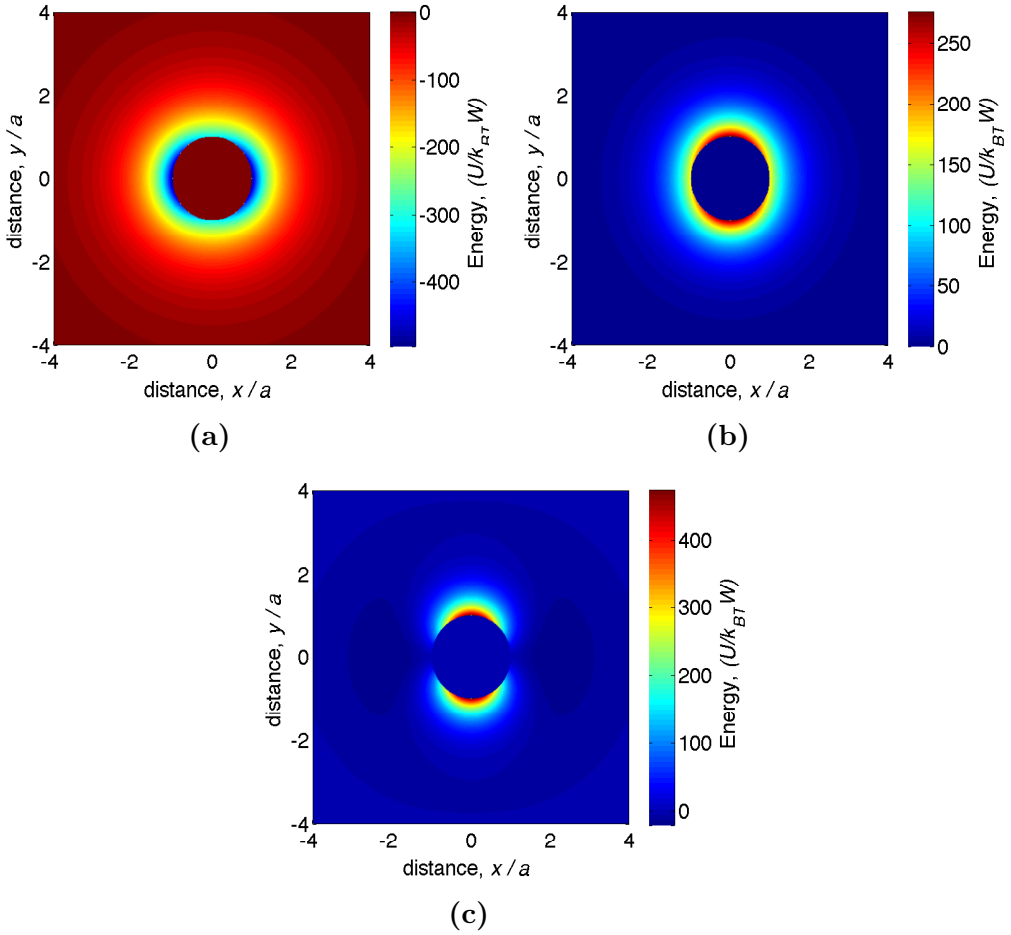

Figure 5.14: Normalised dipole interaction energies for red- and blue- detuned laser beams with orthogonal linear polarisations.(a) $\lambda_R = 457$ nm $> \lambda_p$; (b) $\lambda_B = 405$ nm $< \lambda_p$; (c) Total bi-chromatic interaction energy.

5.5.1.3 $\sigma - \sigma$ Configuration

If both beams have a circular polarization the net potential has azimuthal symmetry and particles are not localized at one point. Indeed, due to the presence of a non-zero azimuthal component of the Poynting vector we expect particles to be driven in a helical trajectory around and along the fibre. Figure 5.15 shows the dipole interaction energies for red- and blue- detuned laser wavelengths.

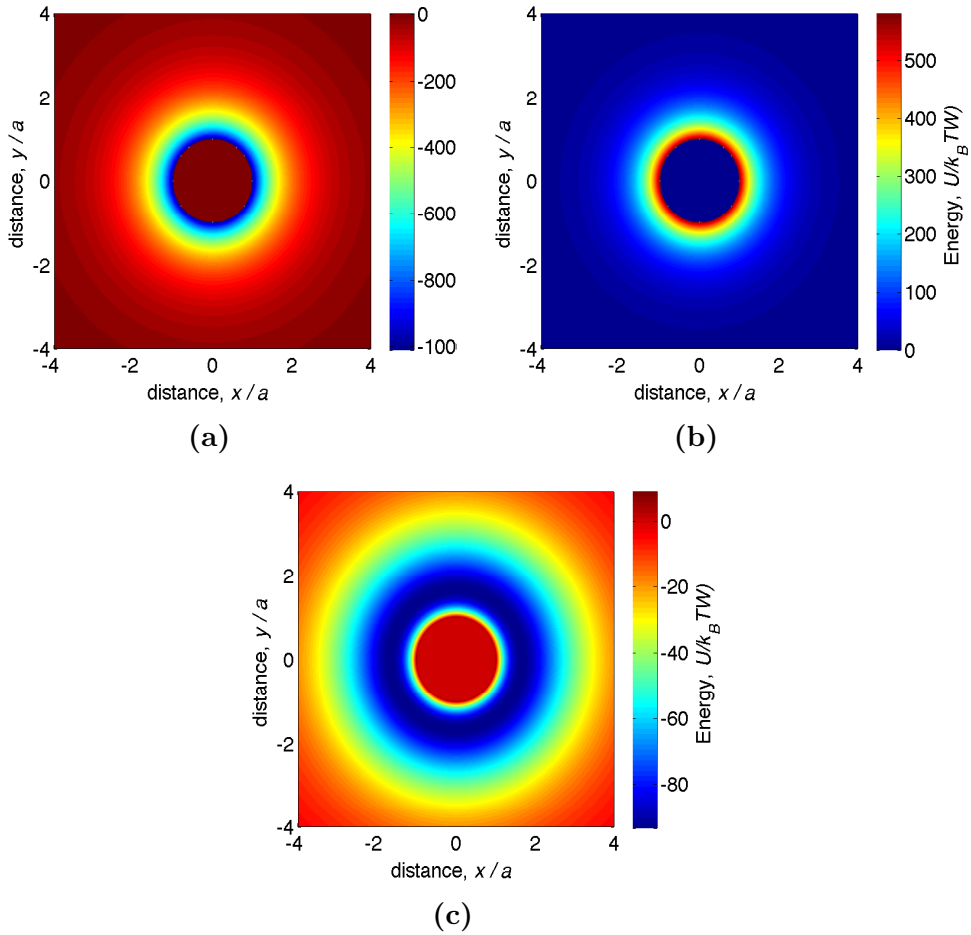

Figure 5.15: Normalised dipole interaction energies for red- and blue- detuned laser beams with circular polarisations. (a) $\lambda_R = 457$ nm $> \lambda_p$; (b) $\lambda_B = 405$ nm $< \lambda_p$; (c) Total bi-chromatic interaction energy.

For this case, the net axial component of the force (normalised) is $F_z = 57$ pN W^{-1} and the azimuthal component $F_\phi = 10$ pN W^{-1} at the minimum of the dipole potential. From this we estimate the components of velocity of $v_z = 151$ mm s^{-1}W^{-1} and $v_\phi = 26$ mm s^{-1}W^{-1}. The magnitude of the transverse force depends on the relative senses of circular polarization of the two beams and determines the pitch of the helical path. For parameters similar to the above calculations we find a pitch of around 10 μm.

5.5.2 Gold Nano-particles

Next, we consider the optical trapping of gold nano-particles in the vicinity of a tapered fibre. The calculations here are made for the same fibre parameters and particle diameter as above. Figure 5.16 shows the optical properties of a gold particle with radius of 20 nm immersed in water. The real part of the polarisability here differs from that of silver in the sense that there is no change

in sign for the whole wavelength range. This implies that the gradient force is always attractive and therefore red- and blue- detuned counter-propagating beams from the plasmon resonance do not provide the same results as in the case of silver particles. However monochromatic trapping can be achieved where nano-particles are propelled along the fibre.

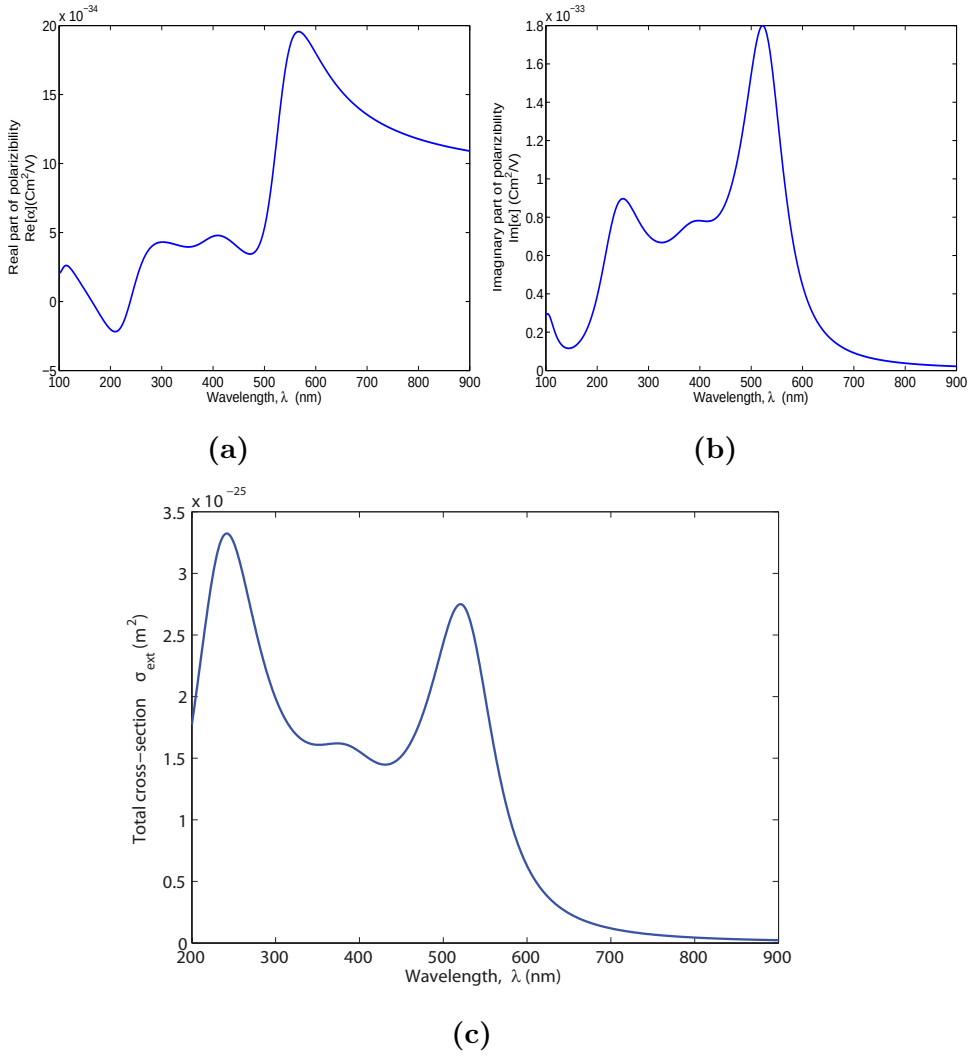

Figure 5.16: Optical properties of gold nano-particle with radius 20 nm calculated with the Lorentz-Drude model. (a) real part of the polarisability, Re$\{\alpha\}$; (b) imaginary part of the polarisability, Im$\{\alpha\}$; (c) Total cross-section σ_{ext}.

We observe two resonances in the extinction cross-section plot. The peaks at the short wavelength are the inter-band transition. Here we consider wavelengths around the intra-band transition, $\lambda_p = 520$ nm, since the first resonance is too far into the UV to be useful (laser sources not available and glass does not transmit in UV).

5.5.2.1 Linear Polarisation

We consider two different laser wavelengths (one blue-detuned and one red-detuned from the gold plasmon resonance) for particle propulsion along a tapered fibre. Figure 5.17 shows the dipole interaction energies for the two cases.

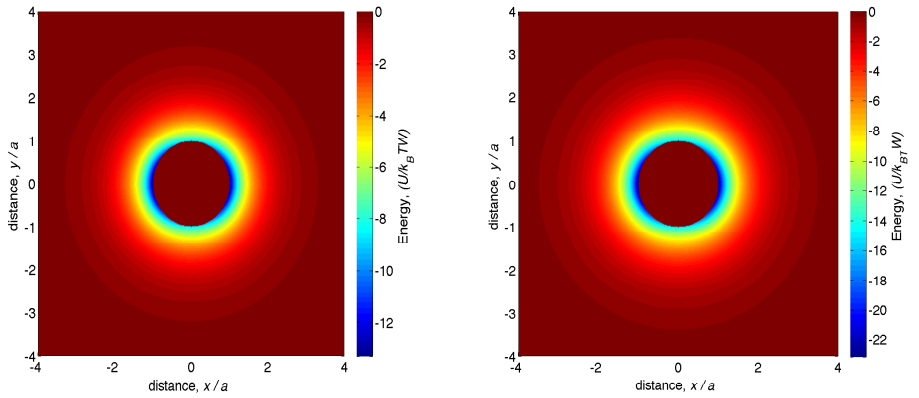

(a) **(b)**

Figure 5.17: Normalised dipole interaction energies for red- and blue- detuned laser beams with linear polarisations. (a) $\lambda_B = 515$ nm $< \lambda_\mathrm{p}$; (b) $\lambda_R = 532$ nm $> \lambda_\mathrm{p}$.

For this configuration the net axial force is $F_z^{(R)} = 3.33$ pN W^{-1} and $F_z^{(B)} = 3.67$ pN W^{-1} at $d = \rho$ for $\lambda_R = 532$ nm and $\lambda_B = 515$ nm respectively. The resulting propulsion velocities $v_z^{(R)} = 8$ mm s^{-1} W^{-1} and $v_z^{(B)} = 10$ mm s^{-1} W^{-1}.

Figure 5.18 presents the dipole interaction energies across the x-direction and the penetration depth Λ of the evanescent field for different wavelengths. It is apparent that the penetration depth increases with wavelength.

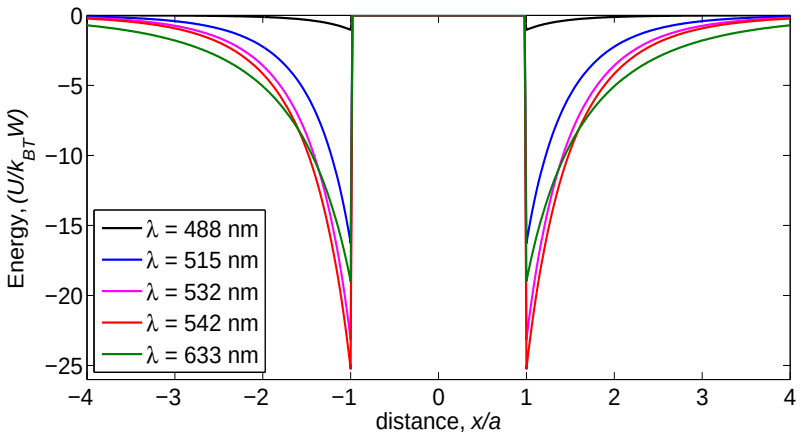

(a)

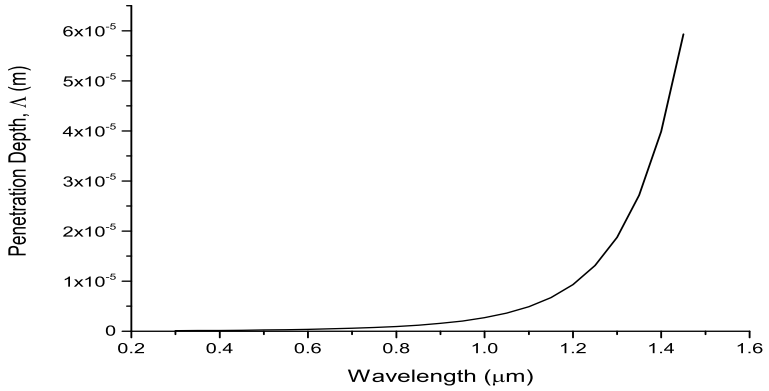

(b)

Figure 5.18: (a) Dipole interaction energy for different wavelengths around gold resonance; (b) Evanescent field penetration depth Λ vs wavelength.

5.5.2.2 Circular Polarisation

The same wavelength parameters are now considered in a circular polarised configuration. Figure 5.19 shows the interaction energies for the two cases.

Similarly we calculate the axial and azimuthal components of the forces. For the blue-detuned wavelength the axial force component at $d = \rho$ is calculated to be $F_z^{(B)} = 2.00$ pN W^{-1} and for the red-detuned $F_z^{(B)} = 1.92$ pN W^{-1}. The resulting axial velocity components of $v_z^{(B)} = 5.32$ mm s^{-1} W^{-1} and $v_z^{(R)} = 5.11$ mm s^{-1} W^{-1}. The azimuthal force components are $F_\phi^{(B)} = 0.44$ pN W^{-1}and $F_\phi^{(R)} = 0.62$ pN W^{-1}. From this the estimated velocity components are $v_\phi^{(B)} = 1.17$ mm s^{-1} W^{-1} and $v_\phi^{(R)} = 1.65$ mm s^{-1} W^{-1}.

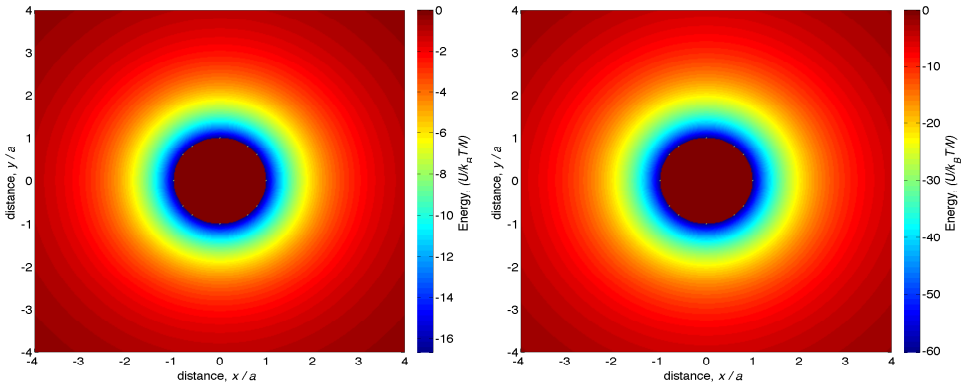

(a) **(b)**

Figure 5.19: Normalised dipole interaction energies for red- and blue- detuned laser beams with circular polarisations. (a) $\lambda_B = 515$ nm $< \lambda_p$; (b) $\lambda_R = 532$ nm $> \lambda_p$.

5.5.3 Particle Sorting

It is implied that the sensitivity of metallic nano-particles to the wavelength of guided light in a nano-fibre can lead to particle sorting applications. Here we present calculations based on previous discussions in this chapter suggesting methods for sorting gold and silver nano-particles. We study the case where a gold and a silver nano-particle of the same radius ($a = 20$ nm) are in the vicinity of the evanescent field generated near the surface of tapered fibre with radius $\rho = 250$ nm, immersed in water. The wavelength chosen here is $\lambda = 405$ nm which is blue-detuned from silver's resonance. The calculations were made for the the quasi-linearly (x-) polarised fundamental mode HE_{11}. Figure 5.20 shows the normalised interaction energies for both materials. We can clearly see that the gold particle is attracted to the surface of the fibre whereas the silver is repulsed.

If the guided wavelength is chosen to be on the red-detuned side of silver's plasmon resonance then both particles will be attracted to the fibre. Sorting in this case can be achieved by comparing the propelling velocities of the particles along the fibre axis. Figure 5.21 shows the distance along the fibre as a function of time (particles are a distance $d = \rho$ away from the fibre surface) for both materials. The parameters here are kept the same except the wavelength which it was chosen to be $\lambda = 457$ nm. It is evident that the silver particle will be propelled much faster than the gold one as the guided wavelength is closer to the resonance of silver, hence the axial scattering force is greater for this material.

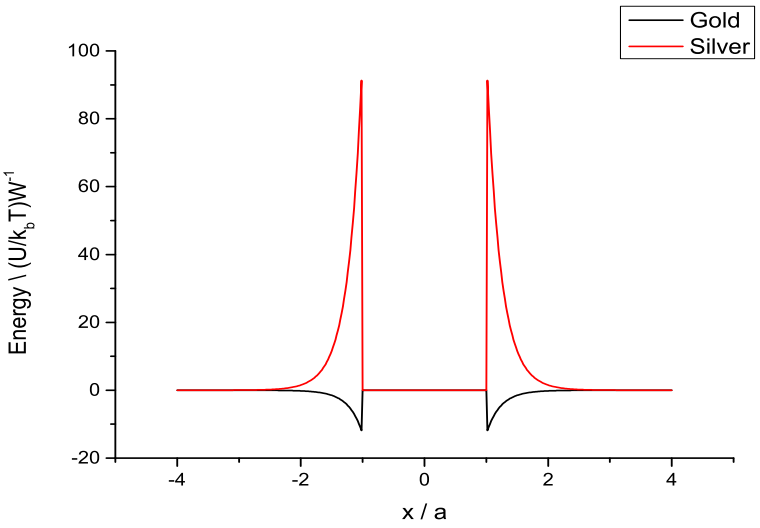

Figure 5.20: Calculations on particle sorting: Normalised interaction energies for both gold and silver nano-particles with radius $a = 20$ nm at a distance $d = \rho$ away from the fibre surface. This case is for the quasi-linearly (x-) polarised fundamental mode HE_{11} ($\lambda = 405$ nm) guided in fibre with radius $\rho = 250$ nm and immersed in water.

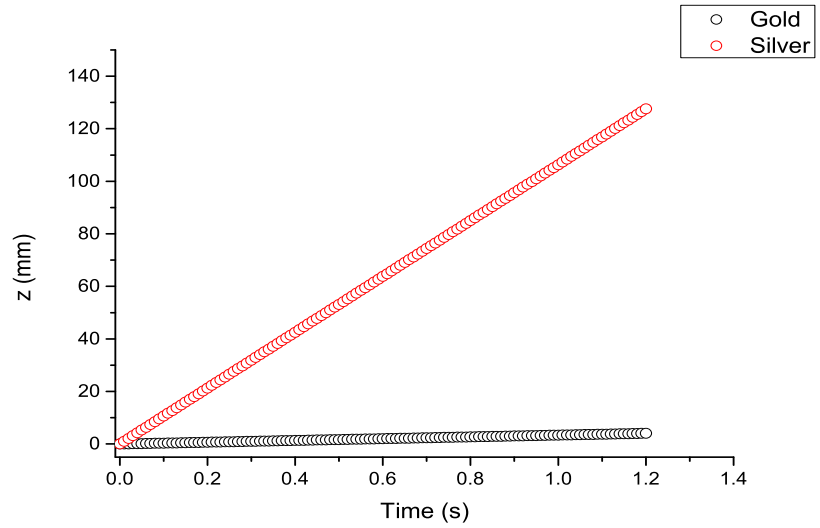

Figure 5.21: Calculations on particle sorting: Propelling distance along the fibre as a function of time for both gold and silver nano-particles with radius $a = 20$ nm at a distance $d = \rho$ away from the fibre surface. This case is for the quasi-linearly (x-) polarised fundamental mode HE_{11} ($\lambda = 457$ nm) guided in fibre with radius $\rho = 250$ nm and immersed in water.

Both these results suggest that particle sorting is possible when the wavelength of the guided mode is chosen carefully.

5.6 Outlook

We have shown how the electric field distribution around a tapered fibre can be calculated by using the exact solution of Maxwell's equations in a cylindrical symmetric geometry. In addition, numerical calculations of the field distributions inside and outside a tapered fibre have been made. It has been shown that the local polarisation has a strong dependence on the fibre parameters: diameter and the refractive index. The cases of quasi-linear and circular polarised fundamental mode HE_{11} have been studied.

Furthermore, we have considered the optical forces originating from the evanescent field of a tapered fibre. Namely expressions for the gradient, scattering and spin curl forces have been presented. Additionally, we have used the Lorentz-Drude model to account for the interaction with metallic nanoparticles and derived an expression for the complex polarisability, α. The optical forces were then written in terms of the polarisibility.

Finally, the optical manipulation of metallic (silver and gold) nano-particles around a tapered fibre was discussed. It is suggested that the sensitivity of the nano-particle dynamics to the polarisation and wavelength of the laser fields through the plasmon resonance could make such tapered fibres an effective tool for sorting nano-particles according to property-dependent criteria.

Chapter 6

Tapered Optical Fibre Trap: Method

6.1 Introduction

In this chapter, a detailed description of a low-cost heat-and-pull apparatus (similar to the one described in [116]) used to fabricate tapered optical fibres suitable for optical trapping is provided. The fibre-pulling rig uses a butane torch which heats a small region of a single-mode fibre while it is being pulled. Alternative heating methods suitable for the fabrication of nano-fibres have been suggested and presented by various groups [117, 116, 118].

Additionally, the experimental set-up used for the conduction of experiments using tapered optical fibres as a trapping geometry is described. Similarly to the evanescent wave surface trap, the particle motion along the tapered region of the fibre is analysed using video microscopy. The experimental analysis and results will be discussed in the next chapter.

We also present the fabrication of fused tapered fibre couplers where two fibres are twisted together before being pulled. The coupling of the two different ends as a function of the polarising angle of the input beam is shown.

6.2 Fibre-pulling rig

Tapered optical fibres are fabricated using a heat-and-pull method on a custom-made fibre-pulling rig (Figure 6.1). The fibre-pulling rig consists of two motorised translation stages (8MT167-100 by Standa Ltd) which are controlled by a micro-step driver (8SMC1-USBhF-B2-4 by Standa Ltd). This driver allows the control of the stages within a 1 μm accuracy. V-groove fibre camps were mounted on each of the stages which were used to hold the fibres. An oxy-butane torch was mounted horizontally onto a labjack with its nozzle pointing vertically. The labjack allowed the adjustment of the flame height. In turn, the labjack was positioned on a rail which provided movement of the flame towards or away the fibre. A manually operated translation stage of 1 μm accuracy was mounted vertically. A stage with a circular hole was attached to it. This stage was used to bring glass slides to the fibre once the pulling process was complete. The circular hole in the middle of the stage was to allow the torch nozzle to remain in position thus avoiding breakage during the fibre mounting.

A length of standard single-mode optical fibre (SM-980-5.8-125 from Thorlabs Inc. NJ) has a short section (20 mm) of the protective polymer buffer stripped away to reveal the cladding glass of the wave-guide. This region is then cleaned with isopropyl alcohol to remove any dust. The fibre is held in the V-groove fibre clamps which are mounted on the motorised translation stages. The exposed glass region is heated by the butane gas torch. The oxygen flow of the butane torch can be adjusted to produce a blue flame minimizing the amount of carbon deposited on the tapered region which can affect the penetration depth of the evanescent field. The size of the flame (approx. 2 cm) and the position of the fibre in it, are optimized so that the heat is sufficient to melt the fibre and in parallel avoid breakage during pulling. The fibre is placed directly above the tip of the flame. The stages are driven apart a distance of 20 - 30 mm at speeds of between 0.5 and 1.0 mm s^{-1} using a LabVIEW based code which controls the micro-step driver. When the stages reach their desired destination the flame is removed and the fibre is further stretched by driving the stages in small steps. This ensures that any bending caused by the flame pressure is tightened.

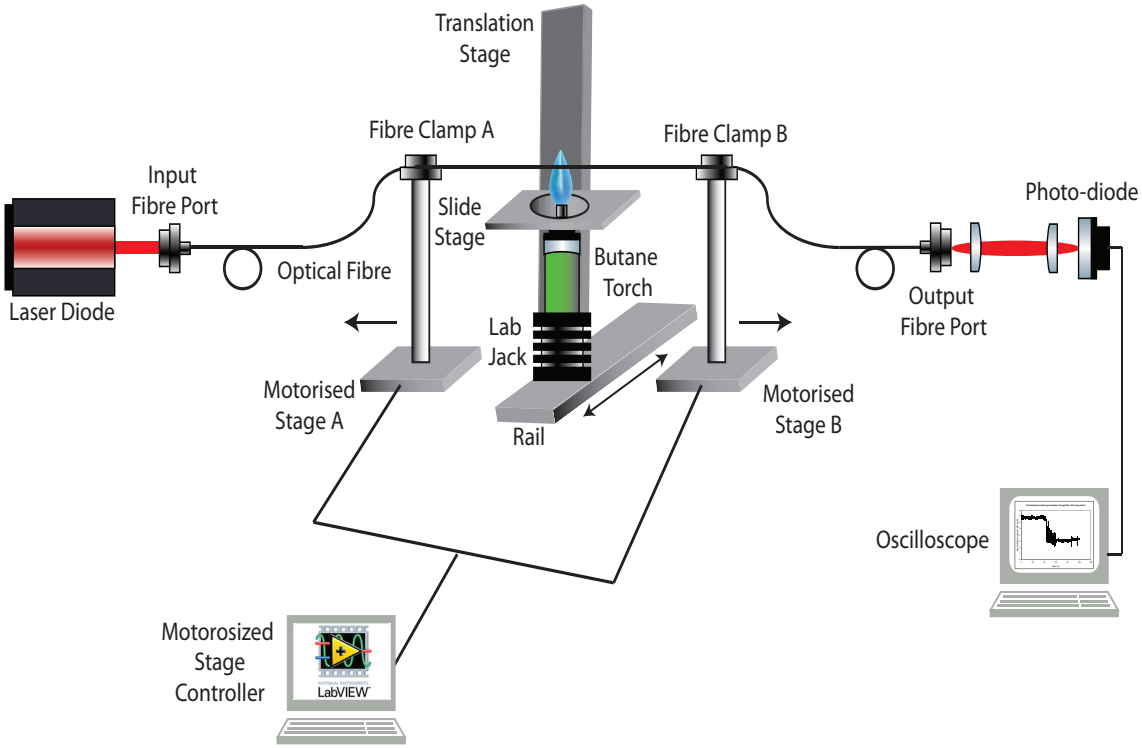

Figure 6.1: Custom made fibre-pulling rig suitable for heat-and-pull fabrication of tapered optical fibres. The apparatus uses a butane torch which heats a small region of a standard optical fibre while it is being pulled by two motorised stages.

The tapering process is monitored by coupling light from a diode laser (wavelength $\lambda_0 = 630$ nm) into the fibre. The transmitted power is measured, as the pulling process occurs, by a photo-diode on one end of the fibre. The photo-diode is connected to a computer running a PicoScope oscilloscope software. A plot of the transmission during a typical tapering process is shown in Figure 6.2. Some features of the pulling process are evident here: at the point labelled 'A' a sudden decrease in the transmitted intensity is observed, corresponding to the core glass material being tapered away leaving a wave-guide made of the remaining cladding glass. Due to its large diameter this wave-guide is multi-mode. As the pulling process continues and the wave-guide diameter is tapered further, beating between the higher modes (due to the different propagation constants) of the wave-guide is observed until they are cut-off, and only the fundamental mode of the wave-guiding structure remains [119]. Eventually on reaching the single mode condition (approximately at the point labelled 'B') no further decrease in transmitted intensity is observed. Transmission of the tapered fibres we produce in this way is less than 100% which is probably due to non adiabaticity of the taper leading to losses in the tapered region [120].

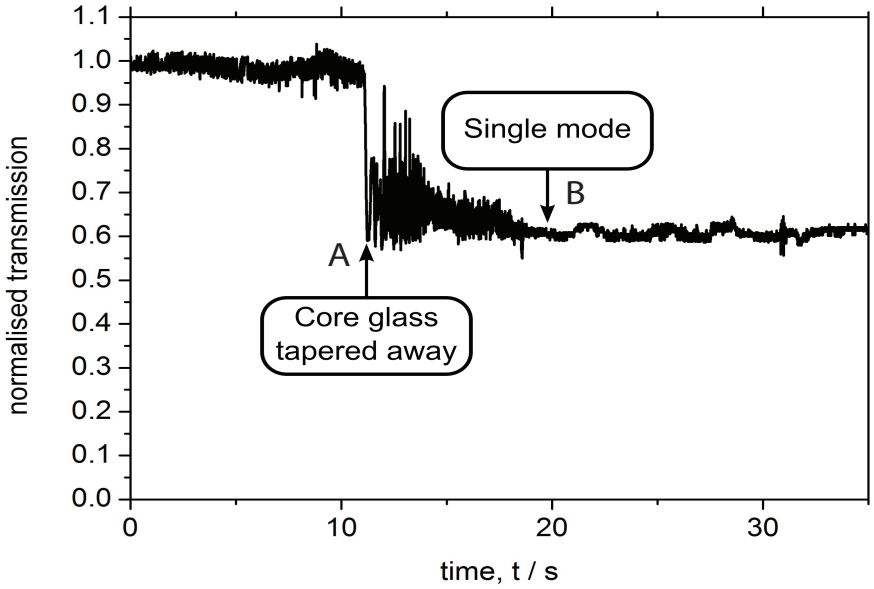

Figure 6.2: Transmission of the optical fibre during the pulling process. At 'A' the core glass has tapered away leaving a (multi-mode) wave-guide made only of the cladding glass. At 'B' the cladding glass waveguide has reached the single mode condition.

The tapered fibre is then mounted on a custom-made microscope slide containing a 300 μm deep groove (Figure 6.3). The fibre was then secured on the glass slide by nail polish. Each end of the tapered fibre was cleaved and inserted into a fibre-to-fibre splice unit to couple in laser light.

This process usually achieves a bi-conical taper that is typically 1 μm in diameter. The diameter of the tapered region is estimated by comparing it to the known sized polystyrene particles.

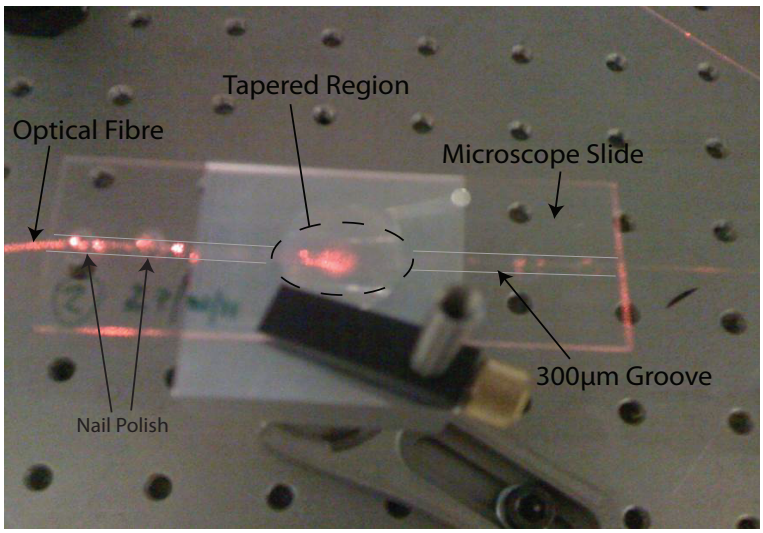

Figure 6.3: Mounted tapered fibre on custom-made slide. This was actually not a very good taper for the experiment as the red laser light was leaking out, however for the purposes of illustration the tapered region of the fibre is well shown.

6.3 Tapered Optical Fibre Trap

The laser source for the optical binding experiment with the tapered fibre is a single-mode Nd:YAG laser (ventus IR 1064 by Laser Quantum) with a maximum output power of 3 W. The output beam is coupled into a length of the same type of optical fibre that is used for making the fibre tapers using a NA = 0.15 fibre port. These fibres are then connected to the tapered fibre by means of a fibre-to-fibre splice. A HeNe laser is initially used for the fibre-to-fibre splice alignment since the scattered light from the splice is easily visible. When alignment is complete the connectorised fibre is connected to the fibre port which couples in the Nd:YAG laser light. This fibre is mounted on a manual fibre polarisation controller (FPC030 from Thorlabs Inc. NJ) which modifies the polarisation of the guided light by utilizing stress-induced birefringence [121].

A few tens of micro-litres of solution containing 2 μm diameter polystyrene micro-spheres suspended in deionized water (with 10% by volume Triton-X-100 to prevent particles sticking to the fibre) is finally added and sealed beneath a cover slip. The slide-mounted tapered fibre is then viewed in an inverted microscope (Zeiss Axiovert 200). A diagram of the optical set-up is shown in Figure 6.4.

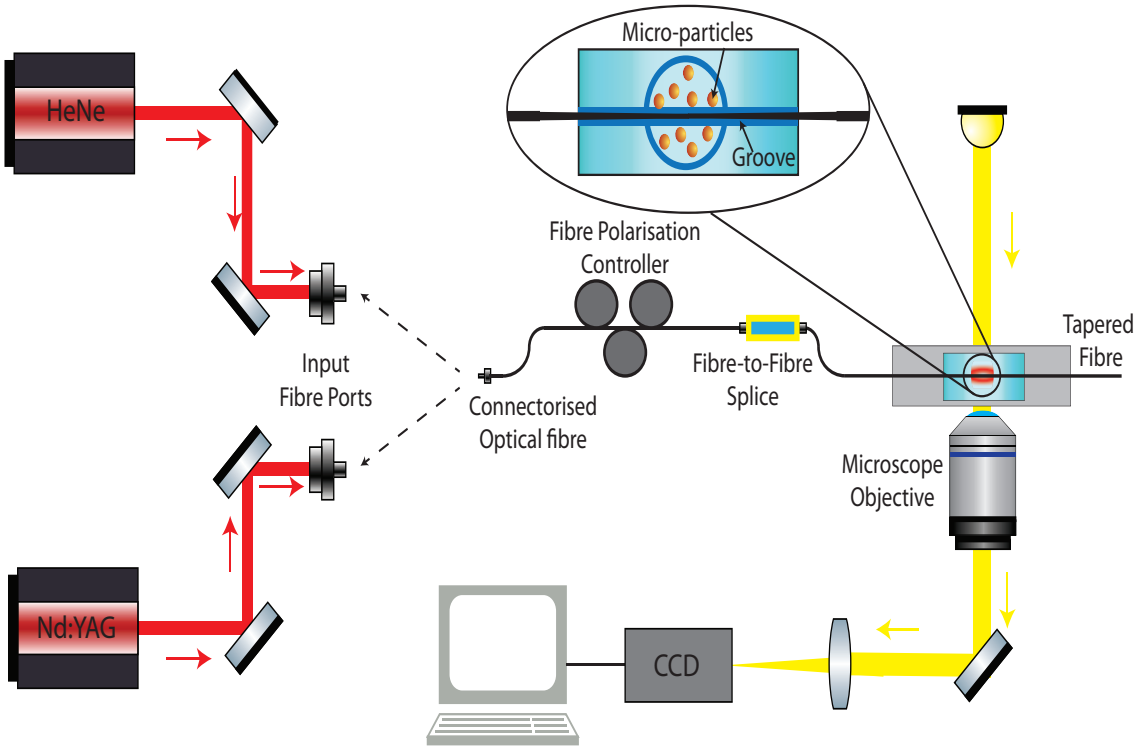

Figure 6.4: Apparatus for observing an evanescent wave particle trap using tapered optical fibres. First, a HeNe laser is used for alignment. Next, light from the Nd:YAG laser is coupled into a tapered optical fibre for trapping experiments. The taper is mounted in an inverted microscope and observed though a objective lens.

In this experiment, particle dynamics is again analysed by video recording and particle tracking as described in Section 3.3.

6.4 Fused Tapered Fibre Couplers

Lastly we present a fused tapered fibre coupler fabricated using the fibre pulling rig similar to [122] and modelled in [123]. Two fibres have a short section of their protective polymer buffer cleaved. The cleaved sections are then twisted together. The two fibres are fused together due to the heating and we obtain a structure as shown in Figure 6.5

We monitor the output at both ends of the two fibres when coupling light to Fibre 'A' via a fibre port. The polarisation angle of the input beam is rotated by a $\lambda/2$ wave-plate. Figure 6.6 shows the intensity output of Fibre 'A', I_A, normalised to the total intensity output, $I_A + I_B$, as a function of the polarisation angle in degrees. It is apparent that light leaks out and into Fibre 'B' as the polarising angle varies. The sinusoidal fit does not oscillate from 1 to 0 meaning that there is always some light in both fibres. This is probably

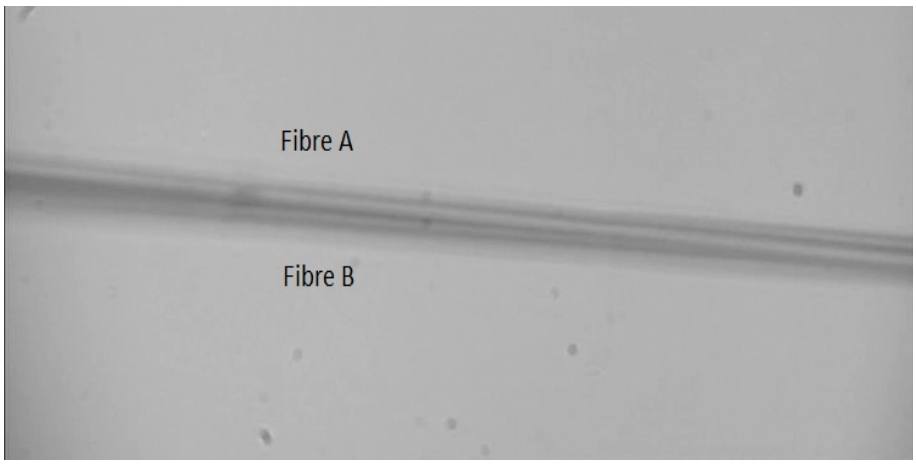

Figure 6.5: Fused twisted tapered fibres. Fibres 'A' and 'B' are twisted together before the pulling process. The two fibres are then fused due to heating.

due to the birefringence introduced to the fibres during the pulling process which can lead to mode-mixing.

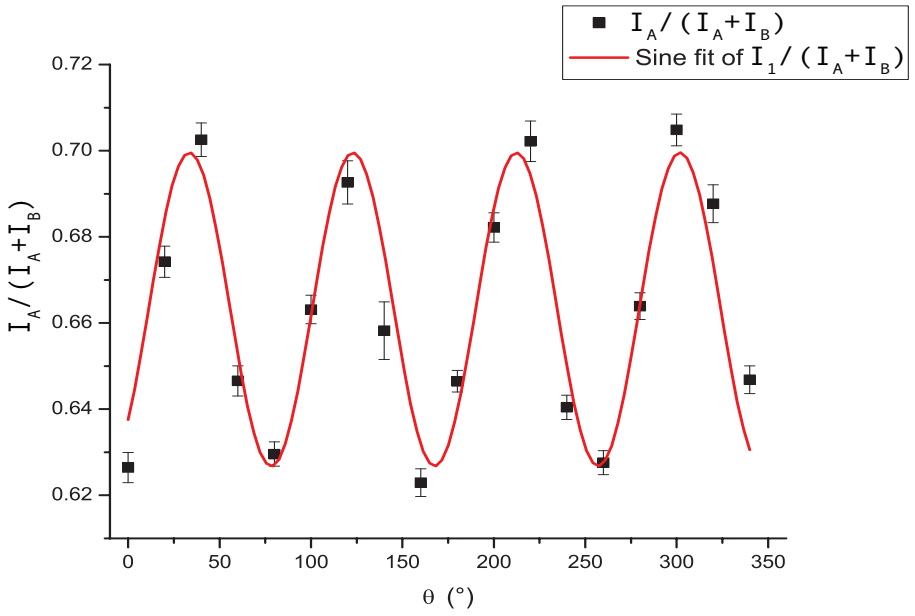

Figure 6.6: Intensity varies with the polarising angle of the input beam. Light is coupled in Fibre 'A' and the output at the ends of Fibre 'A' and Fibre 'B' is monitored. The red curve is a sinusoidal fit on the experimental data.

We anticipate that with further refinements to the tapering process to improve the ratio of power splitting between the outputs, this tapered fused fibre could be used to drive micro-particles to two different locations depending on the polarising angle of the input beam. Even though some preliminary results have been presented here, optimisation of the fabrication method has to be made to achieve adiabatic fibre tapers.

6.5 Outlook

The design and construction of a fibre-pulling rig suitable for fabricating tapered fibres has been described in this chapter. The apparatus uses a butane torch to heat a region of a standard optical fibre while it is being pulled. Meanwhile the apparatus produces tapers that are acceptable for the experiments presented in the following chapter, several changes can be made to optimize its performance. The butane can be replaced by hydrogen to create a more uniform flame reducing the defects on the fibre. Furthermore, the flame could be scanned along the region of the fibre while is being pulled in order to achieve adiabatic fibre tapers. This will eliminate mode mixing which allows selective excitation of fibre modes when used with fibre polarisation controllers.

Moreover, the experimental set-up that is used to produce the results presented next was described in detail. Similarly, optimisation changes can be made specifically to achieve higher coupling efficiency into the taper. More efficient methods (i.e. fusion splicing) than the fibre-to-fibre splice can be used to achieve this.

Chapter 7

Tapered Optical Fibre Trap: Results

7.1 Introduction

This chapter presents the experimental results obtained by using the tapered fibres fabricated with the heat-and-pull method (Section 6.2) to manipulate micro-particles. The tapered fibres obtained usually had a diameter of approximately 1 μm. The laser beams coupled into the fibres have a wavelength of 1064 nm. As shown in Figure 5.2 the only allowed mode for these parameters is the fundamental mode HE_{11}. For these parameters we calculate that the penetration depth is $\Lambda = 0.39$ μm, and approximately 26% of the mode power is carried outside the fibre in the evanescent field.

We have studied the cases for both linear and circular polarisations of the beam for which the propulsion speeds were measured using video microscopy (Section 3.3). Additionally, laser beams are coupled into both ends of the tapered fibre to observe the formation of 1-D chains similar to (Section 4.3).

7.2 Optical Manipulation of Micro-Particles

First, we present results for the quasi-linearly (x-) polarised fundamental HE_{11} mode guided in a tapered fibre of radius of 500 nm. The intensity of the field components around the tapered fibre for this case is shown in Figure 7.1 as calculated by the method described in Section 5.3.

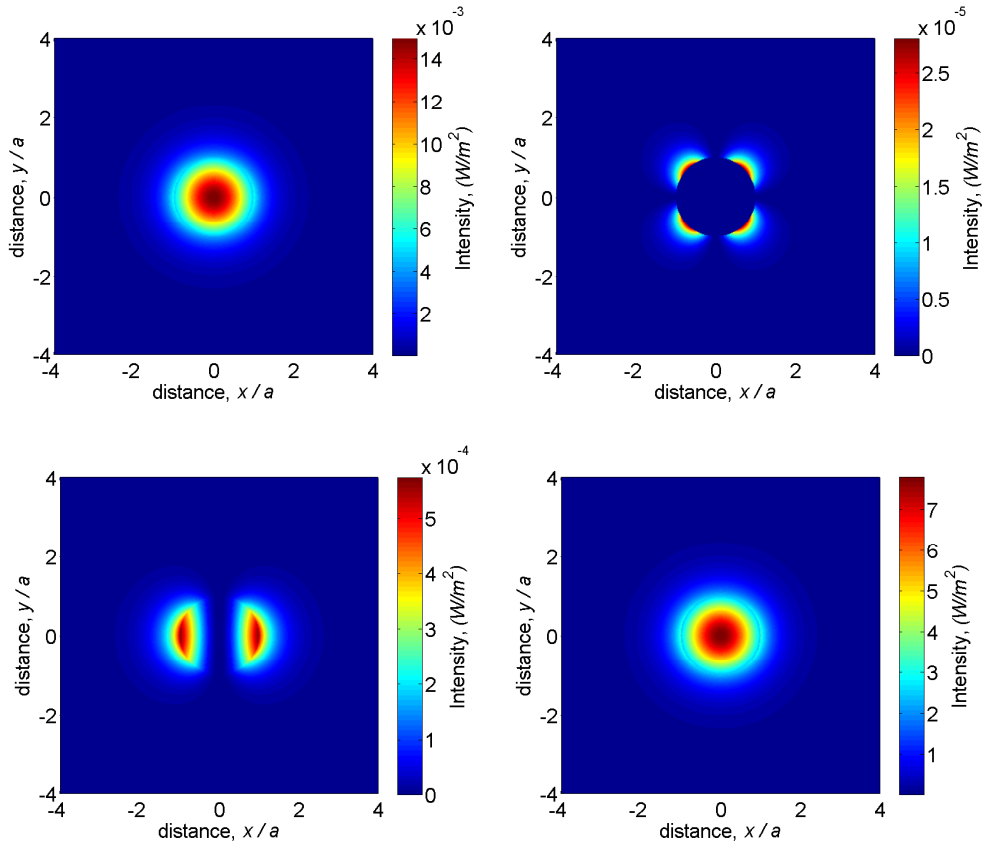

Figure 7.1: Directed fields for the quasi-linearly (x-) polarised fundamental HE_{11} mode in silica fibre with radius 500 nm, wavelength $\lambda = 1.064$ μm. Top left: field in the dominant polarisation direction, x; Top right: field in the orthogonal polarisation direction, y; Bottom left: field in the propagation direction, z; Bottom right: Total field.

When a single mode propagates unidirectionally in the tapered optical fibre, micro-particles are observed to be drawn to the fibre (by the optical gradient force) and propelled along it (by the scattering force) as shown in the sequence of video frames taken at 2 s intervals in Figure 7.2. In this experiment particle dynamics are analysed by video recording and particle tracking (Section 3.3). In this case we track the particles centre of mass as they are pushed along the tapered fibre. Figure 7.3 shows the recorded trajectory of two micro-particles along the tapered fibre. Both particles move along the fibre at a uniform speed of (6.95 ± 0.05) μm s^{-1}.

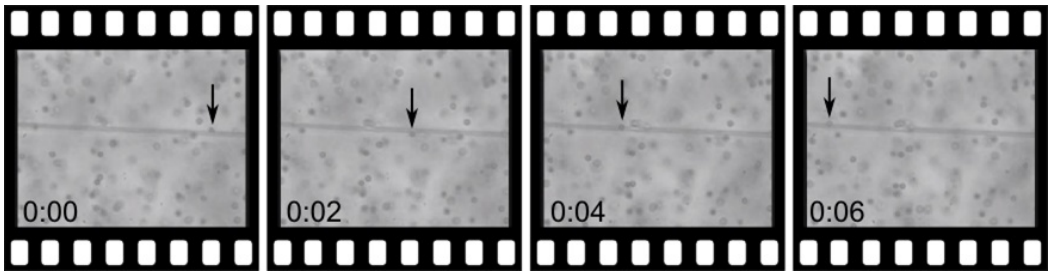

Figure 7.2: Sequence of video frames taken at 2 s intervals of 2 μm polystyrene spheres being propelled along a tapered fibre.

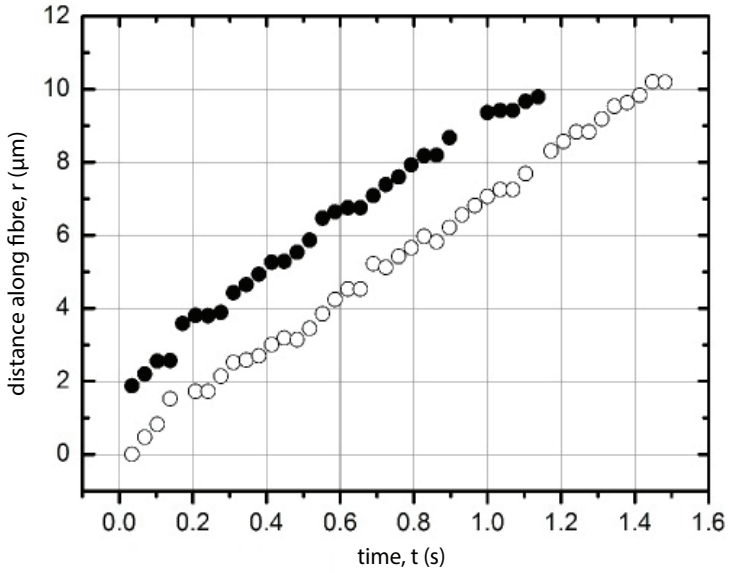

Figure 7.3: The trajectory of two micro-particles along the tapered fibre are shown (filled and open circles). Both particles move along the fibre at a uniform speed of (6.95 ± 0.05) μm s^{-1}.

Figure 7.4 demonstrates what happens to a 2 μm diameter polystyrene particle that reaches the end of a fibre 'half taper', that is, a fibre that has been tapered to breaking point. During time T_1 the particle moves along the fibre at a constant speed of (8.76 ± 0.03) μm s^{-1} before being rapidly ejected from the tip before being brought to rest in a time T_2 by viscous drag. This demonstrates how tapered fibres or half tapers can be used for optical delivery of micro-particles to a targeted region. The particle is confined against the fibre all the way to the tip before being ejected.

7.2.1 Circular Polarisation

Next, we consider the case of the circularly polarised HE_{11} fundamental mode guided in the fibre. The intensity of the field components with the same parameters used in the previous section are shown in Figure 7.5.

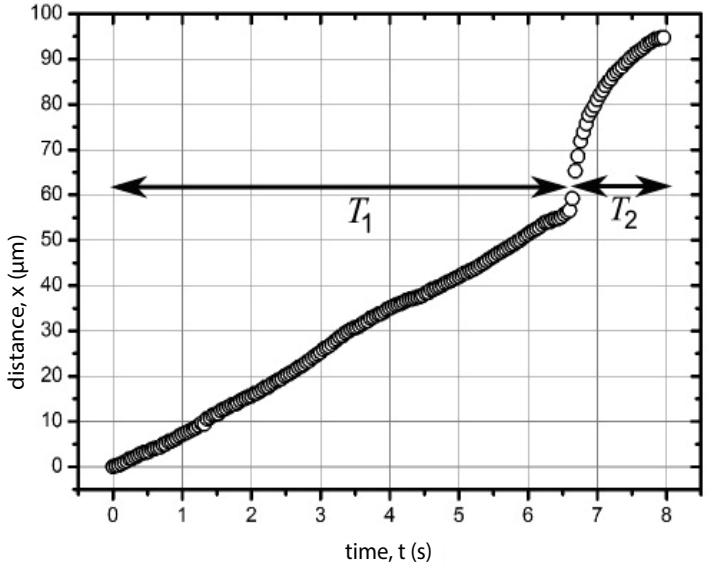

Figure 7.4: Particle shooting: the trajectory of a micro-particle pushed towards the end of a fibre 'half taper'. During he time T_1 the particle moves along the fibre at a constant speed of (8.76 ± 0.03) μm s^{-1} before reaching the end of the fibre and being ejected. During the time T_2 the particle is moving freely through the fluid and eventually brought to rest.

As discussed in Section 5.4 the circularly polarised HE_{11} mode is expected to drive the particles in a helical trajectory along and around the fibre due to the non-zero azimuthal component of the Poynting vector. Figure 7.6 is a sequence of video frames showing the two 2 μm polystyrene spheres following a helical trajectory.

The trajectory of these particles is reconstructed and plotted in Figure 7.7. The measurements uncertainties due to resolution were estimated to be ± 0.25 μm. The polystyrene spheres were used to calibrate the video and to estimate the fibre waist. The trajectories were fitted with a sinusoidal function. The periods of the sinusoidal fits were found to be (26.0 ± 0.7) μm and (26.8 ± 0.2) μm for particle 'A' and particle 'B' respectively. The two periods agree within the stated errors. The z and ϕ velocity components of the two particles were also measured. For particle 'A' $v_z = (5.48 \pm 0.01)$ μm/s and $v_\phi = (0.48 \pm 0.02)$ μm/s and particle 'B' $v_z = (5.49 \pm 0.02)$ μm/s and $v_\phi = (0.46 \pm 0.02)$ μm/s. These values also agree within the stated errors.

This result demonstrates the conversion of spin to angular momentum in optical fibre tapers. It has been shown that this can be observed in high numerical aperture focusing, by scattering of small particles and in paraxial light fields incident on anisotropic media or non-paraxial fields in locally isotropic

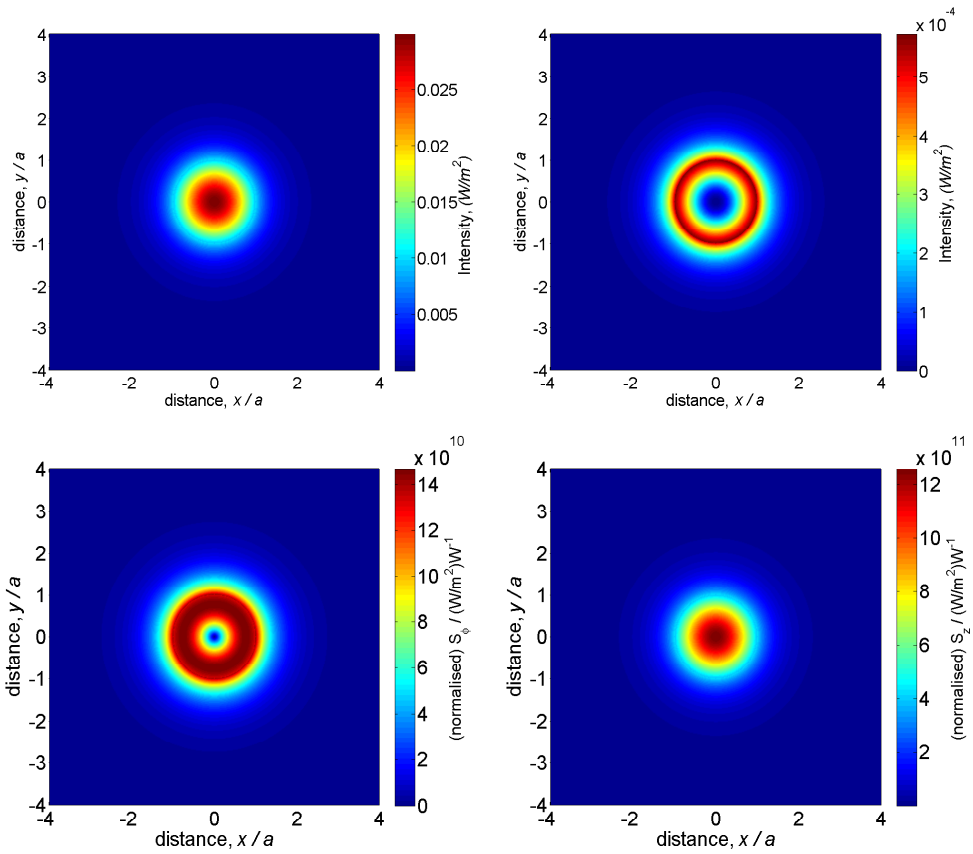

Figure 7.5: Directed fields and Poynting vector magnitudes for the circularly polarised fundamental HE_{11} mode in silica nano-fibre with radius 500 nm, wavelength $\lambda = 1.064$ μm. Top left: transverse component field; Top right: longitudinal component field; Bottom left: azimuthal component of the Poynting vector S_ϕ; Bottom right: longitudinal component of the Poynting vector vector, S_z.

media [124]. Optical fibre are considered to be an intermediated case of the last two.

7.2.2 Two Beam Tapered-Fibre Trap

When laser beams are coupled into both ends of the tapered fibre, chains of micro-particles are observed to form. Qualitatively, two distinct forms of chain-like structure are observed. At places where the radiation pressure from the counter-propagating beams is unequal, strings of particles separated by approximately 2 - 3 particle diameters are pushed along the fibre. The separation between the particles is due to the combination of the attractive optical binding force pulling the particles together and the fluid drag which moves them apart. Oscillations in the trajectory are due to the transverse components of optical momentum from the circularly polarized beam. Frequently the particles in these strings are observed to follow a trajectory that oscillates

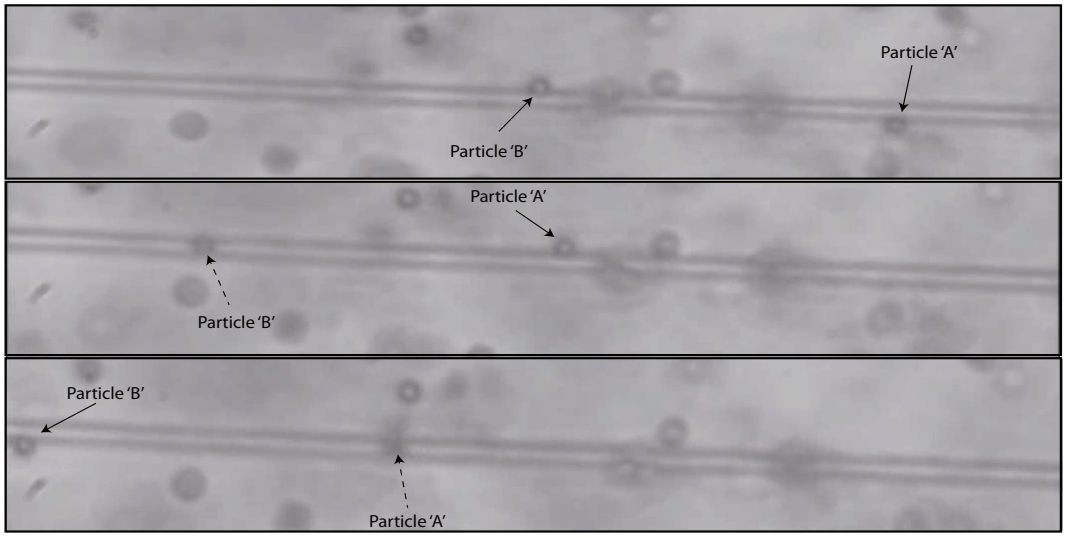

Figure 7.6: Helical trajectory of micro-particles along and around a tapered fibre. The dashed arrows indicate that the particle is behind the fibre away from the camera.

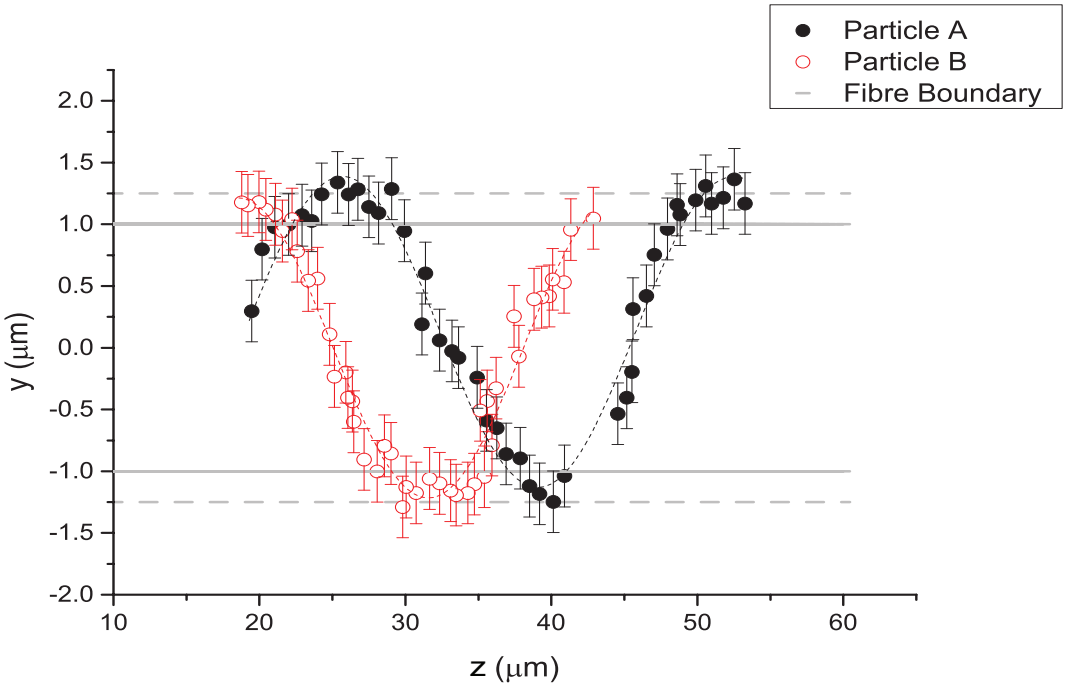

Figure 7.7: Reconstructed helical trajectory of micro-particles along and around a tapered fibre. The dashed lines are sinusoidal fits and the grey lines are the fibre boundaries with their assorted uncertainties.

from one side of the tapered fibre to the other. Where the radiation pressure from the beams is equal or nearly-equal we observe the particles bound into chains similar to those formed in the surface trap described above.

Both behaviours are illustrated in the video frames shown in Figure 7.8. In the first frame 2 μm diameter polystyrene spheres form short, stable optically bound chains on the tapered fibre where the radiation pressure from the counter-propagating beams is (nearly) balanced. In the next frame, more particles are pushed into the trapping region from the right hand side by unbalanced radiation pressure. The particles move at steady speed separated by 2-3 particle diameters and follow a trajectory that coils from one side of the fibre to the other. In the third frame some of the additional particles have been lost and stable chains form again.

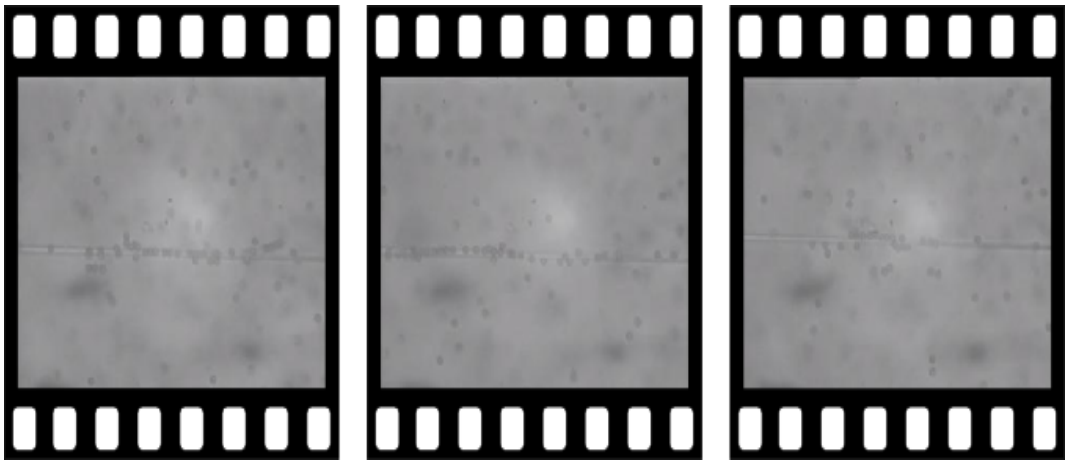

Figure 7.8: Sequence of frames from a film of optical binding and micro-particle chain formation in the evanescent field of a tapered optical fibre. First frame: the radiation pressure from the counter-propagating beams is (nearly) balanced; Second frame: unbalanced radiation pressure and particles follow a trajectory that coils from one side of the fibre to the other; Third frame: stable chains form again.

Optical binding of such structures using this method may lead to the investigation of the different configurations in which the particles can be bound by different mode structures, with potential applications in biophotonics for single molecule detection and trafficking. For example the excitation of whispering gallery modes in the bound micro-particles could be used for the hypersensitive detection of single molecules. Micro-sphere lasers can be used as highly sensitive sensors, achieving a wide range of emission wavelengths [125]. Ordered arrays of such lasers should provide an enhancement of the evanescent field due to constructive interference effects, leading to an increased sensitivity

for particle detection. Additionally, the delivery and transport of particles such as drug capsules or bacteria may be achievable by using similar configurations.

7.3 Outlook

We have presented the analysis of the results obtained on optical manipulation of micro-particles in the vicinity of the tapered region of a single mode fibre. It has been demonstrated that polystyrene micro-particles can be attracted to, and propelled along a fibre. It has been shown that the polarisation of the mode guided in the fibre can control the motion of particles.

In the future the set-up could additionally be extended to incorporate an optical tweezers set-up to characterise the optical potential created by the evanescent wave as described in outlook section of Chapter 3. Even though the polarisation of the beam coupled into the fibre is known, birefringence in the fibre induced during the pulling process may convert the polarisation and allow mode mixing. To draw more precise conclusions on the forces around the fibre, the mode propagating in the tapered region needs to be measured. A method allowing these measurements needs to be developed. Another addition to the experiments is the use of higher order modes in the fibre [126]. To allow the propagation of such modes in the fibres the adiabatic fabrication must be ensured during the pulling process. The use of higher modes will provide an extra degree of control on optical manipulation.

Chapter 8

Conclusion

8.1 Discussion

This thesis has presented the optical manipulation of micro-particles using evanescent fields and the quantitative measurements of trapped particle dynamics using video microscopy. The cases of two trapping geometries have been considered: the first is a surface trap where the evanescent field above a glass prism is formed by the interference of a number of laser beams incident on the prism-water interface; the second uses the evanescent field surrounding a bi-conical tapered optical fibre that has been stretched to produce a waist of sub-micron diameter. The experimental studies of particle structures were complemented by light scattering calculations based on Mie theory to infer how the geometries of the observed particle structures are controlled by the underlying incident and scattered optical fields. Some general conclusions drawn throughout this thesis are listed:

- The Generalized Lorentz-Mie Theory of light scattering was used to simulate the fields inside and outside a sphere for different configurations and beam shapes. Additionally, we have presented calculations of the force acting on the scattering sphere. While the GLMT gives a qualitative understanding of the optical binding process several other factors must be accounted for in a full description of the experimental geometry used, including the amplitude variation across the particle of the incident evanescent field, multiple scattering between the particle and the substrate, and multiple scattering between the particles in the optically bound structure. Experimental results presented in this thesis, such as the two-dimensional binding, highlight the need for rigorous multiple

scattering effects in order to obtain results that match experiments.

- Silica micro-spheres form one-dimensional chain structures in the evanescent field of two counter-propagating beams. The inter-particle separation in such structures depends on particle size. Even though, in the presence of interference there exists a force exerted on a particle due to the fringes, it has been shown that the forces that arise from the multiple scattering of the incident field are dominant for some particle sizes. This said, additional (to optical) effects must be included to completely describe the structures formed i.e. the effects of hydrodynamic coupling and electrostatic interactions between the spheres and the substrate.

- The spring constant can be derived from the Brownian motion of the bound particles. We have quantified the optical potential for individual particles held in optically bound arrays. The bound structures are more stable with increasing laser power since the particles are held in deeper potential wells.

- The use of two orthogonal beam pairs (incident and counter-propagating beams) leads to the formation of two-dimensional arrays. We have found that for two orthogonal beam pairs with parallel polarisations 1.0 μm silica particles are bound in square-lattice bound structures. Alternatively, when the beam pairs are cross-polarised the same particles are trapped in a hexagonal-lattice geometry. For the case of 0.8 μm silica particles, we observed only the formation of hexagonal lattice arrays for both polarisation configurations. This suggests that the formation of two-dimensional structures depends on particle size. This dependence with size, however, is not as simple as the oscillating influence of the background with size as shown in Chapter 4. As the particle size becomes larger the particles are influenced by more trapping sites leading to different bound geometries. Additionally, multiple smaller particles can occupy a single trapping site resulting to close-packed bound structures.

- It has been shown for the first time that carbon nano-tube bundles can be trapped in a counter-propagating beam evanescent surface trap configuration and form chain like structures. The orientation of the cylinder axis does not change with polarisation. A multiple light scattering model for a number of interacting finite cylinders is needed. Such model is even more complicated than one considering spherical objects.

- The small diameter of tapered fibres and the relatively large difference between the refractive indices of the fibre and the surrounding medium can be utilised to produce strong evanescent field that can be used to optically trap and bind micro- and nano-particles. In Chapter 5 we have shown calculations for the evanescent field penetration depth as a function of fibre diameter.

- It is suggested that the sensitivity of the nano-particle dynamics to the polarisation and wavelength of the laser fields through the plasmon resonance could make such tapered fibres an effective tool for sorting and separating nano-particles according to property-dependent criteria. We have presented results demonstrating the motion of metallic nano-particles along the tapered region of a tapered fibre for different polarisation configurations. Furthermore, calculations were made supporting that separation of metallic particles can be achieved when the wavelength of the guided mode is chosen carefully.

- Polystyrene micro-particles can be attracted to, and propelled along the tapered region of a fibre. The polarisation of the mode guided in the fibre can control the motion of particles. An example of this statement is the demonstration of the helical trajectory that particles follow when the circularly polarised fundamental mode is guided in the taper as shown in Chapter 5. This also demonstrates a conversion from spin to orbital angular momentum of the light, previously observed in high NA optical trapping.

In conclusion, it is anticipated that the sensitivity of the optical binding phenomena to light polarisation, particle size and material can be potentially a useful tool for selectively trapping, sorting and trafficking of micro-and nano-particles.

8.2 Future Directions

Even though this thesis provides some results on the optical binding of micro-particles in evanescent fields there are a number of questions still unanswered. The work presented in this thesis is only the starting point to more precise and complicated experiments:

- Incorporate the evanescent field surface and fibre traps with optical tweezers to make quantitative measurements of the binding force. This technique uses a quadrant photo-diode (QPD) to collect the reflected laser light of the surface of a trapped particle. The QPD is connected to a computer and the force constant can be obtained. A weak optical tweezers traps the particle on top of the prism-water interface. The particle feels the presence of the evanescent field and moves by a measurable distance Δx from equilibrium. Since the spring constant of the tweezers is known, one can obtain the force due to the evanescent field as $F = -k\Delta x$.

- Use of a fast camera for data collection will allow the measurement of particle fluctuation correlations in the optically bound lattices. This can potentially provide more information about the dynamics of the particles in such bound states. It is also an additional way to calculate the optical binding spring constant.

- Use ellipsoidal or rod-shaped particles to mimic Escherichia coli bacteria biofilm formation: The aim of this is to get an understanding of the alignment of such bacteria in the biofilm. This will help to identify if E. coli bacteria align themselves in a biofilm due to their shape and hydrodynamics or due to the protein-ligand interactions.

- Optimise the fibre pulling method to achieve adiabatic tapers. This will enable the use of higher order modes that could lead to an extra degree of control over particle manipulation. This may be beneficial to particle sorting and transport.

- Use evanescent field surface traps and optical nanofibers enhanced by plasmonic structures for interfacing, manipulating, and controlling colloidal micro- and nano-scale particles, as well as biological samples of such sizes. This will result in new optical coupling schemes and further understanding of light-matter interactions.

Bibliography

[1] A. Ashkin, J. M. Dziedzic, J. E. Bjorkholm, and S. Chu, "Observation of a single-beam gradient force optical trap for dielectric particles," *Opt. Lett.*, vol. 11, no. 5, pp. 288–290, 1986.

[2] K. Castelino, S. Satyanarayana, and M. Sitti, "Manufacturing of two and three-dimensional micro/nanostructures by integrating optical tweezers with chemical assembly," *Robotica*, vol. 23, no. 4, pp. 435–439, 2005.

[3] K. Dholakia and P. Zemánek, "Colloquium: gripped by light: optical binding," *Reviews of Modern Physics*, vol. 82, no. 2, p. 1767, 2010.

[4] M. M. Burns, J.-M. Fournier, and J. A. Golovchenko, "Optical binding," *Phys. Rev. Lett.*, vol. 63, pp. 1233–1236, 1989.

[5] M. M. Burns, J.-M. Fournier, and J. A. Golovchenko, "Optical Matter: Crystallization and Binding in Intense Optical Fields," *Science*, vol. 249, no. 4970, pp. 749–754, 1990.

[6] S. Kawata and T. Sugiura, "Movement of micrometer-sized particles in the evanescent field of a laser beam," *Opt. Lett.*, vol. 17, no. 11, pp. 772–774, 1992.

[7] V. Garces-Chavez, K. Dholakia, and G. C. Spalding, "Extended-area optically induced organization of microparticles on a surface," *Applied Physics Letters*, vol. 86, no. 3, pp. 031 106 –031 106–3, 2005.

[8] G. Sagué, E. Vetsch, W. Alt, D. Meschede, and A. Rauschenbeutel, "Cold-atom physics using ultrathin optical fibers: Light-induced dipole forces and surface interactions," *Phys. Rev. Lett.*, vol. 99, p. 163602, 2007.

[9] G. Brambilla, G. S. Murugan, J. S. Wilkinson, and D. J. Richardson, "Optical manipulation of microspheres along a subwavelength optical wire," *Opt. Lett.*, vol. 32, no. 20, pp. 3041–3043, 2007.

[10] L. Tong, R. Gattass, J. Ashcom, S. He, J. Lou, M. Shen, I. Maxwell, and E. Mazur, "Subwavelength-diameter silica wires for low-loss optical wave guiding," *Nature*, vol. 426, no. 6968, pp. 816–819, 2003.

[11] A. Ashkin, "Forces of a single-beam gradient laser trap on a dielectric sphere in the ray optics regime," *Biophysical Journal*, vol. 61, no. 2, pp. 569–582, 1992.

[12] Y. Harada and T. Asakura, "Radiation forces on a dielectric sphere in the Rayleigh scattering regime," *Optics communications*, vol. 124, no. 5, pp. 529–541, 1996.

[13] J. Ng, Z. Lin, C. Chan, and P. Sheng, "Photonic clusters formed by dielectric microspheres: Numerical simulations," *Physical Review B*, vol. 72, no. 8, p. 085130, 2005.

[14] S. A. Tatarkova, A. E. Carruthers, and K. Dholakia, "One-dimensional optically bound arrays of microscopic particles," *Phys. Rev. Lett.*, vol. 89, p. 283901, 2002.

[15] W. Singer, M. Frick, S. Bernet, and M. Ritsch-Marte, "Self-organized array of regularly spaced microbeads in a fiber-optical trap," *J. Opt. Soc. Am. B*, vol. 20, no. 7, pp. 1568–1574, 2003.

[16] D. McGloin, A. Carruthers, K. Dholakia, and E. Wright, "Optically bound microscopic particles in one dimension," *Physical Review E*, vol. 69, no. 2, p. 021403, 2004.

[17] N. Metzger, E. Wright, and K. Dholakia, "Theory and simulation of the bistable behaviour of optically bound particles in the Mie size regime," *New Journal of Physics*, vol. 8, no. 8, p. 139, 2006.

[18] J. W. Goodman, *Introduction to Fourier optics*. McGraw-hill New York, 1968, vol. 2.

[19] R. Gordon, M. Kawano, J. Blakely, and D. Sinton, "Optohydrodynamic theory of particles in a dual-beam optical trap," *Physical Review B*, vol. 77, no. 24, p. 245125, 2008.

[20] J. D. Jackson and R. F. Fox, "Classical electrodynamics," *American Journal of Physics*, vol. 67, p. 841, 1999.

[21] C. D. Mellor and C. D. Bain, "Array formation in evanescent waves," *Chem Phys Chem*, vol. 7, no. 2, pp. 329–332, 2006.

[22] C. Mellor, T. Fennerty, and C. Bain, "Polarization effects in optically bound particle arrays," *Optics Express*, vol. 14, no. 21, pp. 10 079–10 088, 2006.

[23] J. Taylor, L. Wong, C. Bain, and G. Love, "Emergent properties in optically bound matter," *Optics Express*, vol. 16, no. 10, pp. 6921–6929, 2008.

[24] V. Garcés-Chávez, R. Quidant, P. J. Reece, G. Badenes, L. Torner, and K. Dholakia, "Extended organization of colloidal microparticles by surface plasmon polariton excitation," *Phys. Rev. B*, vol. 73, p. 085417, 2006.

[25] K. Huang, S. Yang, and L. Tong, "Modeling of evanescent coupling between two parallel optical nanowires," *Appl. Opt.*, vol. 46, no. 9, pp. 1429–1434, 2007.

[26] J. Bures and R. Ghosh, "Power density of the evanescent field in the vicinity of a tapered fiber," *J. Opt. Soc. Am. A*, vol. 16, no. 8, pp. 1992–1996, 1999.

[27] L. Tong, J. Lou, and E. Mazur, "Single-mode guiding properties of subwavelength-diameter silica and silicon wire waveguides," *Opt. Express*, vol. 12, no. 6, pp. 1025–1035, 2004.

[28] V. Balykin, K. Hakuta, F. Le Kien, J. Liang, and M. Morinaga, "Atom trapping and guiding with a subwavelength-diameter optical fiber," *Physical Review A*, vol. 70, no. 1, p. 011401, 2004.

[29] T. M. Grzegorczyk, B. A. Kemp, and J. A. Kong, "Trapping and binding of an arbitrary number of cylindrical particles in an in-plane electromagnetic field," *JOSA A*, vol. 23, no. 9, pp. 2324–2330, 2006.

[30] K.-N. Liou, "A complementary theory of light scattering by homogeneous spheres," *Applied Mathematics and Computation*, vol. 3, no. 4, pp. 331 – 358, 1977.

[31] H. C. van de Hulst, *Light scattering by small particles.* Dover Publications, 1981.

[32] G. Mie, "Beiträge zur optik trüber medien, speziell kolloidaler metallösungen," *Annalen der Physik*, vol. 330, no. 3, pp. 377–445, 1908.

[33] P. Debye, "Der lichtdruck auf kugeln von beliebigem material," *Annalen der physik*, vol. 335, no. 11, pp. 57–136, 1909.

[34] J. A. Stratton, *Electromagnetic Theory.* McGraw-Hill, 1941.

[35] E. Wolf and M. Born, *Principles of optics.* Pergamon press, 1965.

[36] M. Kerker, *The scattering of light, and other electromagnetic radiation.* Academic Press, 1969.

[37] I. H. Malitson, "Interspecimen comparison of the refractive index of fused silica," *J. Opt. Soc. Am.*, vol. 55, no. 10, pp. 1205–1208, 1965.

[38] G. M. Hale and M. R. Querry, "Optical constants of water in the 200-nm to 200-μm wavelength region," *Appl. Opt.*, vol. 12, no. 3, pp. 555–563, 1973.

[39] W. J. Wiscombe, "Improved mie scattering algorithms," *Applied Optics*, vol. 19, no. 9, pp. 1505–1509, 1980.

[40] G. Gouesbet and G. Grehan, "Sur la généralisation de la théorie de Lorentz-Mie," *J. Optics*, vol. 13, no. 2, pp. 97–103, 1982.

[41] G. Sansome, G. Sansone, and A. H. Diamond, *Expansions in Series of Legendre Polynomials and Spherical Harmonics.* Dover Books New York, 1991.

[42] G. Gouesbet, B. Maheu, and G. Grehan, "Scattering of a Gaussian beam by a Mie scatter center using a bromwich formalism," *J. Optics (Paris)*, vol. 16, no. 2, pp. 83–93, 1985.

[43] J. Lekner, "Force on a scatterer in counter-propagating coherent beams," *J. Optics A: Pure and Applied Optics*, vol. 7, no. 5, p. 238, 2005.

[44] N. K. Metzger, R. F. Marchington, M. Mazilu, R. L. Smith, K. Dholakia, and E. M. Wright, "Measurement of the restoring forces acting on two optically bound particles from normal mode correlations," *Phys. Rev. Lett.*, vol. 98, p. 068102, 2007.

[45] G. M. Gibson, J. Leach, S. Keen, A. J. Wright, and M. J. Padgett, "Measuring the accuracy of particle position and force in optical tweezers using high-speed video microscopy," *Optics express*, vol. 16, no. 19, pp. 14 561–14 570, 2008.

[46] G. D. G. Crocker J. C., "Methods of digital microscopy for colloidal studies," *J. Coll. Interf. Sci.*, vol. 179, pp. 298–310, 1996.

[47] A. Schott, "SCHOTT optical glass data sheet-catalog." [Online]. Available: http://www.us.schott.com/advanced_optics/english/our_products/materials/data_tools/index.html

[48] D. Blair and E. Dufresne. (2009) The Matlab particle tracking code repository. [Online]. Available: http://physics.georgetown.edu/matlab/

[49] A. Rohrbach and E. H. Stelzer, "Three-dimensional position detection of optically trapped dielectric particles," *Journal of applied physics*, vol. 91, no. 8, pp. 5474–5488, 2002.

[50] M. Friese, H. Rubinsztein-Dunlop, N. Heckenberg, and E. Dearden, "Determination of the force constant of a single-beam gradient trap by measurement of backscattered light," *Applied optics*, vol. 35, no. 36, pp. 7112–7116, 1996.

[51] J. Huisstede, K. van der Werf, M. Bennink, and V. Subramaniam, "Force detection in optical tweezers using backscattered light," *Optics Express*, vol. 13, no. 4, pp. 1113–1123, 2005.

[52] G. Volpe, G. Kozyreff, and D. Petrov, "Photonic force microscopy with back-scattered light," *Conference on Lasers and Electro-Optics/Quantum Electronics and Laser Science Conference and Photonic Applications Systems Technologies*, p. JThD96, 2007.

[53] P. Zemánek, A. Jonáš, L. Šrámek, and M. Liška, "Optical trapping of Rayleigh particles using a Gaussian standing wave," *Optics communications*, vol. 151, no. 4, pp. 273–285, 1998.

[54] V. Karásek, K. Dholakia, and P. Zemánek, "Analysis of optical binding in one dimension," *Applied Physics B*, vol. 84, no. 1-2, pp. 149–156, 2006.

[55] P. Chaumet and M. Nieto-Vesperinas, "Optical binding of particles with or without the presence of a flat dielectric surface," *Physical Review B*, vol. 64, no. 3, p. 035422, 2001.

[56] V. Karásek, T. Čižmár, O. Brzobohatỳ, P. Zemánek, V. Garcés-Chávez, and K. Dholakia, "Long-range one-dimensional longitudinal optical binding," *Physical review letters*, vol. 101, no. 14, p. 143601, 2008.

[57] M. D. Summers, R. D. Dear, J. M. Taylor, and G. A. Ritchie, "Directed assembly of optically bound matter," *Optics Express*, vol. 20, no. 2, pp. 1001–1012, 2012.

[58] D. L. Andrews and L. C. Davila Romero, "Mechanisms for optical binding," *Proc. SPIE*, vol. 7400, pp. 74 001H–74 001H–10, 2009.

[59] M. Mazilu, A. Rudhall, E. M. Wright, and K. Dholakia, "An interacting dipole model to explore broadband transverse optical binding," *Journal of Physics: Condensed Matter*, vol. 24, no. 46, p. 464117, 2012.

[60] P. Reece, E. Wright, and K. Dholakia, "Experimental observation of modulation instability and optical spatial soliton arrays in soft condensed matter," *Physical review letters*, vol. 98, no. 20, p. 203902, 2007.

[61] M. Kawano, J. Blakely, R. Gordon, and D. Sinton, "Theory of dielectric micro-sphere dynamics in a dual-beam optical trap," *Optics Express*, vol. 16, no. 13, pp. 9306–9317, 2008.

[62] J. Taylor and G. Love, "Spontaneous symmetry breaking and circulation by optically bound microparticle chains in Gaussian beam traps," *Physical Review A*, vol. 80, no. 5, p. 053808, 2009.

[63] A. Okabe, B. Boots, K. Sugihara, and S. N. Chiu, *Spatial tessellations: concepts and applications of Voronoi diagrams*. Wiley, 2009, vol. 501.

[64] P. J. Steinhardt, D. R. Nelson, and M. Ronchetti, "Bond-orientational order in liquids and glasses," *Phys. Rev. B*, vol. 28, pp. 784–805, 1983.

[65] R. T. Wang and H. Van de Hulst, "Application of the exact solution for scattering by an infinite cylinder to the estimation of scattering by a finite cylinder," *Applied optics*, vol. 34, no. 15, pp. 2811–2821, 1995.

[66] T. A. Bashkatova, A. N. Bashkatov, V. I. Kochubey, and V. V. Tuchin, "Light-scattering properties for spherical and cylindrical particles: a simple approximation derived from Mie calculations," pp. 247–259, 2001.

[67] D. L. Andrews and D. S. Bradshaw, "Laser-induced forces between carbon nanotubes," *Optics letters*, vol. 30, no. 7, pp. 783–785, 2005.

[68] D. Brown. (2013) Tracker. video analysis and modelling tool. [Online]. Available: http://www.cabrillo.edu/~dbrown/tracker/

[69] A. Irrera, P. Artoni, R. Saija, P. G. Gucciardi, M. A. Iat, F. Borghese, P. Denti, F. Iacona, F. Priolo, and O. M. Maragò, "Size-scaling in optical trapping of silicon nanowires," *Nano Letters*, vol. 11, no. 11, pp. 4879–4884, 2011.

[70] J. P. Burke, Jr., S. T. Chu, G. W. Bryant, C. J. Williams, and P. S. Julienne, "Trapping atoms with evanescent light fields from integrated optical waveguides," *Proc. SPIE*, vol. 4271, pp. 52–61, 2001.

[71] A. H. Yang, S. D. Moore, B. S. Schmidt, M. Klug, M. Lipson, and D. Erickson, "Optical manipulation of nanoparticles and biomolecules in sub-wavelength slot waveguides," *Nature*, vol. 457, no. 7225, pp. 71–75, 2009.

[72] G. Brambilla, G. S. Murugan, J. Wilkinson, and D. Richardson, "Optical manipulation of microspheres along a subwavelength optical wire," *Optics letters*, vol. 32, no. 20, pp. 3041–3043, 2007.

[73] M. J. Morrissey, K. Deasy, Y. Wu, S. Chakrabarti, and S. Nic Chormaic, "Tapered optical fibers as tools for probing magneto-optical trap characteristics," *Review of Scientific Instruments*, vol. 80, no. 5, pp. 053 102–053 102–5, 2009.

[74] P. Polynkin, A. Polynkin, N. Peyghambarian, and M. Mansuripur, "Evanescent field-based optical fiber sensing device for measuring the refractive index of liquids in microfluidic channels," *Opt. Lett.*, vol. 30, no. 11, pp. 1273–1275, 2005.

[75] S. Leon-Saval, T. Birks, W. Wadsworth, P. St J Russell, and M. Mason, "Supercontinuum generation in submicron fibre waveguides," *Optics Express*, vol. 12, no. 13, pp. 2864–2869, 2004.

[76] S. Skelton, M. Sergides, R. Patel, E. Karczewska, O. Maragò, and P. Jones, "Optical trapping and optical binding using cylindrical vector beams," *AAPP— Physical, Mathematical, and Natural Sciences*, vol. 89, no. S1, 2011.

[77] S. Skelton, M. Sergides, R. Patel, E. Karczewska, O. Maragó, and P. Jones, "Evanescent wave optical trapping and transport of micro- and nanoparticles on tapered optical fibers," *Journal of Quantitative Spectroscopy and Radiative Transfer*, 2012.

[78] H. Xin, C. Cheng, and B. Li, "Trapping and delivery of Escherichia coli in a microfluidic channel using an optical nanofiber," *Nanoscale*, pp. 6720–6724, 2013.

[79] E. Vetsch, D. Reitz, G. Sagué, R. Schmidt, S. Dawkins, and A. Rauschenbeutel, "Optical interface created by laser-cooled atoms trapped in the evanescent field surrounding an optical nanofiber," *Physical review letters*, vol. 104, no. 20, p. 203603, 2010.

[80] D. Marcuse, *Light transmission optics*, 2nd ed. Van Nostrand Reinhold, 1982.

[81] A. W. Snyder and J. Love, *Optical waveguide theory*. Springer, 1983, vol. 190.

[82] A. Yariv, *Optical Electronics*, 3rd ed. CBS College Publishing, 1985.

[83] F. L. Kien, K. Hakuta, and V. Balykin, "Angular momentum of light in an optical nanofiber," *Physical Review. A*, vol. 73, no. 5, 2006.

[84] I. Malitson, "Interspecimen comparison of the refractive index of fused silica," *JOSA*, vol. 55, no. 10, pp. 1205–1208, 1965.

[85] F. L. Kien, J. Liang, K. Hakuta, and V. Balykin, "Field intensity distributions and polarization orientations in a vacuum-clad subwavelength-diameter optical fiber," *Optics communications*, vol. 242, no. 4, pp. 445–455, 2004.

[86] T. Nieminen, G. Knöner, N. Heckenberg, and H. Rubinsztein-Dunlop, "Physics of optical tweezers," *Methods in Cell Biology*, vol. 82, pp. 207–236, 2007.

[87] M. Meier and A. Wokaun, "Enhanced fields on large metal particles: dynamic depolarization," *Optics Letters*, vol. 8, no. 11, pp. 581–583, 1983.

[88] J. P. Gordon, "Radiation forces and momenta in dielectric media," *Physical Review A*, vol. 8, no. 1, p. 14, 1973.

[89] S. Albaladejo, M. I. Marqués, M. Laroche, and J. J. Sáenz, "Scattering forces from the curl of the spin angular momentum of a light field," *Physical review letters*, vol. 102, no. 11, p. 113602, 2009.

[90] J. Arias-Gonzalez and M. Nieto-Vesperinas, "Optical forces on small particles: attractive and repulsive nature and plasmon-resonance conditions," *JOSA A*, vol. 20, no. 7, pp. 1201–1209, 2003.

[91] I. Iglesias and J. J. Sáenz, "Scattering forces in the focal volume of high numerical aperture microscope objectives," *Optics Communications*, vol. 284, no. 10, pp. 2430–2436, 2011.

[92] F. Le Kien, V. Balykin, and K. Hakuta, "Light-induced force and torque on an atom outside a nanofiber," *Physical Review Series A*, vol. 74, no. 3, p. 033412, 2006.

[93] P. Yeh, A. Yariv, and E. Marom, "Theory of Bragg fiber," *J. Opt. Soc. Am.*, vol. 68, no. 9, pp. 1196–1201, 1978.

[94] C. Román-Velázquez, C. Noguez, and R. Barrera, "Substrate effects on the optical properties of spheroidal nanoparticles," *Physical Review B*, vol. 61, no. 15, p. 10427, 2000.

[95] N. W. Ashcroft and N. D. Mermin, *Solid State Physics*. Holt and Rinehart and Winston, New York, 1976, vol. 1.

[96] P. Winsemius, "Structure dependence of the optical properties of Cu, Ag and Au," *Physica B+ C*, vol. 79, pp. 529–546, 1975.

[97] H. Kuwata, H. Tamaru, K. Esumi, and K. Miyano, "Resonant light scattering from metal nanoparticles: Practical analysis beyond Rayleigh approximation," *Applied physics letters*, vol. 83, no. 22, pp. 4625–4627, 2003.

[98] K. Svoboda and S. M. Block, "Optical trapping of metallic Rayleigh particles," *Optics Letters*, vol. 19, no. 13, pp. 930–932, 1994.

[99] A. D. Rakic, A. B. Djurišic, J. M. Elazar, and M. L. Majewski, "Optical properties of metallic films for vertical-cavity optoelectronic devices," *Applied optics*, vol. 37, no. 22, pp. 5271–5283, 1998.

[100] S. Albaladejo, M. I. Marqués, and J. J. Sáenz, "Light control of silver nanoparticles diffusion," *Optics Express*, vol. 19, no. 12, pp. 11 471–11 478, 2011.

[101] T. Klar, M. Perner, S. Grosse, G. Von Plessen, W. Spirkl, and J. Feldmann, "Surface-plasmon resonances in single metallic nanoparticles," *Physical Review Letters*, vol. 80, no. 19, pp. 4249–4252, 1998.

[102] P. M. Hansen, V. K. Bhatia, N. Harrit, and L. Oddershede, "Expanding the optical trapping range of gold nanoparticles," *Nano letters*, vol. 5, no. 10, pp. 1937–1942, 2005.

[103] L. Bosanac, T. Aabo, P. M. Bendix, and L. B. Oddershede, "Efficient optical trapping and visualization of silver nanoparticles," *Nano letters*, vol. 8, no. 5, pp. 1486–1491, 2008.

[104] J. E. Molloy and M. J. Padgett, "Lights, action: optical tweezers," *Contemporary Physics*, vol. 43, no. 4, pp. 241–258, 2002.

[105] R. Saija, P. Denti, F. Borghese, and M. A. Iatỳ, "Optical trapping calculations for metal nanoparticles. Comparison with experimental data for Au and Ag spheres." *Optics express*, vol. 17, no. 12, pp. 10 231–10 241, 2009.

[106] F. Hajizadeh and S. N. S Reihani, "Optimized optical trapping of gold nanoparticles," *Optics express*, vol. 18, no. 2, pp. 551–559, 2010.

[107] E. Messina, E. Cavallaro, A. Cacciola, M. A. Iatì, P. G. Gucciardi, F. Borghese, P. Denti, R. Saija, G. Compagnini, and M. Meneghetti, "Plasmon-enhanced optical trapping of gold nanoaggregates with selected optical properties," *ACS nano*, vol. 5, no. 2, pp. 905–913, 2011.

[108] L. Ng, M. Zervas, J. Wilkinson, and B. Luff, "Manipulation of colloidal gold nanoparticles in the evanescent field of a channel waveguide," *Applied Physics Letters*, vol. 76, no. 15, pp. 1993–1995, 2000.

[109] G. Volpe, R. Quidant, G. Badenes, and D. Petrov, "Surface plasmon radiation forces," *Physical review letters*, vol. 96, no. 23, p. 238101, 2006.

[110] K. Wang, E. Schonbrun, and K. B. Crozier, "Propulsion of gold nanoparticles with surface plasmon polaritons: evidence of enhanced optical force from near-field coupling between gold particle and gold film," *Nano letters*, vol. 9, no. 7, pp. 2623–2629, 2009.

[111] P. Chaumet and M. Nieto-Vesperinas, "Electromagnetic force on a metallic particle in the presence of a dielectric surface," *Physical Review B*, vol. 62, no. 16, p. 11185, 2000.

[112] Y. B. Ovchinnikov, I. Manek, and R. Grimm, "Surface trap for Cs atoms based on evanescent-wave cooling," *Physical review letters*, vol. 79, no. 12, pp. 2225–2228, 1997.

[113] M. Ploschner, T. Cizmar, M. Mazilu, A. Di Falco, and K. Dholakia, "Bidirectional optical sorting of gold nanoparticles," *Nano letters*, vol. 12, no. 4, pp. 1923–1927, 2012.

[114] L. Zhao, Y. Li, J. Qi, J. Xu, and Q. Sun, "Quasi 3-dimensional optical trapping by two counter-propagating beams in nano-fiber," *Optics express*, vol. 18, no. 6, pp. 5724–5729, 2010.

[115] R. Cox, "The motion of suspended particles almost in contact," *International Journal of Multiphase Flow*, vol. 1, no. 2, pp. 343–371, 1974.

[116] G. Brambilla, V. Finazzi, and D. Richardson, "Ultra-low-loss optical fiber nanotapers," *Optics Express*, vol. 12, no. 10, pp. 2258–2263, 2004.

[117] T. E. Dimmick, G. Kakarantzas, T. A. Birks, and P. S. J. Russell, "Carbon dioxide laser fabrication of fused-fiber couplers and tapers," *Applied Optics*, vol. 38, no. 33, pp. 6845–6848, 1999.

[118] L. Shi, X. Chen, H. Liu, Y. Chen, Z. Ye, W. Liao, and Y. Xia, "Fabrication of submicron-diameter silica fibers using electric strip heater," *Opt. Express*, vol. 14, no. 12, pp. 5055–5060, 2006.

[119] A. Petchu-Colan, M. Frawley, and S. N. Chormaic, "Tapered few-mode fibers: Mode evolution during fabrication and adiabaticity," *Journal of Nonlinear Optical Physics and Materials*, vol. 20, no. 03, pp. 293–307, 2011.

[120] T. A. Birks and Y. W. Li, "The shape of fiber tapers," *Lightwave Technology, Journal of*, vol. 10, no. 4, pp. 432–438, 1992.

[121] H. Lefevre, "Single-mode fibre fractional wave devices and polarisation controllers," *Electronics Letters*, vol. 16, no. 20, pp. 778–780, 1980.

[122] K. Jedrzejewski, "Biconical fused taper-a universal fibre devices technology," *OPTOELECTRONICS REVIEW*, no. 2, pp. 153–160, 2000.

[123] F. Payne, C. Hussey, and M. Yataki, "Modelling fused single-mode-fibre couplers," *Electronics Letters*, vol. 21, no. 11, pp. 461–462, 1985.

[124] K. Y. Bliokh, E. A. Ostrovskaya, M. A. Alonso, O. G. Rodríguez-Herrera, D. Lara, and C. Dainty, "Spin-to-orbital angular momentum conversion in focusing, scattering, and imaging systems," *Opt. Express*, vol. 19, no. 27, pp. 26 132–26 149, 2011.

[125] D. G. O'Shea, J. M. Ward, B. J. Shortt, M. Mortier, P. Fron, and S. N. Chormaic, "Upconversion channels in Er^{3+}:ZBLALiP fluoride glass microspheres," *The European Physical Journal Applied Physics*, vol. 40, pp. 181–188, 2007.

[126] M. C. Frawley, A. Petcu-Colan, V. G. Truong, and S. N. Chormaic, "Higher order mode propagation in an optical nanofiber," *Optics Communications*, vol. 285, no. 23, pp. 4648 – 4654, 2012.